RECIPE IMPROVEMENT AND MATHEMATICAL MODELLING OF POLYMER GEL DOSIMETERS

by

Jonathan Nathaniel Michel Chain

A thesis submitted to the Department of Chemical Engineering

In conformity with the requirements for

the degree of Master of Applied Science

Queen's University

Kingston, Ontario, Canada

(December, 2010)

Abstract

A mathematical model for polymer gel dosimeters was extended to simulate the effects of radiation depth doses of various radiation beams on the mass of polymer formed. The influences of monomer diffusion and temperature variation were investigated and predicted by the model. Simulation results indicate that both diffusion and temperature effects are most noticeable at the depth of maximum dose. Diffusion effects are larger for steep depth-dose curves with large dose gradients, while temperature effects are larger for extensive depth-dose curves that deliver high doses of radiation to a greater depth. Based on simulation results, involving a maximum dose of 5 Gy, the amount of additional polymer formed due to diffusion is small, ranging from 0.1 % for 15 MV x-ray photons to 2.6 % for Co^{60} γ-radiation. This small amount of additional polymer should not cause significant problems for the accuracy of depth-dose calibration curves, particularly if the depth of maximum dose is avoided. Inaccuracies caused by temperature effects are expected to be smaller than those caused by diffusion.

Experimental studies were undertaken to improve the radiation dose response using x-ray Computed Tomography (CT). A new polymer gel dosimeter recipe with enhanced dose response was achieved by using a large quantity of *N*-isopropyl acrylamide (NIPAM) (15 wt%) to help dissolve the *N,N*'-methylene bisacrylamide (Bis) crosslinker. The solubility of Bis was substantially increased, allowing for large quantities of dissolved NIPAM and Bis in the system. The new dosimeter exhibits an enhanced dose sensitivity and dose resolution for x-ray CT imaging, which holds promise for clinical applications. The dose resolution of approximately 0.1 Gy, for up to absorbed doses of 50 Gy, for the new recipe is superior to that for previous dosimeter formulations developed for x-ray CT.

Co-Authorship

The research that is presented in this thesis was conducted independently by me, under the guidance and supervision of Dr. K. B. McAuley of the Department of Chemical Engineering (Queen's University), and Dr. L. J. Schreiner of the Cancer Centre of Southeastern Ontario and the Departments of Oncology and Physics (Queen's University).

Chapter 2, which describes the development of an extended mathematical model, presents some additions to the reaction scheme, which was developed by myself and Mr. A. T. Nasr. Dr. McAuley and Dr. Schreiner assisted in the preparation and editing of Chapter 2 and provided technical advice. The manuscript in Chapter 2 will be submitted for publication in a refereed journal (*Macromolecular Theory Simulations*).

Dr. A. Jirasek from the University of Victoria assisted with the irradiation of samples and use of x-ray computed tomography for experiments in Chapter 3. Dr. T. Olding assisted with the irradiation of samples for optical imaging in Chapter 3. In addition to Dr. McAuley and Dr. Schreiner, Dr. Jirasek assisted in the preparation and editing of the manuscript, which has been submitted for publication in a refereed journal (*Physics in Medicine and Biology*).

Acknowledgments

Above all, I would like to express my gratitude to my supervisors Dr. Kim McAuley and Dr. John Schreiner, for their guidance, advice and encouragement throughout my research at Queen's. It was a great learning experience, and a pleasure to work with such friendly, enthusiastic and supportive people.

I would also like to thank Dr. Tim Olding of the Cancer Centre of Southeastern Ontario and Dr. Andrew Jirasek of the University of Victoria for their assistance in the experimental work and invaluable support. Your help, suggestions and the pleasant discussions we have had were much appreciated. Many thanks also to the faculty, staff and students of the Department of Chemical Engineering, especially my officemates in G36 (Duncan, Shaohua, Hui, Steve, Angelica, John, Kevin, Wei, Hadis, Zahra and Yutian), who made my time in graduate studies at Queen's very enjoyable. Particular thanks are due to Valeria Koeva, who showed me how to make gels.

I am especially grateful to my parents and brothers for their continuous love and support, and the encouragement to pursue my dreams.

Table of Contents

List of Figures

List of Tables

Nomenclature

Symbols	
C_p	Heat capacity of the PAG gel system [J kg^{-1} K^{-1}]
d_b	Depth of the back wall
d_{max}	Depth of maximum delivered dose on depth-dose curves
D^i	Dead polymer chain in the *i*th phase. In the aqueous phase, subscript *n* indicates the length of the chain
D^i_i	Diffusivity in the *i*th phase of the j^{th} species [cm^2 min^{-1}]
G	Gelatin
h	Heat transfer coefficient for heat transfer from the PAG to the surrounding environment [J cm^{-2} K^{-1} s^{-1}]
H_2O	Water
ΔH_R	Energy released per mole of double bonds consumed
k_{cond}	Thermal conductivity in the PAG dosimeter [J cm^{-1} K^{-1} s^{-1}]
k_c	Rate constant for intermolecular cyclization reactions [mol^{-1} s^{-1}]
$k_{f,jk}$	Rate constant for chain transfer reaction of a polymer radical bearing the active radical on an acrylamide unit (j = 1) or bisacrylamide unit (j = 2) to acrylamide monomer (k = 1) or bisacrylamide monomer (k = 2) [mol^{-1} s^{-1}]
$k_{f,jG}$	Rate constant for chain transfer reaction of a polymer radical bearing the active radical on an acrylamide unit (j = 1) or bisacrylamide unit (j = 2) to gelatin [mol^{-1} s^{-1}]
$k_{i,k}$	Rate constant for initiation reaction between primary radicals and acrylamide monomer (k = 1) or bisacrylamide monomer (k = 2) [$M^{-1}s^{-1}$]
k_m	Mass transfer coefficient [s^{-1}]

$k_{p,jk}$	Rate constant for propagation of a polymer radical bearing the active radical on an acrylamide unit (j = 1) or bisacrylamide unit (j = 2) with acrylamide monomer (k = 1) or bisacrylamide monomer (k = 2) [mol^{-1} s^{-1}]
$k_{p,Gk}$	Rate constant for re-initiation of a gelatin radical with acrylamide monomer (k = 1) or bisacrylamide monomer (k = 2) [mol^{-1} s^{-1}]
$k_{t,jk}$	Rate constant for termination reaction between a polymer radical bearing the active radical on an acrylamide unit (j = 1) or bisacrylamide unit (j = 2) and a polymer radical bearing the active radical on an acrylamide unit (k = 1), bisacrylamide unit (k = 2) [mol^{-1} s^{-1}]
$k_{x,j}$	Rate constant for crosslinking reaction between an unreacted pendant double bond and a polymer radical bearing the active radical on an acrylamide unit (j = 1) or bisacrylamide unit (j = 2) [mol^{-1} s^{-1}]
L_i	Growing radical in polymer phase, bearing the active radicals on an acrylamide unit (i = 1) or bisacrylamide unit (i = 2) unit.
M_1	Acrylamide monomer
M_2	Bisacrylamide monomer
$M_{w,H2O}$	Molecular weight of water [g mol^{-1}]
N_{CT}	X-ray CT readout number [H]
n_{PDE}	Number of pendent double bonds on a water soluble polymer chain
$(PR^{\bullet})$	Primary radical in water cage
$PR^{\bullet}$	Primary radical outside of water cage
r_i	Rate of reaction of species i [mol L^{-1} s^{-1}]
R_2	Transverse relaxation rate [s^{-1}]
R_{PR}	Rate of generation of primary radicals [mol s^{-1}]
$S_{i,n}$	(short) Propagating radical of length n, bearing the active radicals on an acrylamide unit (i = 1) or bisacrylamide unit (i = 2).
T	Temperature inside the PAG system [°C]

T_S	Temperature of the surrounding environment [°C]
T_2	Transverse relaxation time [s]
x	Horizontal coordinate [cm]
w	Transformed horizontal coordinate

Subscripts	
n	Number indicating chain length
1	Acrylamide
2	Bisacrylamide
3	Newly crosslinked unit without a neighbouring PDB (only L_3^p)

Superscripts	
•	Radical species
w	Aqueous phase
p	Polymer phase

Greek	
Γ	Fraction of total delivered dose
γ	Gamma radiation
$\lambda_{i,j}$	Moments of the water soluble growing radical distribution (i=0,1,2) with the active radical on an acrylamide (j=1) or bisacrylamide (j=2) unit
ϕ	Volume fraction of the reaction volume occupied by the aqueous phase
θ	Fraction of gelatin radicals that can re-initiate polymerization
Φ_i	Ratio of the concentration of species i in the polymer-phase over the concentration of the same species in the aqueous phase

Acronyms	
Aam	Acrylamide monomer
Bis	*N,N*'-methylene-bisacrylamide crosslinker
CT	Computed Tomography
Gy	Gray, unit for radiation dose (= J kg^{-1})
MeV	Mega-electronvolt
MRI	Magnetic Resonance Imaging
MV	Megavolt
NIPAM	*N*-isopropylacrylamide monomer
PAG	Polyacrylamide gel
PDB_e	Pendant double bond available for crosslinking
PDD	Percent depth-dose
PDE	Partial differential equation
THPC	Tetrakis (hydroxymethyl) phosphonium chloride

Chapter 1

Introduction

According to Canadian Cancer Statistics (Canadian Cancer Society 2010), over 173,000 new cases of cancer along with over 75,000 cancer deaths are expected in Canada in 2010. Clinical radiation therapy is an important and frequently used cancer treatment method (Zhang-Salomons and Mackillop 2008). The radiotherapy equipment irradiates the tumour, and to a lesser extent, the surrounding normal tissue. It is imperative that the correct radiation dose be delivered throughout the tumour volume, while minimizing any harm to surrounding healthy tissue. To ensure proper radiation delivery, the radiotherapy equipment must be tested and calibrated.

Polymer gel dosimetry systems provide an effective means for medical physicists to detect and verify three-dimensional (3D) radiation dose distributions delivered by clinical radiotherapy equipment (Baldock *et al.* 2010). These dosimeters are essentially small polymerization vessels, which respond to radiation and are able to capture and store information pertaining to the amount of radiation absorbed at different locations in 3D. Free radicals, generated by water radiolysis in the aqueous dosimeter solution, initiate polymerization and crosslinking reactions that form densely crosslinked polymer microgels. More polymer is formed in high-dose regions of the dosimeter than in regions where the dose is low. The polymer precipitates from the aqueous phase and is held in place by the gelatin matrix, which is able to hold the spatial dose information (Baldock *et al.* 1998, Maryanski *et al.* 1993). The precipitated polymer has different properties than the surrounding aqueous solution and can be detected using a variety of 3D imaging techniques. Note that radiation doses are specified in units of Gray (Gy), where 1 Gy corresponds to 1 Joule of ionizing radiation delivered per kg of sample.

Despite their great promise, some issues remain unresolved, and have so far prevented a widespread application of polymer gel dosimeters. For example, acrylamide (Aam) is a severe neurotoxin and potential carcinogen (Papagiannis *et al.* 2006, Ibbott 2004), which makes PAG dosimeters inconvenient to manufacture, use, and dispose of in routine clinical applications. Over the years, much research has gone into developing improved polymer gel dosimeters (Baldock et al. 2010). These efforts include optimizing dosimeter recipes to reduced toxicity (Senden *et al.* 2006, Pappas *et al.* 2001), and to obtain improve dose response by increasing dose sensitivity and enhancing dose resolution (Jirasek *et al.* 2010, Koeva *et al.* 2009a, Venning *et al.* 2005). Dose sensitivity is defined as the change in imaging readout per unit of absorbed dose, while dose resolution is defined as the minimum detectable difference between two absorbed doses (Gustavsson *et al.* 2004).

In recent years, normoxic polymer gel dosimeters, manufactured under normal atmospheric conditions with an oxygen scavenger (e.g. Tetrakis(hydroxymethyl)phosphonium chloride (THPC)) have become popular due to their low sensitivity to oxygen (a free-radical polymerization inhibitor) and convenient preparation outside of a glove box (oxygen-free atmosphere) (Senden *et al.* 2006, Jirasek *et al.* 2006, Venning *et al.* 2005, De Deene *et al.* 2002, 2006, Fong *et al.* 2001). Limited water solubility of the *N,N'*-methylene-bisacrylamide (Bis) crosslinker in polymer gel dosimeters has also been an important concern. Approaches for possible Bis replacements and ways of increasing the solubility of Bis have been studied (Jirasek *et al.* 2009, 2010, Koeva *et al.* 2008, Senden *et al.* 2006).

Other factors that can affect the polymerization and response of polymer gel dosimeters are primarily concerned with the temporal and spatial stability of the 3-D dose distribution. These problems are caused by temperature changes during gelatin setting and polymerization (De Deene *et al.* 2006, Salomons *et al.* 2002, Maryanski *et al.* 1994), chemical reactions after irradiation

stops (due to long-lived radicals) (De Deene *et al.* 2000), and monomer diffusion (De Deene 2006, De Deene *et al.* 2001, Maryanski *et al.* 1994). Some of these problems have been studied through the use of mathematical models (Vergote *et al.* 2004, Fuxman *et al.* 2003, 2005).

Depending on the type of radiation equipment used, the ionizing radiation may be delivered as γ rays, x-ray photon beams or electron beams. Different types of radiation tend to penetrate the human body to different depths and are used in different cancer treatment applications (Khan 2009, Woods and Pikaev 1993). The goal of the research in Chapter 2 is to extend an existing mathematical model (Fuxman *et al.* 2005) to describe the kinetic processes occurring in irradiated polymer gel dosimeters. The extended model accounts for depth-dose information from a number of clinically-relevant radiation beams. This model provides a better understanding of potential limitations arising from temporal and spatial inaccuracies caused by monomer diffusion and temperature effects when using depth-dose behaviour to create polymer gel calibrations. Simulation results of predicted mass of polymer formed indicate that both diffusion and temperature effects should be considered when calibrating polymer gel dosimeters.

The traditional imaging technique for polymer gel dosimeters has been Magnetic Resonance Imaging (MRI) (Ibbott *et al.* 1997, Bladock *et al.* 1996, Maryanski *et al.* 1993, 1996a, Gore *et al.* 1984). Recent work has explored the promise of x-ray computed tomography (CT) (Hilts and Jirasek 2008, Baxter *et al.* 2007, Hilts 2006, Trapp *et al.* 2001, 2002, Hilts *et al.* 2000) as an alternative imaging modality. X-ray CT is easy to use, robust, and in many countries, much more accessible than MRI. Therefore, in addition to the modelling work, new polymer gel dosimeter formulations are developed and investigated, in attempts to improve the dose response performance and accuracy for calibration using x-ray CT imaging. Chapter 3 of this thesis explores a range of NIPAM gel formulations with increased Bis solubility by using NIPAM as a cosolvent. Promising results were obtained and a new polymer gel dosimeter recipe is proposed

for use with x-ray CT imaging. Overall conclusions based on experimental work and simulation results, along with recommendations for future work, are presented in Chapter 4.

1.1 References for Chapter 1

Baldock C, De Deene Y D, Doran S, Ibbott G, Jirasek A, Lepage M, McAuley K B, Oldham M and Schreiner L J 2010 Polymer gel dosimetry *Phys. Med. Biol.* **55** R1-63

Baldock C, Burford R P, Billingham N, Wagner G S, Patval S, Badawi R D and Keevil S F 1998 Experimental procedure for the manufacture and calibration of polyacrylamide gel (PAG) for magnetic resonance imaging (MRI) radiation dosimetry *Phys. Med. Biol*. **43** 695-702

Baldock C, Burford R P, Billingham N C, Cohen D and Keevil S F 1996 Polymer gel composition in magnetic resonance imaging dosimetry *Med. Phys.* **23** 1070

Baxter P, Jirasek A and Hilts M 2007 X-ray CT dose in normoxic polyacrylamide gel dosimetry *Med. Phys*. **34** 1934–43

Canadian Cancer Society's Steering Committee 2010 *Canadian Cancer Statistics 2010* (Toronto: Canadian Cancer Society)

De Deene Y 2006 On the accuracy and precision of gel dosimetry *J. Phys.: Conf. Ser.* **56** 72-85

De Deene Y, Vergote K, Claeys C and De Wagter C 2006 The fundamental radiation properties of normoxic polymer gel dosimeters: a comparison between a methacrylic acid based gel and acrylamide based gels *Phys. Med. Biol.* **51** 653-73

De Deene Y, Hurley C, Venning A, Vergote K, Mather M, Healy B J and Baldock C 2002 A basic study of some normoxic polymer gel dosimeters Phys. Med. Biol. 47 3441-63

De Deene Y, Reynaert N and De Wagter C 2001 On the accuracy of monomer/polymer gel dosimetry in the proximity of a high-dose-rate ^{192}Ir source *Phys. Med. Biol.* **46** 2801-25

De Deene Y, Hanselaer P, De Wagter C, Achten E and De Neve W 2000 An investigation of the chemical stability of a monomer/polymer gel dosimeter Phys. Med. Biol. **45** 859-78

Fong P M, Keil D C, Does M D, Gore J C 2001 Polymer gels for magnetic resonance imaging of radiation dose distributions at normal room atmosphere *Phys. Med. Biol.* **46** 3105-13

Fuxman A M, McAuley K B and Schreiner L J 2005 Modelling of polyacrylamide gel dosimeters with spatially non-uniform radiation dose distributions *Chem. Eng. Sci*. **60** 1277-93

Gore J C, Kang Y S and Schulz R J 1984 Measurement of radiation dose distributions by nuclear magnetic resonance (NMR) imaging *Phys. Med. Biol*. **29** 1189-97

Guo P, Adamovics J and Oldham M 2006 A practical three-dimensional dosimetry system for radiation therapy *Med. Phys.* **33** 3962-72

Gustavsson H, Back S A J, Lepage M, Rintoul L and Baldock C 2004 Development and optimization of a 2-hyrdoxyethylacrylate MRI polymer gel dosimeter *Phys. Med. Biol.* **49** 227-41

Hilts M and Jirasek A 2008 Adaptive mean filtering for noise reduction in CT polymer gel dosimetry *Med. Phys.* **35** 344-55

Hilts M 2006 X-ray computed tomography imaging of polymer gel dosimeters *J. Phys.: Conf. Ser*. **56** 95–107

Hilts M, Audet C, Duzenli C and Jirasek A 2000 Polymer gel dosimetry using x-ray computed tomography: a feasibility study *Phys. Med. Biol.* **45** 2559-71

Ibbott G, Maryanski M J, Eastman P, Holcomb S D, Zhang Y, Avison R G, Sanders M and Gore J C 1997 Three-dimensional visualization and measurement of conformal dose distributions using magnetic resonance imaging of BANG polymer gel dosimeters *Int. J. Radiat. Oncol. Biol. Phys.* **38** 1097-103

Jirasek A, Hilts M and McAuley K B 2010 Polymer gel dosimeters with enhanced sensitivity for use in x-ray CY polymer gel dosimetry *Phys. Med. Biol.* **55** 5269-81

Jirasek A, Hilts M, Berman A and McAuley K B 2009 Effects of glycerol co-solvent on the rate and form of polymer gel dose response *Phys. Med. Biol.* **54** 907-18

Jirasek A, Hilts M, Shaw C and Baxter P 2006 Investigation of tetrakis hydroxymethyl phosphonium chloride as an antioxidant for use in x-ray computed tomography polyacrylamide gel dosimetry *Phys. Med. Biol.* **51** 1891-906

Khan F M 2009 *The physics of radiation therapy, 4th ed* (Philadelphia, PA: Lippincott Williams & Wilkins)

Koeva V I, Olding T, Jirasek A, Schreiner L J and McAuley K B 2009a Preliminary investigation of the NMR, optical and x-ray CT dose-response of polymer gel dosimeters incorporating cosolvents to improve dose sensitivity *Phys. Med. Biol.* **54** 2779-90

Koeva V I, Daneshvar S, Senden R J, Imam A H M, Schreiner L J and McAuley K B 2009b Mathematical modeling of PAG- and NIPAM-based polymer gel dosimeters contaminated by oxygen and inhibitor *Macromol. Theory Simul*. **18** 495-510

Koeva V I, Csaszar E S, Senden R J, McAuley K B and Schreiner L J 2008 Polymer gel dosimeters with increased solubility: a preliminary investigation of the NMR and optical dose-response using different crosslinkers and co-solvents *Macromol. Symp.* **261** 157-66

Maryanski M J, Ibbott G S, Eastman P, Schulz R J and Gore J C 1996a Radiation therapy dosimetry using magnetic resonance imaging of polymer gels *Med. Phys.* **23** 699-705

Maryanski M J, Zastavker Y Z and Gore J C 1996b Radiation dose distributions in three dimensions from tomographic optical density scanning of polymer gels: II. Optical properties of the BANG polymer gel *Phys. Med Biol.* **41** 2705-17

Maryanski M J, Schulz R J, Ibbott G S, Gatenby J C, Xie J, Horton D and Gore J C 1994 Magnetic resonance imaging of radiation dose distributions using a polymer-gel dosimeter *Phys. Med. Biol.* **39** 1437-55

Maryanski M J, Gore J C, Kennan R P and Schulz R J 1993 NMR relaxation enhancement in gels polymerized and cross-linked by ionizing radiation: a new approach to 3D dosimetry by MRI *Magn. Reson. Imaging*. **11** 253-8

Oldham M, Sakhalkar H, Guo P and Adamovics J 2008 An investigation of the accuracy of an IMRT dose distribution using two- and three-dimensional dosimetry techniques *Med. Phys.* **35** 2072-80

Pappas E, Seimenis I, Angelopoulos A, Georgolopoulou P, Kamariotaki-Paparigopoulou M, Maris T, Sakelliou L, Sandilos P and Vlachos L 2001 Narrow stereotactic beam profile measurements using N-vinylpyrrolidone based polymer gels and magnetic resonance imaging *Phys. Med. Biol.* **46** 783-97

Sakhalkar H S, Adamovics J, Ibbott G and Oldham M 2009 A comprehensive evaluation of the PRESAGE/optical-CT 3D dosimetry system *Med. Phys.* **36** 71-82

Salomons G J, Park Y S, McAuley K B and Schreiner L J 2002 Temperature increases associated with polymerization of irradiated PAG dosimeters *Phys. Med. Biol*. **47** 1435-48

Senden R J, De Jean P, McAuley K B and Schreiner L J 2006 Polymer gel dosimeters with reduced toxicity: a preliminary investigation of the NMR and optical dose-response using different monomers *Phys. Med. Biol.* **51** 3301-14

Trapp J V, Back S A J, Lepage M, Michael G and Baldock C 2001 An experimental study of the dose response of polymer gel dosimeters imaged with x-ray computed tomography *Phys. Med. Biol.* **46** 2939-51

Venning A J, Hill B, Brindha S, Healy B J and Baldock C 2005 Investigation of the PAGAT polymer gel dosimeter using magnetic resonance imaging *Phys. Med. Biol.* **50** 3875-88

Vergote K, De Deene Y, Vanden Bussche E and De Wagter C 2004 On the relation between the spatial dose integrity and the temporal instability of polymer gel dosimeters *Phys. Med. Biol*. **49** 4507-22

Wai P, Adamovics J, Krstajic N, Ismail A, Nisbet A and Doran S 2009 Dosimetry of the microSelectron-HDR Ir-192 source using PRESAGE ™ and optical CT *Appl. Radiat. Isot.* **67** 419-22

Woods R and Pikaev A 1993 *Applied Radiation Chemistry* (New York: Wiley)

Zang-Salomons J and Mackillop W J 2008 Estimating the lifetime utilization rate of radiotherapy in cancer patients: The Multicohort Current Utilization Table (MCUT) method *Comput. Methods Prog. Biomed.* **92** 99-108

Chapter 2

Kinetic model development for depth-dose response

2.1 Chapter Overview

In this chapter, an existing kinetic model is extended to incorporate depth-dose information as a form of spatially non-uniform irradiation. Model predictions of the type and amount of polymer formed are presented to show the behaviour of PAG dosimeters, under the influence of monomer diffusion and temperature effects.

The material presented in this chapter will be submitted to *Macromolecular Theory and Simulation* and appears in manuscript form.

Mathematical modelling of depth-dose response of polymer gel dosimeters

J N M Chain[1], A T Nasr[1], L J Schreiner[2,3], K B McAuley[1]

[1] Dept. of Chemical Engineering, Queen's University, Kingston, Canada, K7L 3N6

[2] Cancer Centre of Southeastern Ontario, Kingston, Canada, K7L 5P9

[3] Depts. of Oncology and Physics, Queen's University, Kingston, Canada, K7L 3N6

2.2 Summary

A dynamic partial differential equation (PDE) model is extended and used to simulate the effects of radiation depth doses on polymer formation in Polyacrylamide Gel (PAG) dosimeters. Depth doses are simulated using different types of radiation including Co60 gamma and 6 and 15 MV x-ray photon beams, along with 6, 9, 12, 16 and 20 MeV electron beams. Effects of monomer diffusion (edge enhancement) and temperature are studied. Diffusion results in excess polymer formation at the position of maximum dose (2.6 % for Co^{60} gamma radiation and less for other types of radiation studied). Temperature increases on the order of 2 °C increase the mass of polymer formed by approximately 1.25 %. These results provide insight for calibrating dosimeters using depth-dose information.

2.3 Introduction

Clinical radiation therapy is often used for cancer treatment (Zhang-Salomons and Mackillop 2008). Since the radiotherapy equipment irradiates the tumour, and to a lesser extent, the surrounding normal tissue, it is important that the correct dose be delivered throughout the entire

tumour volume, while minimizing the irradiation of non-cancerous cells. Polymer gel dosimeters have been developed as an effective means of detecting and verifying radiation dose distributions of three-dimensional (3D) radiotherapy treatments (Baldock *et al.* 2010). These dosimeters capture and store information on the amount of radiation absorbed at each location using dose-dependent polymerization of monomers dispersed in an irradiated gel substrate.

Polyacrylamide gel (PAG) dosimeters, which consist of acrylamide (Aam) monomer and *N,N'*-methylene-bisacrylamide (Bis) crosslinker dissolved in an aqueous gelatin matrix, are the most studied and widely used polymer gel dosimeters (De Deene *et al.* 2006, Venning *et al.* 2005, Maryanski *et al.* 1993). Free radicals are generated when radiation is absorbed by water molecules in the aqueous dosimeter solution. These free radicals induce polymerization and crosslinking of the water-soluble monomers. More polymer is formed in locations receiving higher amounts of radiation. The crosslinked polymer precipitates from the aqueous phase and is held in place by the gelatin matrix, thereby storing spatial information on the amount of radiation delivered (Baldock *et al.* 1998, Maryanski *et al.* 1993). A typical PAG dosimeter recipe is shown in Table 2.1 (Baldock *et al.* 1998, Maryanski *et al.* 1994). Note that the main component of the dosimeter is water, which leads to nearly water-equivalent or tissue-equivalent dose absorption behaviour for the types of ionizing radiation used in cancer treatments (De Deene 2004).

Table 2.1: Typical PAG dosimeter recipe.

Component	Quantity (wt %)
Monomer (Aam or NIPAM)	3
Crosslinker (Bis)	3
Gelatin	5
Water	89

PAG dosimeters continue to be used and studied despite Aam being a severe neurotoxin and potential carcinogen (Papagiannis *et al.* 2006, Ibbott 2004). Alternative monomers have been examined as a suitable replacement for Aam, with *N*-isopropyl acrylamide (NIPAM) showing the best result with similar polymerization kinetics (Senden *et al.* 2006). NIPAM-based gel dosimeters have reduced safety concerns associated with the careful handling of the highly toxic Aam, and are currently being used and studied (Jirasek *et al.* 2010, Koeva *et al.* 2009a, Olding *et al.* 2009).

Oxygen, which has the ability to quickly consume primary radicals, is a well-known free-radical polymerization inhibitor (Odian 1991, Rudin 1982). The performance of polymer gel dosimeters is greatly affected by oxygen contamination (Salomons *et al.* 2002, McJury *et al.* 1999, 2000, Hepworth *et al.* 1999), where even small amounts of oxygen can significantly inhibit polymerization. Oxygen levels in dosimeters can vary depending on manufacturing and storage procedures, leading to variable dosimetry results. It is therefore imperative to effectively remove oxygen from polymer gel dosimeters. Traditionally, an inert gas was bubbled through gel solutions to remove oxygen (Baldock *et al.* 1998). The resulting dosimeters are called anoxic.

Alternatively, oxygen scavengers, of which Tetrakis(hydroxymethyl)phosphonium chloride (THPC) is the most commonly used, have been introduced as a means of consuming dissolved oxygen in dosimeter phantoms (Senden *et al.* 2006, Jirasek *et al.* 2006, Venning *et al.* 2005, De Deene *et al.* 2002, 2006, Fong *et al.* 2001). Dosimeters prepared under normal atmospheric conditions using an oxygen scavenger are called normoxic.

The precipitated polymer has different properties than the surrounding aqueous solution, making detection possible using a variety of 3D imaging techniques including Magnetic Resonance Imaging (MRI) (Ibbott *et al.* 1997, Baldock *et al.* 1996, Maryanski *et al.* 1993, 1996a, Gore *et al.* 1984), optical Computed Tomography (CT) (Wai *et al.* 2009, Sakhalkar *et al.* 2009, Oldham *et al.* 2008, Guo *et al.* 2006, Maryanski *et al.* 1996b) and x-ray CT (Hilts and Jirasek 2008, Baxter *et al.* 2007, Hilts 2006, Trapp *et al.* 2001, 2002, Hilts *et al.* 2000). To determine the amount of radiation that was absorbed at each location, a calibration procedure must be performed.

The traditional calibration process involves calibration vials that have been uniformly irradiated using different radiation doses, which are measured in units of gray (Gy), as shown in Figure 2.1 (Oldham *et al.* 1998, Baldock *et al.* 1998, Ibbott *et al.* 1997). The dose-dependent physical properties of the contents of each vial are measured using the desired readout method (MRI, optical CT or x-ray CT) and a calibration curve is constructed. Figure 2.2 shows a typical MRI calibration curve for a PAG dosimeter from Table 2.1. This dose-response curve allows subsequent determination of the radiation dose delivered to each voxel in non-uniformly irradiated polymer gel phantoms, like the one shown in Figure 2.3, based on MRI readout of transverse relaxation rate, R_2, at different spatial locations.

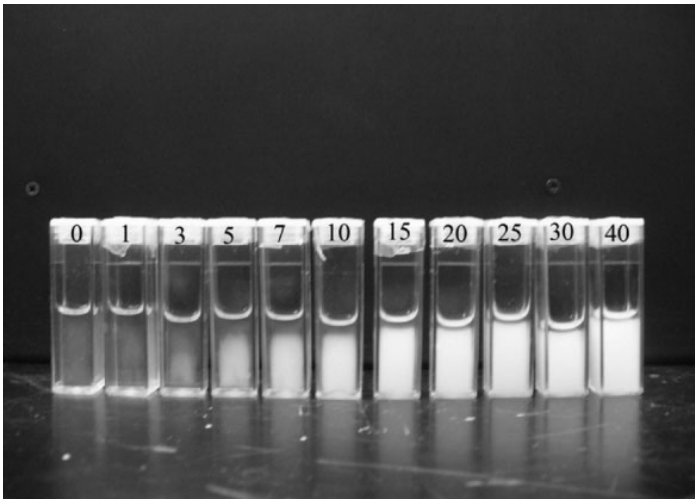

Figure 2.1: Photograph of uniformly irradiated calibration vials for polymer gel dosimetry. Radiation was delivered from 0 Gy to 40 Gy (Koeva *et al.* 2009b).

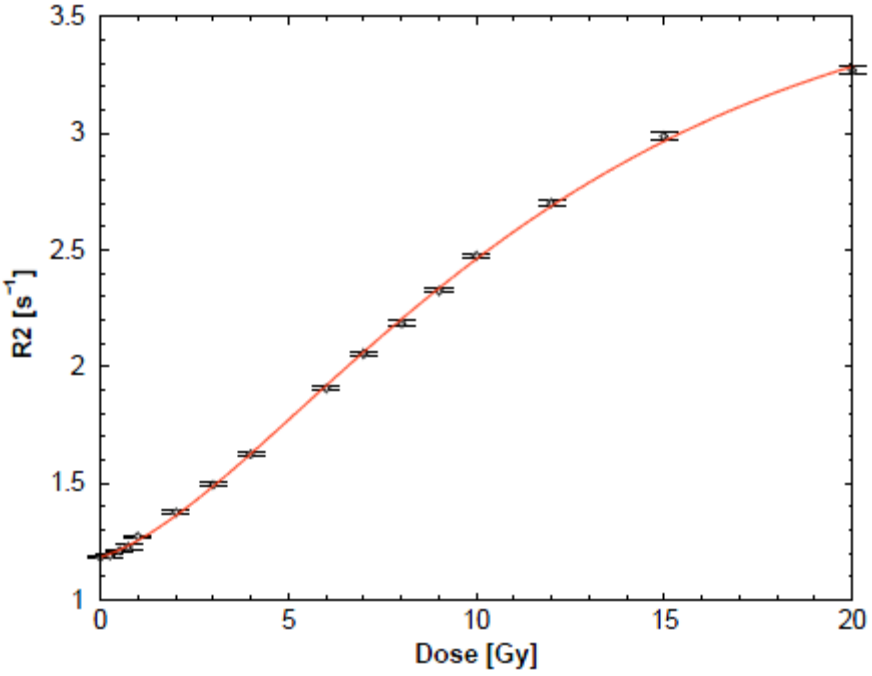

Figure 2.2: Calibration curve for a typical anoxic PAG dosimeter produced using the recipe in Table 2.1. (De Deene 2004)

Figure 2.3: Photograph of a non-uniformly irradiated polymer gel dosimeter phantom of approximately 1 L. The white regions, which received higher radiation dose, contain more precipitated polymer than the surrounding transparent gel.

Inaccuracies can arise when small calibration vials are used to produce calibration curves for computing 3D dose distributions in larger phantoms like the one shown in Figure 2.3. These inaccuracies arise from a variety of sources including different temperature histories during gel manufacture and different levels of oxygen contamination (De Deene 2006, Dumas *et al.* 2006). An alternative calibration method that may provide more reliable results involves use of radiation depth-dose information to create dose-response curves (Jirasek *et al.* 2010, Hilts *et al.* 2000, Oldham *et al.* 1998). In this approach, the same size of container is used for both calibration and for dose detection, thereby eliminating container-dependent temperature and oxygen contamination issues.

2.3.1 Depth-dose behavior in water

The amount of radiation energy absorbed in water varies with depth along a radiation beam, such that the dose absorbed near the surface can be significantly different than the dose absorbed deeper within the volume (Khan 2009, Woods and Pikaev 1993, Andrews *et al.* 1957). Typical percent depth-dose (PDD) data (Figure 2.4) used in the current study were obtained from clinical measurements for different types of radiation used in cancer treatment (Baldock *et al.* 2010). An explanation of the physics behind this depth-dose behaviour is provided by Khan (2009). Based on these PDD data, the amount of delivered radiation is known at different depths when simple radiation beams are delivered to polymer gel phantoms. To construct a calibration curve, a pencil beam of radiation (or several overlapping pencil beams) is used to irradiate a portion of a large gel phantom, (Jirasek *et al.* 2010, Hilts *et al.* 2000). The dosimeter response (e.g. R_2) is plotted vs. the known absorbed dose for a variety of points along the beam.

2.3.2 Modelling of polymer gel dosimeters

Dynamic mathematical models have previously been developed for PAG dosimeters, describing the kinetic mechanisms, chemical reactions and temperature changes for radiation-induced polymerization and crosslinking of Aam and Bis, for both spatially uniform (Koeva *et al.* 2009b, Fuxman *et al.* 2003) and non-uniform (Fuxman *et al.* 2005, Vergote *et al.* 2004) radiation doses. Measurements and modelling have shown that in non-uniform conditions with large dose gradients, the amount of polymer that forms at the edge of an irradiated zone may be enhanced by monomer diffusing from low dose areas (Fuxman *et al.* 2005, Vergote *et al.* 2004). The temporal stability of polymer gel dosimeters has also been investigated using these models, which show how radicals can persist in phantoms for extended periods of time (e.g. more than twelve hours), leading to additional polymerization and changes in resulting imaging readouts for many hours after radiation delivery ceases (Fuxman *et al.* 2003, 2005, Lepage *et al.* 2001b). Koeva *et al.*

(2009b) extended the model developed by Fuxman *et al.* (2003) to include the effects of oxygen inhibition and an inhibitor (monomethyl ether hydroquinone) found in many water-soluble monomers. New parameter estimates were also obtained by Koeva *et al.* (2009b) using experimental data (Babic and Schreiner 2006, Salomons *et al.* 2002).

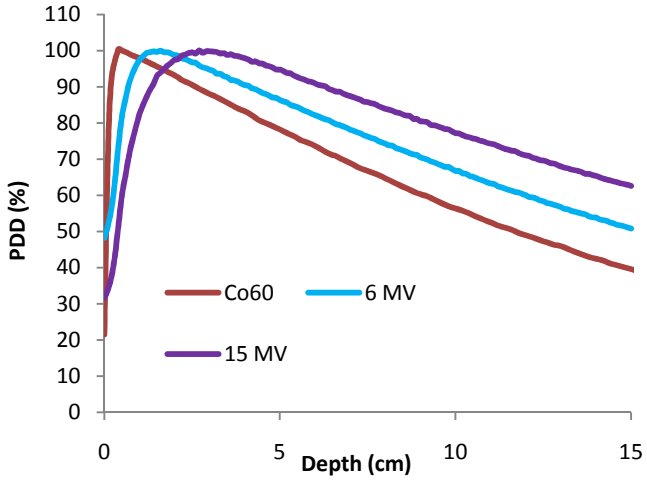

(a)

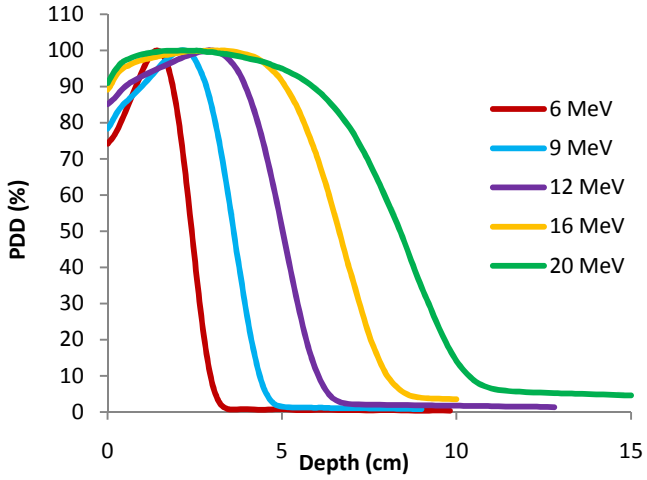

(b)

Figure 2.4: Percent depth-dose data by: (a) Co^{60} γ-radiation and 6 and 15 MV X-ray photon beams; (b) 6, 9, 12, 16 and 20 MeV electron beams.

When modeling polymerization in gel dosimeters, it is important to consider both the aqueous phase, and the polymer phase that forms due to precipitation of crosslinked polymer microgels (Fuxman *et al.* 2003). Reactions that occur in both phases include: radical generation by water radiolysis, initiation of polymer chains, propagation, intramolecular cyclization, intermolecular crosslinking, termination by disproportionation, chain transfer to both monomer and gelatin, and re-initiation by gelatin-centred radicals (Koeva *et al.* 2009b, Fuxman *et al.* 2003, 2005, Fuxman 2003). A list of assumptions made in the development of these models is provided by Fuxman *et al.* (2003, 2005) and in Appendix A.

The objectives of the current chapter are to: i) extend the model of Fuxman *et al.* (2005) to simulate the influence of depth-dose behaviour on polymerization and crosslinking in PAG dosimeters, and ii) to use the simulation results to explore the influence of monomer diffusion and reaction temperature effects on the accuracy of depth-dose calibration (De Deene 2006, Oldham *et al.* 1998). Predictions of chemical species concentrations and temperature at various depths are made for simulations using Co^{60} γ-radiation, 6 and 15 MV X-ray photon beams, and 6 MeV to 20 MeV electron beams. The current research focuses on the traditional PAG dosimeter recipe from Table 2.1, but the model could also be used to simulate NIPAM-based dosimeters and PAG dosimeters with other recipes.

2.4 Development of extended model

Partial differential equation (PDE) material balances on chemical species in aqueous and polymer phases of PAG dosimeters account for polymerization reactions, phase volume changes and mass transfer of species between phases (Fuxman *et al.* 2005). A PDE energy balance is used to determine the temperature distribution within the phantom. The original PDEs developed by Fuxman *et al.*, with associated reaction rates and boundary and initial conditions are found in

Tables 3 to 6 of Fuxman *et al.* (2005) and Table 4.6 of the associated thesis (Fuxman, 2003). Updated values of model parameters obtained by Koeva *et al.* (2009b) are used in the extended model and are provided in Appendix D.

The equations and settings described above form the basis of the current research. However, in the extended model, boundary conditions are revised to permit heat loss through the front and back walls of the phantom. The new boundary condition for the energy balance is given by equation (1):

$$k_{\text{cond}} \left.\frac{\partial T}{\partial x}\right|_{x=0} = h(T - T_s) \tag{1}$$

where k_{cond} is the thermal conductivity of the gel in the phantom, T is the temperature, x is the horizontal spatial dimension, which takes values of zero to d_b as shown in Figure 2.5, h is a convective heat-transfer coefficient, and T_s is the temperature outside of the wall of the vessel. All other boundary conditions remain unchanged and are provided in Appendix G.

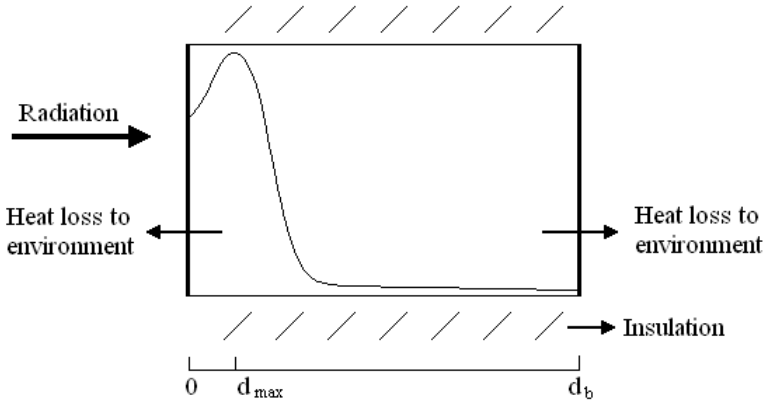

Figure 2.5: Schematic diagram of the irradiation of a simulated phantom with a PDD curve, where d_{max} represents the location of maximum absorbed dose, and d_b is the depth of the back wall. All simulations use a value of d_b = 10 cm.

The extended model also requires a minor modification to the PDE material balance on primary radicals generated by water radiolysis:

$$\frac{\partial[(\mathrm{PR}^{\cdot})]}{\partial t} = \Gamma(x) R_{(\mathrm{PR}^{\cdot})}[\mathrm{H_2O}] M_{w,\mathrm{H_2O}} - r_{(\mathrm{PR}^{\cdot})} - \frac{[(\mathrm{PR}^{\cdot})]}{\phi}\frac{\partial \phi}{\partial t} \qquad (2)$$

where [(PR$^{\bullet}$)] is the concentration of primary radicals, $\Gamma(x)$ identifies zones receiving or not receiving radiation, $R_{(\mathrm{PR}\bullet)}$ is the rate of generation of primary radicals, [H_2O] is the concentration of water in the aqueous phase, $M_{w,H2O}$ is the molecular weight of water, ϕ is the local volume fraction occupied by the aqueous phase and $r_{(\mathrm{PR}\bullet)}$ is the rate of consumption of primary radicals by subsequent reactions. When studying edge enhancement at a sharp interface between irradiated and un-irradiated zones, Fuxman *et al.* (2005) used $\Gamma(x)$ to distinguish locations that receive radiation ($\Gamma(x) = 1$) from locations that do not ($\Gamma(x) = 0$). In the current work, which is concerned with radical generation rates that vary with depth, $\Gamma(x)$ is used to input depth-dose information into the model. Note that a typographical error appeared in the material balance on pendant double bonds in the polymer phase in the earlier article (Fuxman *et al.* 2005). The correct version is:

$$\frac{\partial[\mathrm{PDB}_e^p]}{\partial t} = r_{\mathrm{PDB}_e^p} + n_{\mathrm{PDB}}\left\{\left(k_{x1}^w[S_{1,n}^w] + k_{x2}^w[S_{2,n}^w]\right)([\mathrm{PDB}_e^w])\right\}\frac{\phi}{(1-\phi)} + \frac{[\mathrm{PDB}_e^p]}{(1-\phi)}\frac{\partial \phi}{\partial t} \qquad (3)$$

Definitions for all symbols are provided in the Nomenclature and a complete list of model equations is provided in Appendix G. Several additional reactions are considered in the extended model, which were neglected by Fuxman *et al.* (2005). These new reactions indicate that it is possible for gelatin radicals to consume radicals attached to polymer chains, in both phases. Termination reactions with gelatin generate dead polymer chains.

$$S_{1,n}^{w} + G^{\cdot w} \xrightarrow{k_{t12}^{w}} D_{n}^{w} \tag{4}$$

$$S_{2,n}^{w} + G^{\cdot w} \xrightarrow{k_{t22}^{w}} D_{n}^{w} + \mathrm{PDB}_{e}^{w} \tag{5}$$

$$L_{1}^{p} + G^{\cdot p} \xrightarrow{k_{t12}^{P}} D^{P} \tag{6}$$

$$L_{2}^{p} + G^{\cdot p} \xrightarrow{k_{t22}^{P}} D^{P} + \mathrm{PDB}_{e}^{P} \tag{7}$$

Reaction rate equations, which were revised to include the influence of reactions (4) to (7) above, are shown in Table 2.2. All other reaction rate expressions remain the same as those of Fuxman *et al.* (2005). A complete list of reaction mechanisms and rate equations are provided in Appendix B and Appendix C. A summary of all modifications for the extended model is provided in Appendix E.

Table 2.2: Revised reaction rates which include the influence of new reaction mechanisms.

$$\begin{aligned} r_{S_1^w} = {} & \left\{k_{i1}[\mathrm{PR}^{\cdot w}][M_1^w] + \left(k_{p21}^w + k_{f21}^w\right)[S_2^w][M_1^w] + k_c^w[S_2^w] + k_{pG1}^w[G^{\cdot w}][M_1^w]\right\} \\ & - \left\{k_{t12}^w[G^{\cdot w}][S_1^w] + \left(k_{p12}^w + k_{f12}^w\right)[S_1^w][M_2^w] + k_{x1}^w[S_1^w][\mathrm{PDB}_e^w]\right. \\ & \left. + 2k_{t11}^w[S_1^w]^2 + k_{t12}^w[S_2^w][S_1^w] + k_{fG1}^w[G^w][S_1^w]\right\} \end{aligned} \tag{8}$$

$$\begin{aligned} r_{S_2^w} = {} & \left\{k_{i2}[\mathrm{PR}^{\cdot w}][M_2^w] + \left(k_{p12}^w + k_{f12}^w\right)[S_1^w][M_2^w] + k_{pG2}^w[G^{\cdot w}][M_2^w]\right\} \\ & - \left\{k_{t22}^w[G^{\cdot w}][S_2^w] + k_c^w[S_2^w] + \left(k_{p21}^w + k_{f21}^w\right)[S_2^w][M_1^w]\right. \\ & \left. + k_{x2}^w[S_2^w][\mathrm{PDB}_e^w] + 2k_{t22}^w[S_2^w]^2 + k_{t12}^w[S_2^w][S_1^w] + k_{fG2}^w[G^w][S_2^w]\right\} \end{aligned} \tag{9}$$

$$\begin{aligned} r_{\mathrm{PDB}_e^w} = {} & \left\{\left(k_{p21}^w + 2k_{f21}^w\right)[S_2^w][M_1^w] + \left(k_{p22}^w + 2k_{f22}^w\right)[S_2^w][M_2^w] + k_{t11}^w[S_1^w]^2\right. \\ & + k_{t22}^w[G^{\cdot w}][S_2^w] + 2k_{t12}^w[S_2^w][S_1^w] + 3k_{t22}^w[S_2^w]^2 + k_{fG2}^w[G^w][S_2^w] \\ & \left. + \left(k_{f11}^w[M_1^w] + k_{f12}^w[M_2^w]\right)[S_1^w]\right\} \\ & - \left(k_{x1}^w[S_1^w] + k_{x2}^w[S_2^w]\right)[\mathrm{PDB}_e^w](1 + n_{\mathrm{PDB}}) \end{aligned} \tag{10}$$

$$\begin{aligned} r_{G^{\cdot w}} = {} & \left\{[G^w]\left(\theta k_{fG1}^w[S_1^w] + \theta k_{fG2}^w[S_2^w]\right)\right\} \\ & - \left\{[G^{\cdot w}]\left(k_{pG1}^w[M_1^w] + k_{pG2}^w[M_2^w] + k_{t12}^w[S_1^w] + k_{t22}^w[S_2^w]\right)\right\} \end{aligned} \tag{11}$$

$$r_{L_1^p} = \{[M_1^P](k_{p21}^P[L_2^p] + k_{p21}^P[L_3^p] + k_{pG1}^P[G^{\cdot p}]) + k_c^P[L_2^p]\} - \{k_{p12}^P[M_2^P][L_1^p] + k_{x1}^P[\mathrm{PDB}_e^p][L_1^p] + (k_{f11}^P[M_1^p] + k_{f12}^P[M_2^p])[L_1^p] + 2k_{t11}^P[L_1^p]^2 + k_{t12}^P[L_1^p][L_2^p] + k_{t12}^P[L_1^p][G^{\cdot p}] + k_{fG1}^P[L_1^p][G^P]\} \quad (12)$$

$$r_{L_2^p} = \{[M_2^P](k_{p12}^P[L_1^p] + k_{p22}^P[L_3^p] + k_{pG2}^P[G^{\cdot p}])\} - \{k_c^P[L_2^p] + k_{p21}^P[M_1^P][L_2^p] + k_{x2}^P[\mathrm{PDB}_e^P][L_2^p] + (k_{f21}^P[M_1^p] + k_{f22}^P[M_2^p])[L_2^p] + 2k_{t22}^P[L_2^p]^2 + k_{t12}^P[L_1^p][L_2^p] + k_{t22}^P[L_2^p][G^{\cdot p}] + k_{fG2}^P[L_2^p][G^P]\} \quad (13)$$

$$r_{\mathrm{PDB}_e^p} = \{(k_{p21}^P + 2k_{f21}^P)[M_1^P][L_2^p] + (k_{p22}^P + 2k_{f22}^P)[M_2^P][L_2^p] + k_{t11}^P[L_1^p]^2 + k_{t22}^P[G^{\cdot p}][L_2^p] + 2k_{t12}^P[L_2^p][L_1^p] + 3k_{t22}^P[L_2^p]^2 + k_{fG2}^P[G^P][L_2^p]\} + (k_{f11}^P[M_1^p] + k_{f12}^P[M_2^p])[L_1^p] - \{(k_{x1}^P[L_1^p] + k_{x1'}^P[S_1^p])[\mathrm{PDB}_e^p]\} \quad (14)$$

$$r_{G^{\cdot p}} = \{[G^P](\theta k_{fG1}^P[L_1^p] + \theta k_{fG2}^P[L_2^p])\} - \{[G^{\cdot p}](k_{pG1}^P[M_1^P] + k_{pG2}^P[M_2^P] + k_{t12}^P[L_1^p] + k_{t22}^P[L_2^p])\} \quad (15)$$

2.5 Model solution

To model the depth-dose behaviour, the PDDs shown in Figure 2.6 must be approximated by equations, which can then be inserted as functions ($\Gamma(x)$) within the extended model. Cubic polynomial equations were fitted using the spline toolbox in Matlab™ (The Mathworks, Natick, MA, USA) to convert the experimental depth-dose data from the various radiation beams to a convenient functional form for use in the PDE model. More spline nodes were used near the depth of maximum dose (d_{max} in Figure 2.5) than where depth dose curves are smooth to ensure that accurate depth-dose information was provided to the model. Figure 2.6 shows the quality of a spline fit. All other spline fits are provided in Appendix F.

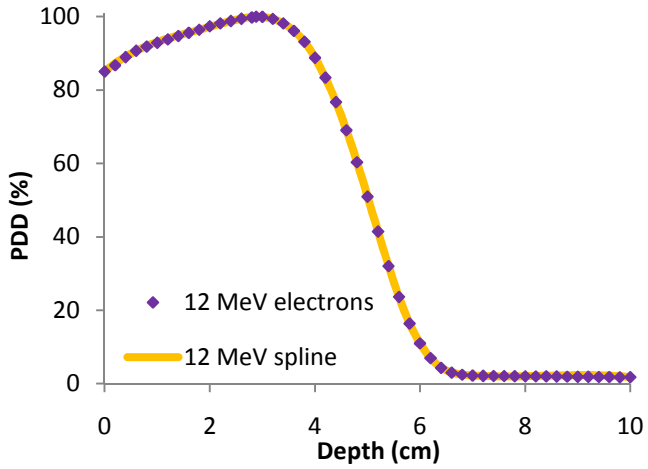

Figure 2.6: Plot comparing PDD data and spline fit for 12 MeV electron radiation. The cublic spline is nearly a perfect match for the experimental depth dose data.

The complete system of 31 PDEs (shown in Appendix D) was solved using the VLUGR2 solver within Fortran. VLUGR2 is a numerical solver, capable of solving initial value problems with boundary conditions, for systems of time-dependent PDEs having either one or two spatial dimensions (Blom *et al.* 1996). Note that the model equations can also be solved using the *pdepe* subroutine in Matlab™, but simulation times are prohibitively long. The PDEs were solved to predict the mass of polymer formed per unit volume of phantom at different depths. The type of polymer formed (e.g. the number of crosslinks per mass of polymer) and the temperature were also predicted as a function of depth and time.

Additional simulations were performed to examine the influence of monomer diffusion and temperature effects. Simulations with diffusion turned off (e.g. $D_{M1} = 0$) were compared with simulations that account for diffusion ($D_{M1} = 4.1 \times 10^{-6}$ cm^2/min). Simulations with heat effects turned off (T = 20°C everywhere) were compared with simulations that account for the heat released by polymerization. All simulations use a phantom depth of d_b = 10 cm. Radiation was

delivered until the total dose was 5 Gy at d_{max} for all types of radiation. Simulations for the Co^{60} γ-radiation used a dose rate of 2 Gy/min, while all other radiation beams had a dose rate of 4 Gy/min.

2.5.1 Transformed PDEs

The VLUGR2 algorithm solves PDEs on a spatial domain where the horizontal axis (w) extends from 0 to 1. Therefore, transformations on the PDEs were first performed so that the transformed axis is constrained between $w = 0$ and $w = 1$, rather than the actual depth of the phantom (from $x = 0$ to $x = d_b$=10). All terms within the PDEs which contained the original x coordinate were replaced by the transformed variable w. The model equations that required transformation are provided in Table 2.3. Only the PDEs of Fuxman *et al.* (2005) with partial derivatives with respect to x on the right hand side needed to transform.

$$w = \frac{x}{d_b} \tag{16}$$

$$\frac{\partial w}{\partial x} = \frac{1}{d_b} \tag{17}$$

$$\frac{\partial^2 w}{\partial x^2} = 0 \tag{18}$$

Boundary conditions were also transformed to account for the new spatial coordinates. The boundary conditions for heat loss through the front and back walls of the phantom become:

$$k_{\text{cond}} \frac{\partial T}{\partial w}\left(\frac{1}{d_b}\right)\Big|_{w=0} = h(T - T_s) \tag{19}$$

$$-k_{\text{cond}} \frac{\partial T}{\partial w}\left(\frac{1}{d_b}\right)\Big|_{w=1} = h(T - T_s) \tag{20}$$

A list of all PDEs and boundary conditions for the extended model are provided in Appendix G.

Table 2.3: Transformed species balance equations used in the current model.

$$\frac{\partial[\mathrm{PR}^{\cdot w}]}{\partial t} = D_{\mathrm{PR}^{\cdot}}\left(\frac{1}{d_b}\right)^2\left(\frac{1}{\phi}\frac{\partial\phi}{\partial w}\frac{\partial[\mathrm{PR}^{\cdot w}]}{\partial w} + \frac{\partial^2[\mathrm{PR}^{\cdot w}]}{\partial w^2}\right) + r_{\mathrm{PR}^{\cdot w}} - \frac{[\mathrm{PR}^{\cdot w}]}{\phi}\frac{\partial\phi}{\partial t} \tag{21}$$

$$\frac{\partial[M_1^w]}{\partial t} = D_{M_1^w}\left(\frac{1}{d_b}\right)^2\left(\frac{1}{\phi}\frac{\partial\phi}{\partial w}\frac{\partial[M_1^w]}{\partial w} + \frac{\partial^2[M_1^w]}{\partial w^2}\right) + r_{M_1^w} - k_m\left([M_1^w] - \frac{[M_1^p]}{\Phi_{\mathrm{M}_1}}\right) - \frac{[M_1^w]}{\phi}\frac{\partial\phi}{\partial t} \tag{22}$$

$$\frac{\partial[M_2^w]}{\partial t} = D_{M_2^w}\left(\frac{1}{d_b}\right)^2\left(\frac{1}{\phi}\frac{\partial\phi}{\partial w}\frac{\partial[M_2^w]}{\partial w} + \frac{\partial^2[M_2^w]}{\partial w^2}\right) + r_{M_2^w} - k_m\left([M_2^w] - \frac{[M_2^p]}{\Phi_{\mathrm{M}_2}}\right) - \frac{[M_2^w]}{\phi}\frac{\partial\phi}{\partial t} \tag{23}$$

$$\frac{\partial[S_1^w]}{\partial t} = D_{S_1^w}\left(\frac{1}{d_b}\right)^2\left(\frac{1}{\phi}\frac{\partial\phi}{\partial w}\frac{\partial[S_1^w]}{\partial w} + \frac{\partial^2[S_1^w]}{\partial w^2}\right) + r_{S_1^w} - \frac{[S_1^w]}{\phi}\frac{\partial\phi}{\partial t} \tag{24}$$

$$\frac{\partial[S_2^w]}{\partial t} = D_{S_2^w}\left(\frac{1}{d_b}\right)^2\left(\frac{1}{\phi}\frac{\partial\phi}{\partial w}\frac{\partial[S_2^w]}{\partial w} + \frac{\partial^2[S_2^w]}{\partial w^2}\right) + r_{S_2^w} - \frac{[S_2^w]}{\phi}\frac{\partial\phi}{\partial t} \tag{25}$$

$$\frac{\partial[\mathrm{PDB}_e^w]}{\partial t} = D_{\mathrm{PDB}^{\mathrm{w}}}\left(\frac{1}{d_b}\right)^2\left(\frac{1}{\phi}\frac{\partial\phi}{\partial w}\frac{\partial[\mathrm{PDB}_e^w]}{\partial w} + \frac{\partial^2[\mathrm{PDB}_e^w]}{\partial w^2}\right) + r_{\mathrm{PDB}_e^w} - \frac{[\mathrm{PDB}_e^w]}{\phi}\frac{\partial\phi}{\partial t} \tag{26}$$

$$\frac{\partial[\mathrm{H_2O}^w]}{\partial t} = D_{\mathrm{H_2O}^w}\left(\frac{1}{d_b}\right)^2\left(\frac{1}{\phi}\frac{\partial\phi}{\partial w}\frac{\partial[\mathrm{H_2O}^w]}{\partial w} + \frac{\partial^2[\mathrm{H_2O}^w]}{\partial w^2}\right) - k_m\left([\mathrm{H_2O}^w] - \frac{[\mathrm{H_2O}^p]}{\Phi_{\mathrm{H_2O}}}\right) - \frac{[\mathrm{H_2O}^w]}{\phi}\frac{\partial\phi}{\partial t} \tag{27}$$

$$\frac{\partial[D^w]}{\partial t} = D_{D^w}\left(\frac{1}{d_b}\right)^2\left(\frac{1}{\phi}\frac{\partial\phi}{\partial w}\frac{\partial[D^w]}{\partial w} + \frac{\partial^2[D^w]}{\partial w^2}\right) + r_{D^w} - \frac{[D^w]}{\phi}\frac{\partial\phi}{\partial t} \tag{28}$$

$$\frac{\partial\lambda_{i,j}}{\partial t} = D_{S_j^w}\left(\frac{1}{d_b}\right)^2\left(\frac{1}{\phi}\frac{\partial\phi}{\partial w}\frac{\partial\lambda_{i,j}}{\partial w} + \frac{\partial^2\lambda_{i,j}}{\partial w^2}\right) + r_{\lambda_{i,j}} - \frac{\lambda_{i,j}}{\phi}\frac{\partial\phi}{\partial t} \quad \text{for } i = 1,2;\ j = 1,2 \tag{29}$$

$$\frac{\partial T}{\partial t} = \left(\frac{k_{\mathrm{cond}}}{\rho C_p}\right)\left(\frac{1}{d_b}\right)^2\frac{\partial^2 T}{\partial w^2} + r_T\frac{(-\Delta H_r)}{\rho C_p} \tag{30}$$

2.6 Simulation results

2.6.1 Monomer consumption and polymer formed

The extended model is now used to simulate depth-dose behaviour of polymer gel dosimeters. Aam and Bis concentrations over time and depth in the aqueous phase when using Co^{60} γ-radiation are shown in Figure 2.7. The monomer concentration curves indicate that the maximum monomer consumption occurs near d_{max}. These simulation results also show the effect of long-lived radicals because monomer concentrations continue to decrease up to 24 hrs post-irradiation due to on-going polymerization.

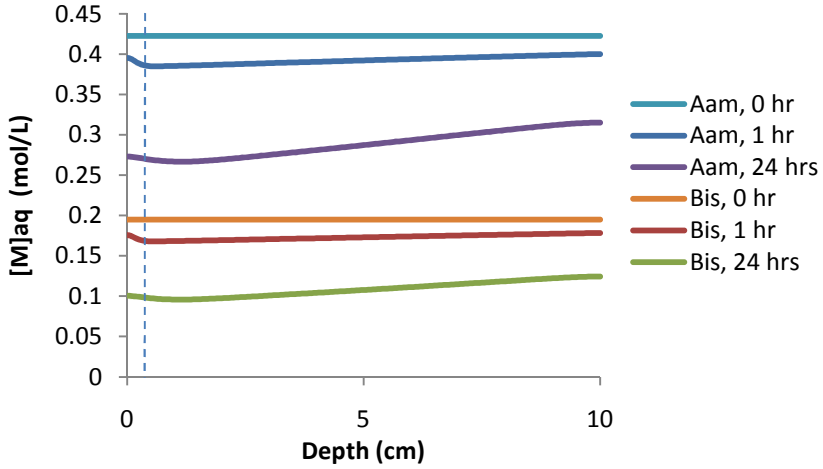

Figure 2.7: Aam and Bis concentrations for Co^{60} γ-radiation in the aqueous phase as a function of depth at different times. The dosimeter was irradiated at 2 Gy/min for 2.5 mins, but polymerization continued after irradiation ceased. The position d_{max} is indicated by the vertical dashed line.

Simulation results showing the amount of polymer formed 24 hours post irradiation are shown in Figure 2.8b along with the corresponding depth-dose curves in Figure 2.8a. The amount of polymer formed for each type of radiation has a shape similar to the corresponding depth-dose

curve. There are, however, some small differences between the shapes of the curves, especially near the position of maximum dose. For example, the polymer formation curve for Co^{60} γ-radiation has a more pronounced maximum than does its PDD curve.

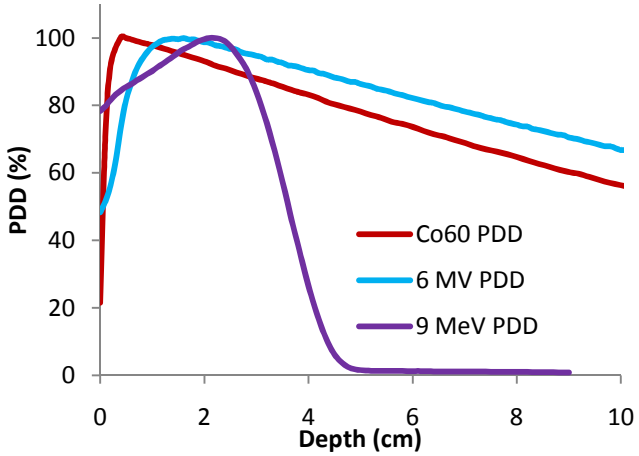

(a)

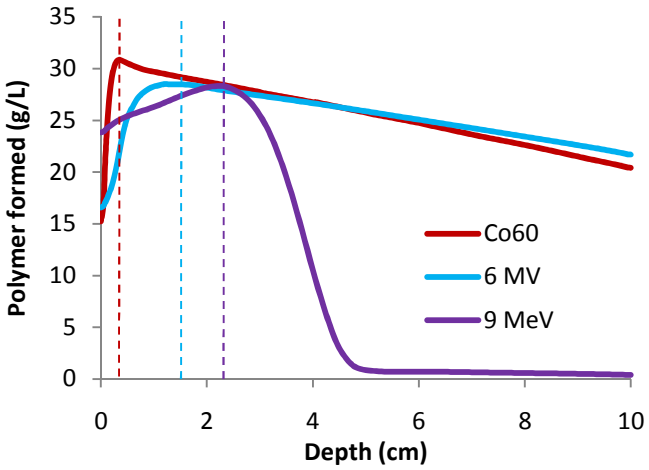

(b)

Figure 2.8: Comparison between (a) the depth-dose curves and (b) the simulated amount of polymer formed 24 hrs post irradiation for Co^{60} γ-radiation, 6 MV x-ray photon beam and 9 MeV electron beam. The position d_{max} is indicated by the vertical dashed lines.

The type of polymer formed can be investigated by simulating the number of crosslinks per mass of polymer formed (see Figure 2.9). The crosslink density of the polymer influences transverse relaxation rates (R_2) when gels are imaged using MR (Babic and Schreiner 2006), and x-ray CT response (in Hounsfield units) when gels are imaged using x-ray CT (Hill *et al.* 2005). For the simulations involving Co^{60} γ-radiation and MV x-ray photons, the predicted change in crosslink density with depth is sufficiently small as to have little effect on imaging readout. However, for MeV electron beams, it is clear that more highly crosslinked (and thus more dense) polymer is formed at low depths where more radiation is received, which may affect imaging response.

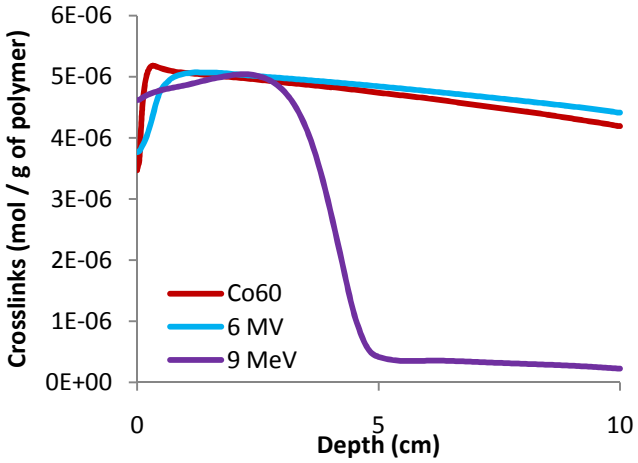

Figure 2.9: The simulated amount of crosslinks per mass of polymer formed 24 hrs post irradiation for Co^{60} γ-radiation, 6 MV x-ray photon and 9 MeV electron beams.

2.6.2 Diffusion effects

Selected simulation results comparing the model predictions with and without diffusion effects are presented in Figure 2.10. Table 2.4 shows the percent difference in the mass of polymer formed at d_{max}, with and without monomer diffusion. Note that, when diffusion is included in the

model, d_{max} is near to, but does not correspond perfectly to the location of maximum polymer formation (see Figure 2.8). For Co^{60} γ-radiation, 6 MV and 15 MV x-ray photon beams, the largest amount of polymer is formed to the left of d_{max}, where the dose gradient is highest, while for all MeV electron beams, the peak is shifted to the right.

Diffusion effects are more prominent near the depth of maximum dose, where monomer concentrations are lower, than at greater depths where monomer concentrations are more uniform. Radiation beams with the largest dose gradients (Co^{60} γ-radiation and 6 MeV electrons) are most affected by monomer diffusion, leading to a difference in polymer formation of over 2 % when diffusion effects are removed (see Figure 2.10a and Table 2.4). High MV photon beams and high MeV electron beams have smoother PDD curves. Thus, diffusion effects have only a minor influence on the mass of polymer formed (less than 0.25 % at d_{max}) as shown in Figure 2.10b and Table 2.4. Therefore, when using depth-dose information for calibration, inaccuracies are possible due to discrepancies caused by monomer diffusion. These inaccuracies tend to be highest near d_{max}.

Table 2.4: Polymer formed 24 hours post irradiation at the location of maximum absorbed dose for simulations with and without diffusion and with and without temperature effects.

Radiation type	Polymer formed (g/L)			Percent increase with D	Percent increase with T
	with D and T	without D	without T		
Co^{60} γ-radiation	30.78	30.00	30.43	2.60	1.15
6 MV x-ray photon beam	28.46	28.32	28.11	0.49	1.25
15 MV x-ray photon beam	28.41	28.35	28.05	0.21	1.28
6MeV electron beam	28.76	28.16	28.62	2.13	0.49
9 MeV electron beam	28.29	28.04	28.11	0.89	0.64
12 MeV electron beam	28.37	28.27	28.12	0.35	0.89
16 MeV electron beam	28.33	28.30	27.98	0.11	1.25
20 MeV electron beam	28.34	28.33	27.99	0.04	1.25

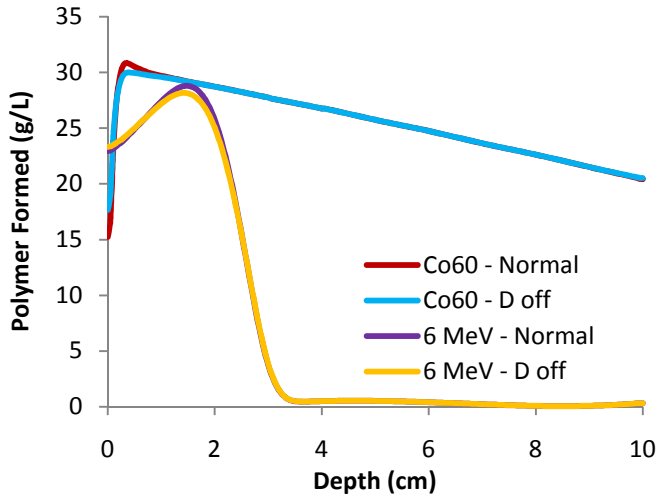

(a)

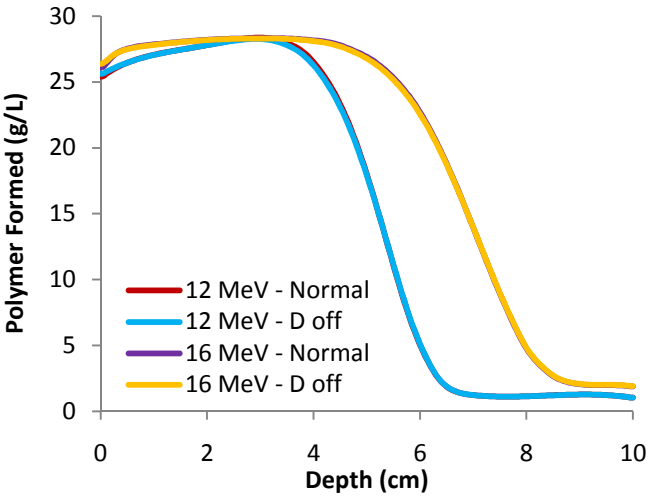

(b)

Figure 2.10: Comparison between normal simulations and simulations without diffusion for: (a) Co^{60} γ-radiation and 6 MeV electron beam, (b) 12 and 16 MeV electron beams, 24 hours post irradiation.

2.6.3 Temperature effects

The temperature of the system increases as polymerization occurs, and then eventually decreases toward room temperature due to heat loss through the front and back walls of the phantom. Regions where higher amounts of radiation are delivered achieve higher temperatures. Since temperature increases the rate of propagation more than the rate of termination, more polymer tends to form in highly irradiated areas, than if the system were isothermal (Salomons *et al.* 2000). Results showing the temperature profiles 24 hours after irradiation, for simulations using the 15 MV x-ray photon beam and the 6 and 9 MeV electron beams, are shown in Figure 2.11. The 15 MV photon beam reached the highest temperature, while the 6 MeV electron beam had the smallest temperature increase. More free radicals were generated by the 15 MV beam due to the higher average dose throughout the phantom (see Figure 2.4).

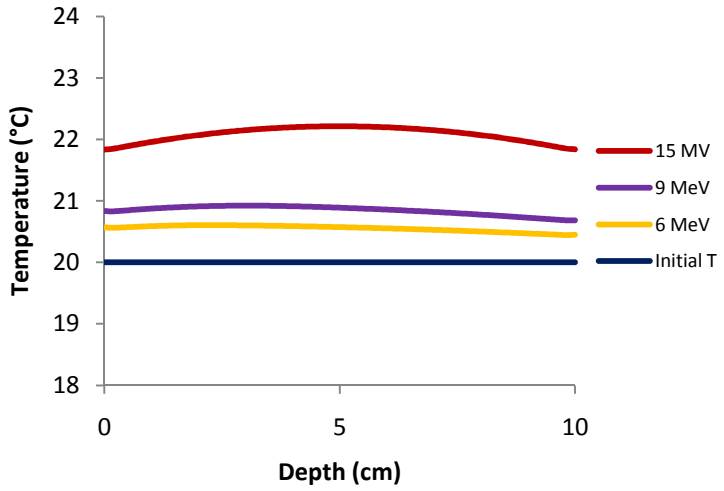

Figure 2.11: Temperature profiles in PAG dosimeters 24 hours post irradiation simulating a 15 MV x-ray photon beam, a 6 MeV electron beam and a 9 MeV electron beam. The initial temperature is shown for reference.

Simulation results comparing the model with and without temperature effects are presented in Figure 2.12 and Table 2.4. As expected, the total mass of polymer formed decreases when the temperature effects are removed from the model. The difference, however, is rather small, with a maximum increase of 1.28 % at d_{max} for the 15 MV x-ray photon beam (see Figure 2.12a), which is a result of having the highest temperature increase (approximately 2 °C) during irradiation and polymerization (see Figure 2.11). Figure 2.12b shows simulation results for radiation beams that are least affected by the removal of temperature dependence, due to lower overall radiation dose. Simulation results show that diffusion effects are more prominent when the depth-dose curve has a large dose gradient, while the influence of temperature is greatest for radiation beams that penetrate far into the phantom, leading to higher overall radiation dose. Overall, these effects are most important when irradiating with Co^{60} γ-radiation. Although monomer diffusion and temperature have only minor effects, they contribute to a loss in calibration accuracy, which influences polymer gel dosimeter effectiveness. In these simulations, radiation was delivered up to 5 Gy at d_{max}. If more radiation were delivered, temperature increases would be greater, and thus temperature effects on mass of polymer formed would be more significant. Similarly, diffusion effects would be more prominent, as larger dose gradients would result in more monomer diffusion. Simulation results show that diffusion and temperature effects are most noticeable at d_{max}. It is therefore recommended that when physicists use depth-dose information to obtain calibration curves, the depth of maximum dose should be avoided, especially for Co^{60} γ-radiation.

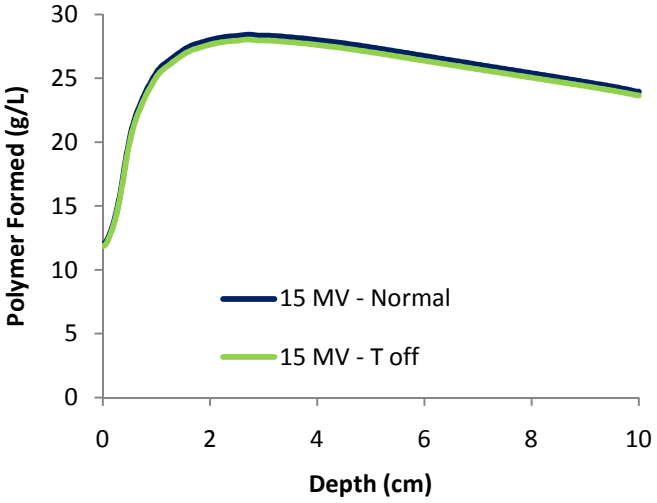

(a)

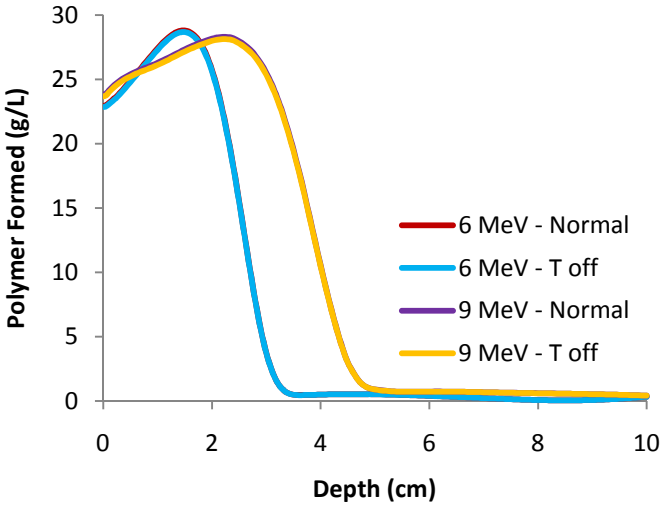

(b)

Figure 2.12: Comparison between simulations with and without temperature effects for (a) the 15 MV radiation beam and for (b) the 6 and 9 MeV electron beams.

2.7 Conclusions

A PAG dosimeter model was extended to simulate the influence of depth-dose behaviour on polymerization and crosslinking in PAG dosimeters when using Co^{60} γ-radiation, 6 and 15 MV x-ray photon beams, and 6 MeV to 20 MeV electron beams. The resulting system of PDEs was solved to predict mass of polymer formed, crosslink density and temperature profiles within PAG phantoms. The influence of monomer diffusion and temperature were investigated by simulations with and without these effects.

The model predicts that both diffusion and temperature effects influence the amount of polymer formed. Diffusion effects are more apparent for Co^{60} γ-radiation and 6 MeV electron beams (2.60% and 2.13% increase in polymer formed at d_{max} respectively) than for other types of radiation. Temperature effects are larger when more radiation is delivered throughout the phantom. With temperature increases on the order of 2 °C, the amount of polymer formed can increase by approximately 1.25%. The 15 MV x-ray photon beam resulted in the highest temperature after irradiation, leading to the largest difference in mass of polymer formed of 1.28%. While these diffusion and temperature effects will have only a small influence for calibration curves obtained using depth-dose experiments, larger discrepancies are anticipated when higher total doses are delivered (e.g. 20 Gy).

Inherent inaccuracies in polymer gel dosimeters due to monomer diffusion, long lived radicals and temperature dependence on reaction rates were observed in simulations of the extended model. As a result, when producing calibration curves using depth-dose information, it is recommended to avoid the depth of maximum dose, particularly for Co^{60} γ-radiation, to obtain more accurate calibration results. Simulated PAG dosimeters did not include THPC in the recipe. For situations involving this oxygen scavenger the effects of diffusion and temperature increases are expected to be smaller due to a reduction in long-lived radicals (De Deene *et al.* 2006).

2.8 Acknowledgments

This work was funded by Mathematics of Information Technology and Complex Systems (MITACS), the Canadian Institutes for Health Research (CIHR) and the Natural Sciences and Engineering Research Council of Canada (NSERC).

2.9 References for Chapter 2

Andrews H L, Murphy R E and LeBrun E J 1957 Gel dosimeter for depth-dose measurements *Rev. Sci. Instrum*. **28** 329–32

Babic S and Schreiner L J 2006 An NMR relaxometry and gravimetric study of gelatine-free aqueous polyacrylamide dosimeters *Phys. Med. Biol.* **51** 4171-87

Baldock C, De Deene Y D, Doran S, Ibbott G, Jirasek A, Lepage M, McAuley K B, Oldham M and Schreiner L J 2010 Polymer gel dosimetry *Phys. Med. Biol.* **55** R1-63

Baldock C, Burford R P, Billingham N, Wagner G S, Patval S, Badawi R D and Keevil S F 1998 Experimental procedure for the manufacture and calibration of polyacrylamide gel (PAG) for magnetic resonance imaging (MRI) radiation dosimetry *Phys. Med. Biol*. **43** 695-702

Baldock C, Burford R P, Billingham N C, Cohen D and Keevil S F 1996 Polymer gel composition in magnetic resonance imaging dosimetry *Med. Phys.* **23** 1070

Baxter P, Jirasek A and Hilts M 2007 X-ray CT dose in normoxic polyacrylamide gel dosimetry *Med. Phys*. **34** 1934–43

Blom J G, Trompert R A and Verwer J G 1996 Algorithm 758: VLUGR2: A Vectorizable Adaptive-Grid Solver for PDEs in 2D *ACM Transactions on Mathematical Software* **22** 302-28

De Deene Y 2006 On the accuracy and precision of gel dosimetry *J. Phys.: Conf. Ser.* **56** 72-85

De Deene Y 2004 Essential characteristics of polymer gel dosimeters *J. Phys.: Conf. Ser.* **3** 34-57

De Deene Y, Vergote K, Claeys C and De Wagter C 2006 The fundamental radiation properties of normoxic polymer gel dosimeters: a comparison between a methacrylic acid based gel and acrylamide based gels *Phys. Med. Biol.* **51** 653-673

De Deene Y, Hurley C, Venning A, Vergote K, Mather M, Healy B J and Baldock C 2002 A basic study of some normoxic polymer gel dosimeters *Phys. Med. Biol.* **47** 3441-63

Dumas E, Leclerc G and Lepage M 2006 Effect of container size on the accuracy of polymer gel dosimetry *J. Phys.: Conf. Ser*. **56** 239–41

Fong P M, Keil D C, Does M D, Gore J C 2001 Polymer gels for magnetic resonance imaging of radiation dose distributions at normal room atmosphere *Phys. Med. Biol.* **46** 3105-13

Fuxman A M, McAuley K B and Schreiner L J 2005 Modelling of polyacrylamide gel dosimeters with spatially non-uniform radiation dose distributions *Chem. Eng. Sci*. **60** 1277-93

Fuxman A M, McAuley K B, and Schreiner L J 2003 Modeling of free-radical crosslinking copolymerization of acrylamide and N,N'-methylenebis(acrylamide) for radiation dosimetry *Macromol. Theory Simul*. **12** 647-62

Fuxman, A. M. 2003 Modelling chemical and physical phenomena in polyacrylamide gel for radiation dosimetry M.Sc. (Eng) Thesis, Department of Chemical Engineering, Queen's University, Kingston, ON, Canada

Gore J C, Kang Y S and Schulz R J 1984 Measurement of radiation dose distributions by nuclear magnetic resonance (NMR) imaging *Phys. Med. Biol*. **29** 1189-97

Guo P, Adamovics J and Oldham M 2006 A practical three-dimensional dosimetry system for radiation therapy *Med. Phys.* **33** 3962-72

Ibbott G S 2004 Applications of gel dosimetry *J. Phys.: Conf. Ser*. **3** 58-77

Ibbott G, Maryanski M J, Eastman P, Holcomb S D, Zhang Y, Avison R G, Sanders M and Gore J C 1997 Three-dimensional visualization and measurement of conformal dose distributions using magnetic resonance imaging of BANG polymer gel dosimeters *Int. J. Radiat. Oncol. Biol. Phys.* **38** 1097-103

Jirasek A, Hilts M and McAuley K B 2010 Polymer gel dosimeters with enhanced sensitivity for use in x-ray CY polymer gel dosimetry *Phys. Med. Biol.* **55** 5269-81

Hepworth S J, Leach M O and Doran S J 1999 Dynamics of polymerization in polyacrylamide gel (PAG) dosimeters: (II) modelling oxygen diffusion *Phys. Med. Biol*. **44** 1875-84

Hilts M 2006 X-ray computed tomography imaging of polymer gel dosimeters *J. Phys.: Conf. Ser*. **56** 95–107

Hilts M and Jirasek A 2008 Adaptive mean filtering for noise reduction in CT polymer gel dosimetry *Med. Phys.* **35** 344-55

Hilts M, Audet C, Duzenli C and Jirasek A 2000 Polymer gel dosimetry using x-ray computed tomography: a feasibility study *Phys. Med. Biol.* **45** 2559-71

Khan F M 2009 *The physics of radiation therapy, 4th ed* (Philadelphia, PA: Lippincott Williams & Wilkins)

Koeva V I, Olding T, Jirasek A, Schreiner L J and McAuley K B 2009a Preliminary investigation of the NMR, optical and x-ray CT dose-response of polymer gel dosimeters incorporating cosolvents to improve dose sensitivity *Phys. Med. Biol.* **54** 2779-90

Koeva V I, Daneshvar S, Senden R J, Imam A H M, Schreiner L J and McAuley K B 2009b Mathematical modeling of PAG- and NIPAM-based polymer gel dosimeters contaminated by oxygen and inhibitor *Macromol. Theory Simul*. **18** 495-510

Lepage M, Whittaker A K, Rintoul L, Back S A J and Baldock C 2001a Modelling of post-irradiation events in polymer gel dosimeters *Phys. Med. Biol.* **46** 2827-39

Lepage M, Whittaker A K, Rintoul L, Back S A J and Baldock C 2001b The relationship between radiation-induced chemical processes and transverse relaxation times in polymer gel dosimeters *Phys. Med. Biol.* **46** 1061-74

Maryanski M J, Ibbott G S, Eastman P, Schulz R J and Gore J C 1996a Radiation therapy dosimetry using magnetic resonance imaging of polymer gels *Med. Phys.* **23** 699-705

Maryanski M J, Zastavker Y Z and Gore J C 1996b Radiation dose distributions in three dimensions from tomographic optical density scanning of polymer gels: II. Optical properties of the BANG polymer gel *Phys. Med Biol.* **41** 2705-17

Maryanski M J, Schulz R J, Ibbott G S, Gatenby J C, Xie J, Horton D and Gore J C 1994 Magnetic resonance imaging of radiation dose distributions using a polymer-gel dosimeter *Phys. Med. Biol.* **39** 1437-55

Maryanski M J, Gore J C, Kennan R P and Schulz R J 1993 NMR relaxation enhancement in gels polymerized and cross-linked by ionizing radiation: a new approach to 3D dosimetry by MRI *Magn. Reson. Imaging*. **11** 253-8

McJury M, Oldham M, Cosgrove V P, Murphy P S, Doran S, Leach M O and Webb S 2000 Radiation dosimetry using polymer gels: methods and applications *Br. J. Radiol* **73** 919-29

McJury M, Oldham M, Leach M O and Webb S 1999 Dynamics of polymerization in polyacrylamide gel (PAG) dosimeters: (I) ageing and long-term stability *Phys. Med. Biol*. **44** 1863-73

Odian G 1991 *Principles of Polymerization, 3rd ed* (New York: John Wiley & Sons)

Oldham M, Sakhalkar H, Guo P and Adamovics J 2008 An investigation of the accuracy of an IMRT dose distribution using two- and three-dimensional dosimetry techniques *Med. Phys.* **35** 2072-80

Oldham M, McJury M, Baustert I B, Webb S and Leach M O 1998 Improving calibration accuracy in gel dosimeter *Phys. Med. Biol*. **43** 2709-20

Olding T, Holmes O and Schreiner L J 2009 Scatter corrections for cone beam optical CT *J. Phys.: Conf. Ser*. **164** 012031

Papagiannis P, Pantelis E, Georgiou E, Karaiskos P, Angelopoulos A, Sakelliou L, Stiliaris S, Baltas D and Seimenis I 2006 Polymer gel dosimetry for the TG-43 dosimetric characterization of a new ^{125}I Insterstitial brachytherapy seed Phys. Med. Biol. **51** 2101-2111

Riggs J B 1988 *An Introduction to Numerical Methods for Chemical Engineers* (Lubbock, TX: Texas Tech University Press) pp 114-22

Rudin A 1982 *The Elements of Polymer Science and Engineering* (New York: Academic Press)

Sakhalkar H S, Adamovics J, Ibbott G and Oldham M 2009 A comprehensive evaluation of the PRESAGE/optical-CT 3D dosimetry system *Med. Phys.* **36** 71-82

Salomons G J, Park Y S, McAuley K B and Schreiner L J 2002 Temperature increases associated with polymerization of irradiated PAG dosimeters *Phys. Med. Biol*. **47** 1435-48

Senden R J, De Jean P, McAuley K B and Schreiner L J 2006 Polymer gel dosimeters with reduced toxicity: a preliminary investigation of the NMR and optical dose-response using different monomers *Phys. Med. Biol.* **51** 3301-14

Trapp J V, Michael G, De Deene Y and Baldock C 2002 Attenuation of diagnostic energy photons by polymer gel dosimeters *Phys. Med. Biol.* **48** 2895-906

Trapp J V, Back S A J, Lepage M, Michael G and Baldock C 2001 An experimental study of the dose response of polymer gel dosimeters imaged with x-ray computed tomography *Phys. Med. Biol.* **46** 2939-51

Venning A J, Hill B, Brindha S, Healy B J and Baldock C 2005 Investigation of the PAGAT polymer gel dosimeter using magnetic resonance imaging *Phys. Med. Biol.* **50** 3875-88

Vergote K, De Deene Y, Vanden Bussche E and De Wagter C 2004 On the relation between the spatial dose integrity and the temporal instability of polymer gel dosimeters *Phys. Med. Biol*. **49** 4507-22

Wai P, Adamovics J, Krstajic N, Ismail A, Nisbet A and Doran S 2009 Dosimetry of the microSelectron-HDR Ir-192 source using PRESAGE ™ and optical CT *Appl. Radiat. Isot.* **67** 419-22

Woods R and Pikaev A 1993 *Applied Radiation Chemistry* (New York: Wiley)

Zang-Salomons J and Mackillop W J 2008 Estimating the lifetime utilization rate of radiotherapy in cancer patients: The Multicohort Current Utilization Table (MCUT) method *Comput. Methods Prog. Biomed.* **92** 99-108

Chapter 3

Improved polymer gel dosimeters for x-ray CT

3.1 Chapter Overview

In this chapter, a new polymer gel dosimeter recipe is developed for use with x-ray CT imaging. NIPAM is investigated as a potential cosolvent to increase the solubility of Bis in the manufacture of polymer gel dosimeters. The work presented in this chapter includes a series of experiments conducted to determine the dose sensitivity and dose resolution of new dosimeters using x-ray CT readouts.

This chapter has been submitted to *Physics in Medicine and Biology*, and appears in manuscript form.

Polymer gel dosimeters with improved dose sensitivity and resolution for readout by x-ray CT

J N M Chain[1], A Jirasek[2], L J Schreiner[3,4], K B McAuley[1]

[1] Dept. of Chemical Engineering, Queen's University, Kingston, Canada, K7L 3N6

[2] Dept. of Physics and Astronomy, University of Victoria, Victoria, Canada, V8W 3P6

[3] Cancer Centre of Southeastern Ontario, Kingston, Canada, K7L 5P9

[4] Depts. of Oncology and Physics, Queen's University, Kingston, Canada, K7L 3N6

3.2 Summary

This study reports new *N*-isopropylacrylamide (NIPAM) polymer gel recipes with increased dose sensitivity and improved dose resolution for x-ray CT readout. NIPAM can be used to increase the solubility of *N, N*'-methylene-bis-acrylamide (Bis) in aqueous solutions from approximately 3 % to 5.5 % by weight, enabling the manufacture of dosimeters containing up to 19.5 %T, which is the total concentration of NIPAM and Bis by weight. Gelatin is shown to have a mild influence on dose sensitivity when gels are imaged using x-ray CT, and a stronger influence when gels are imaged optically. Phantoms that contain only 3 % gelatin and 5 mM tetrakis hydroxymethyl phosphonium chloride (THPC) are sufficiently stiff for dosimetry applications. The new easier-to-produce gel formulations have dose sensitivities that are comparable to the best NIPAM-based gels that incorporate isopropanol as a cosolvent, and have enhanced dose resolution for x-ray CT readout, making clinical applications of this imaging modality more feasible.

3.3 Introduction

Polymer gel dosimeters have been developed as a means of detecting and verifying radiation dose distributions of three-dimensional (3D) radiotherapy treatments (Baldock *et al.* 2010). Recently, much research has gone into improving the dose response of polymer gel dosimeters. These efforts include optimizing the recipe to have increased dose sensitivity (Jirasek *et al.* 2010, Koeva *et al.* 2009, Venning *et al.* 2005) and reduced toxicity (Senden *et al.* 2006, Pappas *et al.* 2001).

The traditional imaging technique for polymer gel dosimeters has been by magnetic resonance imaging (MRI) (Ibbott *et al.* 1997, Bladock *et al.* 1996, Maryanski *et al.* 1993, 1996a). However, due to technical requirements for accurate MRI dosimetry, as well as limited MRI access in clinics (De Deene 2004, Gore *et al.* 1984), recent work has explored the promise of both optical computed tomography (CT) (Wai *et al.* 2009, Sakhalkar *et al.* 2009, Oldham *et al.* 2008, Guo *et al.* 2006) and x-ray CT (Hilts and Jirasek 2008, Baxter *et al.* 2007, Hilts 2006, Trapp *et al.* 2001, 2002) as alternative imaging modalities. While promising, optical CT for polymer gels has several technical concerns preventing its widespread use (Olding *et al.* 2010a, Oldham and Kim 2004, Oldham *et al.* 2003, Maryanski *et al.* 1996b, Gore *et al.* 1996). X-ray CT on the other hand has not gained widespread acceptance due to the low contrast of the resultant images, resulting in poor dose resolution (Hill *et al.* 2005, Hilts *et al.* 2000). Contrast arises from small density changes that occur due to polymerization and crosslinking in irradiated gel dosimeters (Baldock *et al.* 2010, Trapp *et al.* 2001, 2002, Hilts *et al.* 2000). Dosimeters that undergo larger density changes in response to ionizing radiation could result in better contrast and more accurate dosimetry (Hilts *et al.* 2000). Fortunately, x-ray CT is readily available in radiotherapy clinics, is robust and well developed, and is easy to use. Therefore, this paper investigates ways to improve the dose sensitivity and resolution of gel dosimeters for x-ray CT imaging. Normoxic gels that use NIPAM as the monomer and Bis as the crosslinker are explored due to their reduced toxicity

compared with normoxic polyacrylamide gels (nPAG) and their ease of preparation (Senden *et al.* 2006, De Deene *et al.* 2006).

A relationship between gelatin concentration in the phantom and dose sensitivity has been observed with MR scanning (De Deene *et al.* 2006, Gustavsson *et al.* 2004). For example, decreasing the gelatin level from 6 wt% to 3 wt% in a PAG dosimeter increased dose sensitivity (based on the transverse relaxation rate R_2) by approximately 25 % (De Deene *et al.* 2006). This gelatin concentration cannot be reduced too greatly as sufficient gelatin is required in the dosimeter phantom to preserve spatial information about the 3D radiation dose distribution. The addition of THPC, an oxygen scavenger in normoxic polymer gels, results in crosslinking reactions with gelatin that stiffen the gel solution (Jirasek *et al.* 2006). Therefore, due to the presence of THPC, it may be possible to maintain spatial information in gel phantoms using reduced gelatin levels, which could increase the dose sensitivity measured by x-ray CT. Recently, Olding *et al.* (2010b) observed that the amount and type of gelatin used influences light scattering artefacts when gels are imaged by optical CT. As a result, reduction in the amount of gelatin used in gel recipes for optical CT readout may also be beneficial, assuming that sufficient gel stiffness can be maintained at lower gelatin concentrations.

The sensitivity of polymer gel dosimeters to radiation is directly related to %T, the total weight percent of monomer and crosslinker in the system (De Deene *et al.* 2006, Hilts *et al.* 2004), and to %C, the weight of crosslinker relative to total monomer (Maryanski *et al.* 1997). Increases in %T and crosslinker concentration both tend to produce higher dose sensitivities, as measured by MR and x-ray CT (Koeva *et al.* 2009, Babic and Schreiner 2006, Hilts *et al.* 2004, Maryanski *et al.* 1997). Unfortunately, the limited solubility of Bis crosslinker has hampered the development of dosimeters with sufficiently high dose sensitivities for accurate x-ray CT readout. The solubility of Bis in water, which makes up the majority of the mass of polymer gel recipes, is only ~3 % by

weight. Efforts to find effective crosslinkers with increased solubility have been unsuccessful (Koeva *et al.* 2008). Recently, the solubility of Bis in dosimeter solutions was improved using cosolvents (e.g. glycerol and isopropanol) (Koeva *et al.* 2009). X-ray CT results, with improved dose sensitivity and dose resolution were obtained using glycerol and isopropanol to replace a portion of the water in polymer gel formulations (Jirasek *et al.* 2009, 2010, Koeva *et al.* 2009).

Many different chemical species can act as a cosolvent to improve the solubility of organic molecules in aqueous solutions (Cowie and McEwen 1974). In general, a chemical species can act as a cosolvent if it has a chemical structure that is intermediate in polarity between water and the solute of interest. Since NIPAM, which is already present in the dosimeter recipe, is more polar than Bis, but less polar than water, we hypothesize that dosimeter phantoms with increased NIPAM concentrations will be able to dissolve more Bis, making it possible to produce polymer gel phantoms with increased Bis concentrations and increased %T.

The first aim of this study is to determine the solubility limits of NIPAM in water, and of Bis in NIPAM solutions of increasing concentrations to assess whether NIPAM is an effective cosolvent for Bis in polymer gel solutions. The second aim is to determine whether NIPAM polymer gel recipes with reduced levels of gelatin are sufficiently stiff to maintain spatial information and will lead to improved dose sensitivity using x-ray CT readout. The overall objective is to develop and test new polymer gel formulations which maximize the dose response for x-ray CT imaging. This study explores a range of NIPAM gel formulations with high %T and compares the resulting dose sensitivities and dose resolutions to previous gels produced using isopropanol as a cosolvent (Jirasek *et al.* 2010).

3.4 Materials and methods

3.4.1 Solubility experiments

The solubility of NIPAM (manufacturer – TCI Chemicals, OR, USA) in water was determined using 40 g of de-ionized water at 34 °C, to which solid NIPAM was added. Visual observation was used to determine whether or not all of the NIPAM could be dissolved. To determine the solubility of Bis (manufacturer – Sigma-Aldrich) in various NIPAM solutions, a series of aqueous NIPAM solutions was prepared at 34 °C. Bis was then added to 50 g of each NIPAM solution, and the approximate solubility limit for Bis was determined visually.

3.4.2 Gel preparation and analysis

Polymer gels were manufactured in vials for readout by x-ray and by optical methods. For the x-ray studies, 250 g of polymer gel was manufactured in a fume hood and poured into 20 mL scintillation vials (Wheaton Scientific, Millville NJ, USA). For the optical studies, only 100 g of polymer gel was manufactured because the spectrophotometer used smaller cuvettes (4.5 mL polystyrene cuvettes from Fisher Scientific, Canada). The gels contained (by weight) 1.5 % to 5 % gelatin (Type A, 300 Bloom, Sigma-Aldrich, Oakville, Ontario, Canada) and 5 mM THPC (added as an 80 wt% solution in water from Sigma-Aldrich) as an oxygen scavenger. THPC concentrations of 5 mM were used in all dosimeters to ensure sufficient THPC for oxygen scavenging, while maintaining high dose sensitivity (Jirasek *et al.* 2006, Venning *et al.* 2005). The total amount of monomer (NIPAM) and crosslinker (Bis) was varied as needed (6-19.5 %T) while maintaining a Bis concentration near its solubility limit in each gel.

To begin the manufacture of the gels, gelatin was added to the water. The gelatin solution was then heated in a water bath, held at 40 °C until the gelatin was fully dissolved. The gelatin solution was then cooled to 34 °C before adding the desired amount of NIPAM. Once the NIPAM had dissolved, the Bis crosslinker was added at 34 °C. After the Bis had fully dissolved,

the resulting solution was cooled to 30 °C. The THPC solution was added and stirred into the gel for one minute. The resulting gel was then transferred to vials or cuvettes, which were allowed to cool at room temperature. The gels containing only 1.5 % gelatin were refrigerated for several hours since they were slow to set at room temperature. Blank gels, containing only gelatin and water, were also prepared for background subtraction when processing x-ray CT images. These gels were prepared by dissolving the gelatin at 40 °C and were cooled at room temperature. A more detailed experimental procedure is provided in Appendix H.

3.4.3 Gel irradiation

For dose-response studies, gels were irradiated at 1.5 cm depth in water, with a Varian Clinac linear accelerator (Varian Inc., Palo Alto, CA, USA) using 6 MV x-rays, a 10×10 cm^2 field size, and a dose rate of 400 cGy/min. The irradiation was performed approximately four hours after gel preparation. Gels were irradiated at five different depths along the central axis of the beam, in a customized phantom, to doses between 2 and 50 Gy. Doses across each vial were obtained using an Eclipse treatment planning system (Varian Inc, Palo Alto, CA) with appropriate homogeneity corrections used to account for the gel housing vessels. Each vial was rotated 180° half-way through the irradiation, ensuring that a uniform dose had been delivered along the diameter of the vial (Jirasek *et al.* 2009).

The phantoms for the optical tests were irradiated up to 10 Gy, at room temperature, using a T780 Cobalt-60 unit tomotherapy benchtop (MDS Nordion, Kanata, Canada), 24 h after gel manufacture, using a 10×10 cm^2 field and a dose rate of 157 cGy/min, directed perpendicular to their length. These vials were also rotated 180° half-way through the irradiation process.

3.4.4 Gel imaging

CT imaging was performed using a GE HiSpeed X/i scanner (GE Medical Systems, Milwaukee

WI,USA) operating at 140 kVp and 200 mAs. Gel vials were placed in a customized holder (Hilts *et al.* 2004). Sixteen image averages were used for signal-to-noise enhancement and a blank (unirradiated gel) image for background subtraction was utilized to produce each final image.

Gels for optical measurements were inserted in an Ultrospec 1000 UV/Visible Spectrophotometer (Biochrom Ltd, Cambridge, UK) operating at 633 nm, to quantify the fraction of light that passed through the samples. A 0 Gy vial was inserted in the spectrophotometer prior to every light absorption measurement.

3.4.5 Data processing

X-ray dose-response curves were calculated by taking the difference between the mean x-ray CT readout number (N_{CT}) (and standard deviation based on the scatter from sixteen scanned images) of a region of interest within each vial, and the readout number from the 0 Gy vial (ΔN_{CT}). In addition to image averaging and background subtraction, all images were filtered with a Weiner filter using a kernel size of 5×5 and 2 iterations. It has been shown that this combination produces a moderate amount of noise reduction while preserving image fidelity (Hilts and Jirasek, 2008). All data processing was performed using Matlab™ (The Mathworks, Natick, MA, USA).

Dose resolution was calculated based on a 1σ confidence level. The dose resolution is therefore the anticipated error of a data point, divided by the dose sensitivity (slope) at that data point (Gustavsson *et al.* 2004). The slopes of the dose-response curves were calculated by fitting the dose response data to a single exponential function and evaluating the slope of the fitted function at the point of interest, hence eliminating point-by-point noise-induced variations. Note that the dose resolution is an important parameter in gel dosimetry as it provides an estimate of the minimum detectable difference in dose (Gustavsson *et al.* 2004).

3.5 Results and discussion

3.5.1 Effects of gelatin concentration

A series of experiments involving radiation and polymerization was performed using 6 %T gels containing equal masses of NIPAM and Bis (i.e. 50 %C gels) to determine whether gels with lower levels of gelatin and 5 mM THPC are sufficiently stiff to retain 3D information while providing enhanced dose sensitivity. The standard deviation was larger for the 1.5 % gelatin solution, which may be due to the lack of stiffness at room temperature. However, when using 3 % or 5 % gelatin, the gels stiffened and were able to maintain the 3D integrity. X-ray CT imaging of gels prepared with different gelatin concentrations (see Figure 3.1(a)) showed little influence of gelatin concentration on dose sensitivity. The differences in slopes arising from the different gel concentrations are small when analyzed by x-ray CT, with the highest dose sensitivity obtained for the dosimeter with 3 % gelatin. However, reduced gelatin levels produced significant differences in dose sensitivity when phantoms were imaged optically, as shown in Figure 3.1(b). As expected, lower gelatin levels lead to higher optical dose sensitivity. Therefore, when using optical imaging, lowering the gelatin concentration is recommended (along with reduced %T) to produce gels with adequate sensitivity and less light scattering. Note that the lack of dose response at low doses for Figure 3.1(b) is assumed to be due to oxygen inhibition. Table 3.1 provides the dose sensitivities of the three gel dosimeters of varying gelatin concentrations using both optical and x-ray CT imaging. Based on the results in Figure 3.1(a), the amount of gelatin in the recipes used for subsequent experiments (involving different NIPAM and Bis concentrations) was set at 3 % gelatin by weight. No further optical experiments were performed. Recently Khoei *et al.* (2010) recommended using 7-8 mM THPC to produce less variability in dose sensitivity when there are small changes in THPC and oxygen levels (Khoei *et al.* 2010). With higher THPC concentrations, the resulting gels will be even stiffer, supporting

the need for no more than 3 wt% gelatin to hold 3D integrity.

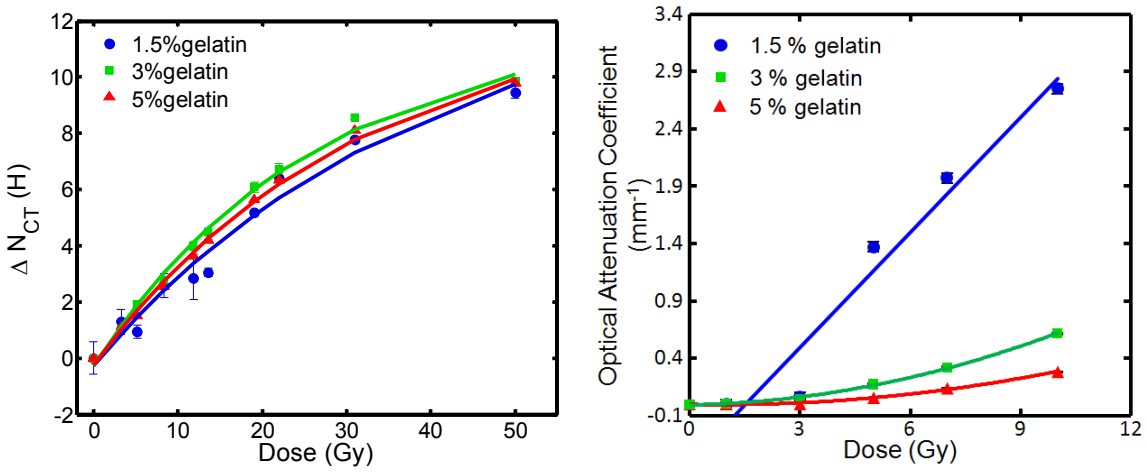

Figure 3.1: Effect of gelatin concentration on dose response for 6 %T, 50 %C gels imaged using (a) x-ray CT and (b) optical measurements. Note that many error bars are hidden behind the symbols for the experimental points. Curves are added to (b) to guide the eye.

Table 3.1: Dose sensitivities (slopes) for 6 %T, 50 %C gels of different gelatin concentrations using x-ray CT and optical imaging.

Recipe	**Dose Sensitivity**	
	X-ray CT (H/Gy)	**Optical (mm^{-1}/Gy)**
1.5 % gelatin	0.26 ± 0.016	0.3347 ± 0.044
3 % gelatin	0.32 ± 0.008	0.0693 ± 0.009
5 % gelatin	0.30 ± 0.005	0.0409 ± 0.003

3.5.2 Solubility of Bis in aqueous NIPAM solutions

The maximum solubility of NIPAM in water was determined to be ~17.8 % by weight at 34 °C, which is the manufacturing temperature. Lower solubility is achieved at lower temperatures. The solubility for Bis in several solutions containing NIPAM and water is shown in Figure 3.2. The results in Figure 3.2 indicate that NIPAM acts as a cosolvent for Bis. Increasing the concentration of NIPAM in the solution results in greater Bis solubility. The maximum solubility of Bis (at 34 °C) using NIPAM as a cosolvent is approximately 5.5 % by weight, which is a substantial increase over the 3 % by weight solubility for Bis in water without any NIPAM.

The resulting solubility curve was used to select the monomer concentrations in subsequent radiation experiments. In these experiments, the standard gel manufacturing procedure (Koeva *et al.* 2009, Senden *et al.* 2006, De Deene *et al.* 2002, Baldock *et al.* 1998) was altered, in that NIPAM was added prior to Bis, to enable easier and faster Bis dissolution.

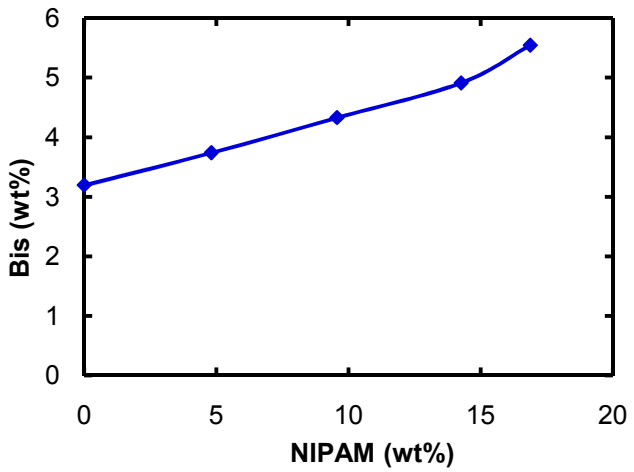

Figure 3.2: Solubility of Bis in aqueous NIPAM solutions at 34 °C.

3.5.3 Recipes with increasing monomer concentrations

Using the results from Figure 3.1(a) and Figure 3.2, gels were prepared using 3 % gelatin with increased %T and with the concentration of Bis just below its corresponding solubility limit to enable complete Bis dissolution. As expected, when the concentration of monomers increases, dose sensitivity and dose resolution improve. Figure 3.3(a) shows that dose sensitivity was highest for the gel with highest %T (containing 15 % NIPAM and 4.5 % Bis by weight). This gel, also had the best dose resolution (~0.1 Gy), as shown in Figure 3.3(b). Note that there was a substantial improvement in both sensitivity and resolution compared with a more traditional gel recipe (6 %T, 50 %C), which is often used for MR imaging (Babic and Schreiner 2006, De Deene *et al.* 2006, Senden *et al.* 2006).

The dose sensitivity of NIPAM-based polymer gels was previously improved through the use of glycerol and isopropanol as cosolvents. Koeva *et al.* (2008) and Jirasek *et al.* (2010) showed that isopropanol improves the solubility of Bis. This increased solubility enables the manufacture of gel phantoms with high Bis levels, resulting in improvements in dose sensitivity and resolution (Koeva *et al.* 2009, Jirasek *et al.* 2009, 2010). Jirasek *et al.* (2010) determined that the best gel to date, containing 30 % isopropanol, 8 % NIPAM and 8 % Bis, exhibits enhanced dose sensitivity and resolution, making this gel promising for x-ray CT readout. In Figure 3.4, the sensitivity and resolution of this isopropanol gel are compared with those of the highest %T gel (15 % NIPAM and 4.5 % Bis) from the current study. The new high %T gel without cosolvent has similar dose sensitivity to the previous gel with isopropanol, but has significantly better resolution, especially at high doses. Note that the isopropanol-free gel is easier to manufacture because of the reduced number of components. It will be important to study the water and tissue equivalence of both of these gels, because the overall water concentrations are lower than in traditional 6 %T gels.

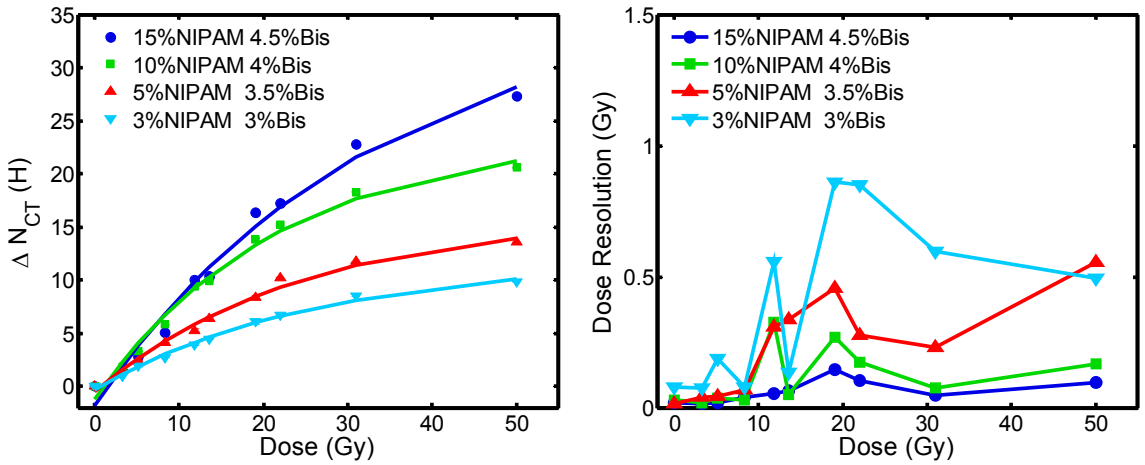

Figure 3.3: (a) Dose response and (b) dose resolution for gels of increasing NIPAM and Bis concentrations with 3 % gelatin, determined by x-ray CT. Lines are added to (b) to guide the eye.

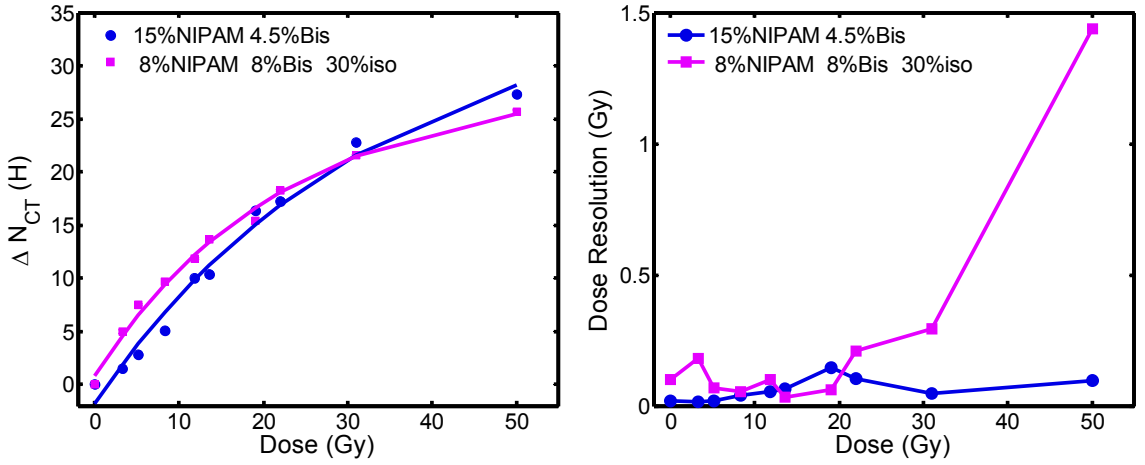

Figure 3.4: (a) Dose response and (b) dose resolution for the highest %T (15 % NIPAM and 4.5 % Bis) gel from the current study and for the 8 % NIPAM, 8 % Bis and 30 % isopropanol gel from Jirasek *et al.* (2010). Lines are added to (b) to guide the eye.

3.6 Conclusions and recommendations

It is shown that NIPAM improves the solubility of Bis in polymer gel dosimeters from approximately 3 % by weight in water to approximately 5.5 % by weight in aqueous solutions containing NIPAM at its solubility limit of 16.8 wt%. Polymer gels with a reduced level of gelatin (3 % by weight) may show a mild benefit in dose sensitivity when imaged by x-ray CT. However, a substantial increase in the dose sensitivity is observed with optical imaging. Having 3 wt% gelatin with 5 mM THPC in the dosimeter recipe is enough to maintain adequate gel stiffness.

This study shows that high %T gel dosimeters can be made without using any additional cosolvent, such as isopropanol or glycerol. The new high %T gels exhibit enhanced dose sensitivity and dose resolution, when compared with previous gels. The best dosimeter from our study, which contained ~15 % NIPAM and ~4.5 % Bis, exhibits comparable dose sensitivity and better dose resolution than the recent best gel by Jirasek *et al.* (2010), which used isopropanol as a cosolvent. Use of the proposed gel recipe with x-ray CT readout holds great promise for future implementation in the clinic.

3.7 Acknowledgments

We would like to thank Dr. Tim Olding for his help with the T780 Cobalt-60 irradiations. This work was funded by the Canadian Institutes for Health Research (CIHR) and the Natural Sciences and Engineering Research Council of Canada (NSERC).

3.8 References for Chapter 3

Babic S and Schreiner L J 2006 An NMR relaxometry and gravimetric study of gelatin-free aqueous polyacrylamide dosimeters *Phys. Med. Biol.* **51** 4171-4187

Baldock C, Burford R P, Billingham N C, Cohen D and Keevil S F 1996 Polymer gel composition in magnetic resonance imaging dosimetry *Med. Phys.* **23** 1070

Baldock C, De Deene Y D, Doran S, Ibbott G, Jirasek A, Lepage M, McAuley K B, Oldham M and Schreiner L J 2010 Polymer gel dosimetry *Phys. Med. Biol.* **55** R1-63

Baxter P, Jirasek A and Hilts M 2007 X-ray CT dose in normoxic polyacrylamide gel dosimetry *Med. Phys*. **34** 1934–43

Cowie J M G and McEwen I J 1974 Polymer-cosolvent systems. IV. Upper and lower critical solution temperatures in the system methylcyclohexane-diethyl ether-polystyrene *Macromolecules* **7** (3) 291-6

De Deene Y, Hurley C, Venning A, Vergote K, Mather M, Healy B J and Baldock C 2002 A basic study of some normoxic polymer gel dosimeters *Phys. Med. Biol.* **47** 3441-63

De Deene Y 2004 Fundamentals of MRI measurements for gel dosimetry *J. Phys.: Conf. Ser.* **3** 87-114

De Deene Y, Vergote K, Claeys C and De Wagter C 2006 The fundamental radiation properties of normoxic polymer gel dosimeters: a comparison between a methacrylic acid based gel and acrylamide based gels *Phys. Med. Biol.* **51** 653-73

Gore J C, Kang Y S and Schulz R J 1984 Measurement of radiation dose distributions by nuclear magnetic resonance (NMR) imaging *Phys. Med. Biol.* **29** 1189-97

Gore J C, Ranade M, Maryanski M J and Schulz R J 1996 Radiation dose distributions in three dimensions from tomographic optical density scanning of polymer gels: I. Development of an optical scanner *Phys. Med. Biol.* **41** 2695-704

Guo P, Adamovics J and Oldham M 2006 A practical three-dimensional dosimetry system for radiation therapy *Med. Phys.* **33** 3962-72

Gustavsson H, Back S A J, Lepage M, Rintoul L and Baldock C 2004 Development and optimization of a 2-hyrdoxyethylacrylate MRI polymer gel dosimeter *Phys. Med. Biol.* **49** 227-41

Hill B, Venning A and Baldock C 2005 The dose response of normoxic polymer gel dosimeters measured using X-ray CT *Br. J. Radiol.* **78** 623-30

Hilts M 2006 X-ray computed tomography imaging of polymer gel dosimeters *J. Phys.: Conf. Ser*. **56** 95–107

Hilts M, Audet C, Duzenli C and Jirasek A 2000 Polymer gel dosimetry using x-ray computed tomography: a feasibility study *Phys. Med. Biol.* **45** 2559-71

Hilts M, Jirasek A and Duzenli C 2004 Effects of gel composition on the radiation induced density change in PAG polymer gel dosimeters: A model and experimental investigations *Phys. Med. Biol.* **49** 2477-90

Hilts M and Jirasek A 2008 Adaptive mean filtering for noise reduction in CT polymer gel dosimetry *Med. Phys.* **35** 344-55

Ibbott G, Maryanski M J, Eastman P, Holcomb S D, Zhang Y, Avison R G, Sanders M and Gore J C 1997 Three-dimensional visualization and measurement of conformal dose distributions using magnetic resonance imaging of BANG polymer gel dosimeters *Int. J. Radiat. Oncol. Biol. Phys.* **38** 1097-103

Jirasek A, Hilts M, Shaw C and Baxter P 2006 Investigation of tetrakis hydroxymethyl phosphonium chloride as an antioxidant for use in x-ray computed tomography polyacrylamide gel dosimetry *Phys. Med. Biol.* **51** 1891-906

Jirasek A, Hilts M, Berman A and McAuley K B 2009 Effects of glycerol co-solvent on the rate and form of polymer gel dose response *Phys. Med. Biol.* **54** 907-18

Jirasek A, Hilts M and McAuley K B 2010 Polymer gel dosimeters with enhanced sensitivity for use in x-ray CY polymer gel dosimetry *Phys. Med. Biol.* **55** 5269-81

Khoei S, Moorrees J, Langton C and Trapp J V 2010 An investigation of the pre-irradiation temporal stability of PAGAT gel dosimeters *IC3DDose 2010 Proc. 6th Int. Conf. on 3D Radiation Dosimetry (Hilton Head Island, SC, USA)* ed M Oldham

Koeva V I, Csaszar E S, Senden R J, McAuley K B and Schreiner L J 2008 Polymer gel dosimeters with increased solubility: a preliminary investigation of the NMR and optical dose-response using different crosslinkers and co-solvents *Macromol. Symp.* **261** 157-66

Koeva V I, Olding T, Jirasek A, Schreiner L J and McAuley K B 2009 Preliminary investigation of the NMR, optical and x-ray CT dose-response of polymer gel dosimeters incorporating cosolvents to improve dose sensitivity *Phys. Med. Biol.* **54** 2779-90

Maryanski M J, Gore J C, Kennan R P and Schulz R 1993 NMR relaxation enhancement in gels polymerized and cross-linked by ionizing radiation: a new approach to 3-D dosimetry by MRI *Magn. Reson. Imaging* **11** 253-8

Maryanski M J, Ibbott G S, Eastman P, Schulz R J and Gore J C 1996a Radiation therapy dosimetry using magnetic resonance imaging of polymer gels *Med. Phys.* **23** 699-705

Maryanski M J, Zastavker Y Z and Gore J C 1996b Radiation dose distributions in three dimensions from tomographic optical density scanning of polymer gels: II. Optical properties of the BANG polymer gel *Phys. Med Biol.* **41** 2705-17

Maryanski M J, Audet C and Gore J C 1997 Effects of crosslinking and temperature on the dose response of a BANG polymer gel dosimeter *Phys. Med. Biol.* **42** 303-11

Oldham M, Sakhalkar H, Guo P and Adamovics J 2008 An investigation of the accuracy of an IMRT dose distribution using two- and three-dimensional dosimetry techniques *Med. Phys.* **35** 2072-80

Olding T, Holmes O and Schreiner L J 2010a Cone beam optical computed tomography for gel dosimetry I: scanner characterization *Phys. Med. Biol.* **55** 2819-40

Olding T, Darko J and Schreiner L J 2010b Effective management of FXG gel dosimetry *IC3DDose 2010 Proc. 6th Int. Conf. on 3D Radiation Dosimetry (Hilton Head Island, SC, USA)* ed M Oldham

Pappas E, Seimenis I, Angelopoulos A, Georgolopoulou P, Kamariotaki-Paparigopoulou M, Maris T, Sakelliou L, Sandilos P and Vlachos L 2001 Narrow stereotactic beam profile measurements using N-vinylpyrrolidone based polymer gels and magnetic resonance imaging *Phys. Med. Biol.* **46** 783-97

Sakhalkar H S, Adamovics J, Ibbott G and Oldham M 2009 A comprehensive evaluation of the PRESAGE/optical-CT 3D dosimetry system *Med. Phys.* **36** 71-82

Senden R J, De Jean P, McAuley K B and Schreiner L J 2006 Polymer gel dosimeters with reduced toxicity: a preliminary investigation of the NMR and optical dose-response using different monomers *Phys. Med. Biol.* **51** 3301-14

Trapp J V, Back S A J, Lepage M, Michael G and Baldock C 2001 An experimental study of the dose response of polymer gel dosimeters imaged with x-ray computed tomography *Phys. Med. Biol.* **46** 2939-51

Trapp J V, Michael G, De Deene Y and Baldock C 2002 Attenuation of diagnostic energy photons by polymer gel dosimeters *Phys. Med. Biol.* **48** 2895-906

Venning A J, Hill B, Brindha S, Healy B J and Baldock C 2005 Investigation of the PAGAT polymer gel dosimeter using magnetic resonance imaging *Phys. Med. Biol.* **50** 3875-88

Wai P, Adamovics J, Krstajic N, Ismail A, Nisbet A and Doran S 2009 Dosimetry of the microSelectron-HDR Ir-192 source using PRESAGE ™ and optical CT *Appl. Radiat. Isot.* **67** 419-22

Xu Y, Wuu C S, Maryanski M J 2003 Determining optimal gel sensitivity in optical CT scanning of gel dosimeters *Med. Phys.* **30** 2257-63

Chapter 4

Conclusions and recommendations

4.1 Conclusions

In Chapter 2 of this thesis, the influence of radiation depth-dose behaviour of a number of clinically relevant radiation sources (Co^{60} γ-radiation, 6 and 15 MV x-ray photon beams, and 6 MeV to 20 MeV electron beams) on polyacrylamide gel dosimeters was modelled. The PDD data were converted to a convenient functional form, using cubic splines, for input to the extended model. The reaction scheme was revised to include termination reactions involving gelatin radicals. Further adjustments to the model were performed to better describe the new system. A transformation was required to allow the model to simulate depth-dose information in a phantom of the desired length (10 cm). The influences of monomer diffusion and temperature were investigated by simulations with and without these effects.

From the model predictions, it was determined that monomer diffusion and temperature effects are of particular importance at the depth of maximum dose (d_{max}). The difference in mass of polymer formed between simulations where diffusion effects were included or removed from the model, reached up to 2.60% (for Co^{60} γ-radiation) at d_{max}, and less for all other types of radiation. The diffusion of monomers from low-dose areas to high-dose areas (where monomers were more quickly consumed), provided an increase in polymer formed. More monomer diffusion occurs when dose gradients are large (steep areas of depth-dose curves).

Similarly, when temperature effects were included in the model, more polymer was formed over time, up to 1.28% for the 15 MV x-ray photon beam. The increased polymer formation is due to temperature increases during irradiation and polymerization. Higher temperatures are reached when the radiation penetrates more deeply into the phantom (e.g. MV photon beams), leading to

temperature increases of approximately 2 °C.

The simulation results of the extended model show that when producing calibration curves based on radiation depth-dose information, more accurate results are obtained away from the depth of maximum dose, particularly for Co^{60} γ-radiation.

Chapter 3 describes how the solubility of Bis can be increased substantially by adding larger quantities of NIPAM to the polymer gel dosimeter recipe. Dosimeters manufactured using up to 15 %NIPAM and 4.5 %Bis by weight were shown to produce significantly higher dose sensitivity and improved dose resolution for x-ray CT than a traditional 3 %NIPAM and 3 %Bis dosimeter. This increase in solubility allows for the manufacture of high %T polymer gel dosimeters without using an additional cosolvent such as glycerol or isopropanol in the recipe.

The effects of gelatin concentration on polymer gel dose response were also studied in Chapter 3. Gels manufactured using 3 % by weight of gelatin (rather than the traditional 5 %gelatin) may show a mild benefit in dose response when imaged by x-ray CT. A substantial increase in dose response of a dosimeter using only 3 % by weight of gelatin was observed with optical imaging. The resulting dosimeter with a reduced level of gelatin maintained adequate gel stiffness in the prepared vials.

The new polymer gel formulation of Chapter 3 has a dose resolution of approximately 0.1 Gy, when imaged with x-ray CT and when receiving up to 50 Gy of radiation. This is a significant improvement compared to the previous best dosimeter formulation for x-ray CT, especially high doses. This improvement in dose resolution shows that the use of the proposed high %T polymer gel recipe, with a reduction in gelatin concentration, for x-ray CT imaging holds great promise for future implementation in the clinic.

4.2 Recommendations

The following recommendations are made for future research on the modelling of polymer gel dosimeters:

- The model should be further extended to simulate normoxic polymer gel dosimeters, which include the effects of the oxygen scavenger (THPC). A better understanding of the interactions of THPC with all other polymer gel components (primarily reactions with radicals and gelatin) would be helpful for predicting dosimeter behaviour.
- It would be beneficial to perform experiments using depth-dose information from various radiation sources, as a means of validating the model simulations.
- Simulations with a higher delivered dose (e.g. 20 Gy) should be performed to investigate whether larger monomer diffusion and temperature effects are observed.
- Simulations using the new proposed high %T dosimeter recipe from Chapter 3 should be investigated.
- An extended model should be developed to investigate the influence of monomer diffusion on depth-dose behaviour in 2D. This will allow for radial diffusion, which is a more accurate representation of a delivered pencil beam of radiation.

The following recommendations are made for future research on polymer gel dosimeter recipe improvement:

- Further experiments should be performed to determine the accuracy and reproducibility of the new high %T polymer gel dosimeter recipe using NIPAM as a cosolvent for Bis.
- The spatial resolution of the new polymer gel dosimeter recipe should be investigated using a large (1 L) phantom with non-uniform irradiation (perhaps using overlapping radiation pencil beams). These results will be important to confirm the effectiveness of

the new recipe and to determine whether the reduction of gelatin to 3% is advisable using a larger phantom. The new recipe can then be better compared with the current best dosimeter by Jirasek *et al.* (2010).

Appendix A

List of assumptions

Table A.1 lists the assumptions made in the development of the extended model.

Table A.1: List of assumptions made in the development of the kinetic model.

1)	The reactivity of the growing polymer chains depends only on the terminal molecule bonded to the radical (*terminal model*).
2)	The system is composed of two different types of radicals: those on small molecules (with high mobility in the aqueous and polymer phases) and those on long-crosslinked molecules (immobile in the polymer phase).
3)	Seven-membered ring cyclization is the dominant mode of intramolecular crosslinking.
4)	No degradation of the polymer by radiation occurs.
5)	No oxygen or other impurities that consume radicals are present in the reacting mixture.
6)	The reactivities of double bonds on the acrylamide and bisacrylamide monomers are equal (Tobita and Hamielec 1990). The reactivity of radicals bearing the active center on a bisacrylamide unit is lower (by a factor w) than those on an acrylamide, due to the shielding effect of the long un-reacted pendant vinyl group. It is assumed that the chain transfer rates are proportional to the rates of propagation, i.e., $\left(k_{f12}/k_{f11}\right) = \left(k_{p12}/k_{p11}\right)$. Terminal double bonds formed by chain transfer and termination reactions are assumed to behave like PDBs.
7)	Heat effects associated with precipitation of the polymer are neglected. Heat generated by the absorption of radiation by water is negligible (in water alone 1Gy increases the temperature by 10^{-4} °C).
8)	Volume changes due to changes in density during polymerization are neglected.
9)	Due to the high concentration of water in the system, ionizing radiation interacts with water to produce free radicals that subsequently react with monomers and gelatin (Myers 1973). The direct action of radiation on the monomers and gelatin is neglected. The three main types of primary radicals generated (e_{aq}^{-}, $H^{\cdot}$ and $OH^{\cdot}$) are assumed to have equal reactivities and to react very quickly with dissolved monomer.
10)	The system is composed of two different types of polymeric radicals: small linear molecules that remain soluble in the aqueous phase and larger cross-linked molecules that precipitate from solution (Durmaz and Okay 2000; Lepage et al. 2001d). When a linear polymeric radical in the aqueous phase reacts with a PDB or a terminal double bond on another polymer molecule, the polymer forms a microgel which precipitates. This assumption is a special case of the numerical fractionation technique proposed by Teymour and Campbell (1994), wherein the first generation of cross-linked polymer is enough to form a gel.

11) All linear polymer chains in the aqueous phase (both growing radicals and dead polymer chains) have similar numbers of PDBs and cyclized units. When a growing radical in the aqueous phase precipitates, the PDBs and cyclized units on it are transferred to the polymer phase. All new PDBs that are formed by the growing crosslinked radical are assumed to be in the precipitated polymer phase. Only a fraction of the new PDBs generated in the precipitated polymer phase are available for reaction with radicals in the aqueous phase.

12) Reactions in the aqueous phase are assumed to be chemically controlled and the propagation rate constant does not depend on the relative amounts of water and monomers, as has been shown for some water-soluble vinyl monomers (Gromov et al. 1980). However, due to the high degree of crosslinking within the precipitated polymer phase, all reactions in the polymer phase are modelled as if they were diffusionally controlled.

13) Radicals that have undergone primary cyclization reactions following the addition of bisacrylamide have the same reactivity as radicals with terminal acrylamide units (Fuxman et al. 2003).

14) In the aqueous phase, concentration gradients develop due to diffusion of monomers and radicals. Gelatin is assumed to be immobile. Within each microgel in the polymer phase, the concentration of monomers and polymeric species are assumed to be uniform.

15) Concentration and temperature gradients are only in one dimension. It is assumed that the top and bottom of the reaction vessel are insulated.

16) Gelatin is not consumed. The concentration of gelatin in both phases is assumed to be the same.

A.1 References for Appendix A

Durmaz S and Okay O 2000 Phase separation during the formation of poly(acrylamide) hydrogels. *Polymer* **41** 5729-35

Fuxman A M, McAuley K B and Schreiner L J 2003 Modeling freeradical crosslinking copolymerization of acrylamide and N,N' - methylenbis(acrylamide) for radiation dosimetry *Macromol Theory Simul* **12** 647-62

Gromov V F, Galperina N I, Osmanov T O, Khomikovskii P M and Abkin A D 1980 Effect of solvent on chain propagation and termination reaction rates in radical polymerization *Eur. Polym. J.* **16** 529-35

Lepage M, Whittaker A K, L. R and Baldock C 2001 13C-NMR, 1H-NMR, and FT-Raman study of radiation-induced modifications in radiation dosimetry polymer gels. *Journal of Applied Polymer Science* **79** 1572-81

Myers L S 1973 *The radiation chemistry of macromolecules*, 2nd edition, Dole M, ed., (New York: Academic)

Teymour F and Campbell J D 1994 Analysis of the dynamics of gelation in polymerization reactors using the “numerical fractionation” technique *Macromolecules* **27** 2460-9

Tobita H and Hamielec A E 1990 Crosslinking kinetics in polyacrylamide networks *Polymer* **31** 1546-52

Appendix B

Reaction mechanisms

Table B.1 lists reaction mechanisms occurring after generation of primary radicals by water radiolysis.

Table B.1: Reaction scheme.

Aqueous Phase		**Polymer Phase**	
Initiation		*Initiation*	
$(2\mathrm{PR}^{\cdot w}) \xrightarrow{fast} f.\,2\ \mathrm{PR}^{\cdot w}$	(B.1a)	$(2\mathrm{PR}^{\cdot p}) \xrightarrow{fast} f.\,2\ \mathrm{PR}^{\cdot p}$	(B.1b)
$\mathrm{PR}^{\cdot w} + M_1^w \xrightarrow{k_{ini1}} S_{1,n}^w$	(B.2a)	$\mathrm{PR}^{\cdot p} + M_1^p \xrightarrow{k_{ini1}} S_1^p$	(B.2b)
$\mathrm{PR}^{\cdot w} + M_2^w \xrightarrow{k_{ini2}} S_{2,n}^w$	(B.3a)	$\mathrm{PR}^{\cdot p} + M_2^p \xrightarrow{k_{ini2}} S_2^p$	(B.3b)
Propagation		*Propagation*	
$S_{1,n}^w + M_1^w \xrightarrow{k_{p11}^w} S_{1,n+1}^w$	(B.4a)	$L_1^p + M_1^p \xrightarrow{k_{p11}^p} L_1^p$	(B.4b)
$S_{1,n}^w + M_2^w \xrightarrow{k_{p12}^w} S_{2,n+1}^w$	(B.5a)	$L_1^p + M_2^p \xrightarrow{k_{p12}^p} L_2^p$	(B.5b)
$S_{2,n}^w + M_1^w \xrightarrow{k_{p21}^w} S_{1,n+1}^w + \mathrm{PDB}_e^w$	(B.6a)	$L_2^p + M_1^p \xrightarrow{k_{p21}^p} L_1^p + PDB_e^p$	(B.6b)
$S_{2,n}^w + M_2^w \xrightarrow{k_{p22}^w} S_{2,n+1}^w + \mathrm{PDB}_e^w$	(B.7a)	$L_2^p + M_2^p \xrightarrow{k_{p22}^p} L_2^p + PDB_e^p$	(B.7b)
		$L_3^p + M_1^p \xrightarrow{k_{p21}^p} L_1^p$	(B.8b)
		$L_3^p + M_2^p \xrightarrow{k_{p22}^p} L_2^p$	(B.9b)
Cyclization		*Cyclization*	
$S_{2,n}^w \xrightarrow{k_c^w} S_{1,n}^w + C^w$	(B.10a)	$L_2^p \xrightarrow{k_c^w} L_1^p + C^p$	(B.10b)
Cross-linking		*Cross-linking*	
$S_{1,n}^w + \mathrm{PDB}_e^w \xrightarrow{k_{x1}^w} S_{x,n}^w + X^w$	(B.12a)	$S_1^p + \mathrm{PDB}_e^p \xrightarrow{k_{x1'}^P} L_3^p + X^P$	(B.11b)
$S_{2,n}^w + \mathrm{PDB}_e^w \xrightarrow{k_{x2}^w} S_{x,n}^w + X^w + \mathrm{PDB}_e^w$	(B.11a)	$S_2^p + \mathrm{PDB}_e^p \xrightarrow{k_{x2'}^P} L_3^p + X^P + \mathrm{PDB}_e^P$	(B.12b)
		$L_1^p + \mathrm{PDB}_e^p \xrightarrow{k_{x1}^P} L_3^p + X^P$	(B.13b)
		$L_2^p + \mathrm{PDB}_e^p \xrightarrow{k_{x2}^P} L_3^p + X^P + \mathrm{PDB}_e^P$	(B.14b)

Transfer to monomer

$$S_{1,n}^{w} + M_1^{w} \xrightarrow{k_{f11}^{w}} S_{1,1}^{w} + D_n^{w} + \mathrm{PDB}_e^{w} \quad \text{(B.15a)}$$

$$S_{1,n}^{w} + M_2^{w} \xrightarrow{k_{f12}^{w}} S_{2,1}^{w} + D_n^{w} + \mathrm{PDB}_e^{w} \quad \text{(B.16a)}$$

$$S_{2,n}^{w} + M_1^{w} \xrightarrow{k_{f21}^{w}} S_{1,1}^{w} + D_n^{w} + 2\mathrm{PDB}_e^{w} \quad \text{(B.17a)}$$

$$S_{2,n}^{w} + M_2^{w} \xrightarrow{k_{f22}^{w}} S_{2,1}^{w} + D_n^{w} + 2\mathrm{PDB}_e^{w} \quad \text{(B.18a)}$$

Termination by disproportionation

$$S_{1,n}^{w} + S_{1,r}^{w} \xrightarrow{k_{t11}^{w}} D_n^{w} + D_r^{w} + \mathrm{PDB}_e^{w} \quad \text{(B.19a)}$$

$$S_{1,n}^{w} + S_{2,r}^{w} \xrightarrow{k_{t12}^{w}} D_n^{w} + D_r^{w} + 2\mathrm{PDB}_e^{w} \quad \text{(B.20a)}$$

$$S_{2,n}^{w} + S_{2,r}^{w} \xrightarrow{k_{t22}^{w}} D_n^{w} + D_r^{w} + 3\mathrm{PDB}_e^{w} \quad \text{(B.21a)}$$

Reactions with Gelatin

Termination with gelatin

$$S_{1,n}^{w} + G^{\cdot w} \xrightarrow{k_{t12}^{w}} D_n^{w} \quad \text{(B.22a)}$$

$$S_{2,n}^{w} + G^{\cdot w} \xrightarrow{k_{t22}^{w}} D_n^{w} + \mathrm{PDB}_e^{w} \quad \text{(B.23a)}$$

Transfer to gelatin

$$S_{1,n}^{w} + G^{w} \xrightarrow{k_{fG1}^{w}} D_n^{w} + \theta G^{\cdot w} \quad \text{(B.24a)}$$

$$S_{2,n}^{w} + G^{w} \xrightarrow{k_{fG2}^{w}} D_n^{w} + \theta G^{\cdot w} + \mathrm{PDB}_e^{w} \quad \text{(B.25a)}$$

Re-initiation

$$G^{\cdot w} + M_1^{w} \xrightarrow{k_{pG1}^{w}} S_{1,n}^{w} + G^{w} \quad \text{(B.26a)}$$

$$G^{\cdot w} + M_2^{w} \xrightarrow{k_{pG2}^{w}} S_{2,n}^{w} + G^{w} \quad \text{(B.27a)}$$

Transfer between phases

$$S_{x,n}^{w} \xrightarrow{precip.} L_3^{p} \quad \text{(B.29)}$$

$$\mathrm{PDB}_e^{w}, C^{w}, X^{w} \xrightarrow{precip.} \mathrm{PDB}_e^{P}, C^{P}, X^{P} \quad \text{(B.28)}$$

$$M_1^{w} \overset{\Phi_{M_1}}{\Longleftrightarrow} M_1^{P} \quad \text{(B.30)}$$

$$M_2^{w} \overset{\Phi_{M_2}}{\Longleftrightarrow} M_2^{P} \quad \text{(B.31)}$$

$$\mathrm{H_2O}^{w} \overset{\Phi_{H_2O}}{\Longleftrightarrow} \mathrm{H_2O}^{p} \quad \text{(B.32)}$$

$$G^{w} \overset{\Phi_{G}}{\Leftrightarrow} G^{P} \quad \text{(B.33)}$$

Transfer to monomer

$$L_1^{p} + M_1^{p} \xrightarrow{k_{f11}^{w}} S_1^{p} + D^{p} + \mathrm{PDB}_e^{p} \quad \text{(B.15b)}$$

$$L_1^{p} + M_2^{p} \xrightarrow{k_{f12}^{w}} S_2^{p} + D^{p} + \mathrm{PDB}_e^{p} \quad \text{(B.16b)}$$

$$L_2^{p} + M_1^{p} \xrightarrow{k_{f21}^{w}} S_1^{p} + D^{p} + 2\mathrm{PDB}_e^{p} \quad \text{(B.17b)}$$

$$L_2^{p} + M_2^{p} \xrightarrow{k_{f22}^{w}} S_2^{p} + D^{p} + 2\mathrm{PDB}_e^{p} \quad \text{(B.18b)}$$

Termination by disproportionation

$$L_1^{p} + L_1^{p} \xrightarrow{k_{t11}^{P}} 2D^{P} + \mathrm{PDB}_e^{P} \quad \text{(B.19b)}$$

$$L_1^{p} + L_2^{p} \xrightarrow{k_{t12}^{P}} 2D^{P} + 2\mathrm{PDB}_e^{P} \quad \text{(B.20b)}$$

$$L_2^{p} + L_2^{p} \xrightarrow{k_{t22}^{P}} 2D^{P} + 3\mathrm{PDB}_e^{P} \quad \text{(B.21b)}$$

Reactions with Gelatin

Termination with gelatin

$$L_1^{p} + G^{\cdot p} \xrightarrow{k_{t12}^{P}} D^{P} \quad \text{(B.22b)}$$

$$L_2^{p} + G^{\cdot p} \xrightarrow{k_{t22}^{P}} D^{P} + \mathrm{PDB}_e^{P} \quad \text{(B.23b)}$$

Transfer to gelatin

$$L_1^{p} + G^{P} \xrightarrow{k_{fG1}^{P}} D^{P} + \theta G^{\cdot p} \quad \text{(B.24b)}$$

$$L_2^{p} + G^{P} \xrightarrow{k_{fG2}^{P}} D^{P} + \theta G^{\cdot p} + \mathrm{PDB}_e^{P} \quad \text{(B.25b)}$$

Re-initiation

$$G^{\cdot p} + M_1^{P} \xrightarrow{k_{pG1}^{P}} L_1^{p} + G^{P} \quad \text{(B.26b)}$$

$$G^{\cdot p} + M_2^{P} \xrightarrow{k_{pG2}^{P}} L_2^{p} + G^{P} \quad \text{(B.27b)}$$

Appendix C

Reaction rate equations

Table C.1 lists expressions for all reaction rates used in the species balances, developed from the kinetic scheme given in Table B.1.

Table C.1: Reaction rates.

$$r_{(\mathrm{PR}^{\cdot w})} = -2k_{\mathrm{fast}}[(\mathrm{PR}^{\cdot w})] \tag{C.1a}$$

$$r_{\mathrm{PR}^{\cdot w}} = 2fk_{\mathrm{fast}}[(\mathrm{PR}^{\cdot w})] - [\mathrm{PR}^{\cdot w}](k_{ini1}[M_1^w] + k_{ini2}[M_2^w]) \tag{C.2a}$$

$$\begin{aligned} r_{S_1^w} = {} & \{k_{ini1}[\mathrm{PR}^{\cdot w}][M_1^w] + (k_{p21}^w + k_{f21}^w)[S_2^w][M_1^w] + k_c^w[S_2^w] + k_{pG1}^w[G^{\cdot w}][M_1^w]\} \\ & - \{k_{t12}^w[G^{\cdot w}][S_1^w] + (k_{p12}^w + k_{f12}^w)[S_1^w][M_2^w] + k_{x1}^w[S_1^w][\mathrm{PDB}_e^w] \\ & + 2k_{t11}^w[S_1^w]^2 + k_{t12}^w[S_2^w][S_1^w] + k_{fG1}^w[G^w][S_1^w]\} \end{aligned} \tag{C.3a}$$

$$\begin{aligned} r_{S_2^w} = {} & \{k_{ini2}[\mathrm{PR}^{\cdot w}][M_2^w] + (k_{p12}^w + k_{f12}^w)[S_1^w][M_2^w] + k_{pG2}^w[G^{\cdot w}][M_2^w]\} \\ & - \{k_{t22}^w[G^{\cdot w}][S_2^w] + k_c^w[S_2^w] + (k_{p21}^w + k_{f21}^w)[S_2^w][M_1^w] \\ & + k_{x2}^w[S_2^w][\mathrm{PDB}_e^w] + 2k_{t22}^w[S_2^w]^2 + k_{t12}^w[S_2^w][S_1^w] + k_{fG2}^w[G^w][S_2^w]\} \end{aligned} \tag{C.4a}$$

$$r_{M_1^w} = -[M_1^w](k_{ini1}[\mathrm{PR}^{\cdot w}] + (k_{p11}^w + k_{f11}^w)[S_1^w] + (k_{p21}^w + k_{f21}^w)[S_2^w] + k_{pG1}^w[G^{\cdot w}]) \tag{C.5a}$$

$$r_{M_2^w} = -[M_2^w](k_{ini2}[\mathrm{PR}^{\cdot w}] + (k_{p12}^w + k_{f12}^w)[S_1^w] + (k_{p22}^w + k_{f22}^w)[S_2^w] + k_{pG2}^w[G^{\cdot w}]) \tag{C.6a}$$

$$\begin{aligned} r_{\mathrm{PDB}_e^w} = {} & \{(k_{p21}^w + 2k_{f21}^w)[S_2^w][M_1^w] + (k_{p22}^w + 2k_{f22}^w)[S_2^w][M_2^w] + k_{t11}^w[S_1^w]^2 \\ & + k_{t22}^w[G^{\cdot w}][S_2^w] + 2k_{t12}^w[S_2^w][S_1^w] + 3k_{t22}^w[S_2^w]^2 + k_{fG2}^w[G^w][S_2^w] \\ & + (k_{f11}^w[M_1^w] + k_{f12}^w[M_2^w])[S_1^w]\} \\ & - (k_{x1}^w[S_1^w] + k_{x2}^w[S_2^w])[\mathrm{PDB}_e^w](1 + n_{\mathrm{PDB}}) \end{aligned} \tag{C.7a}$$

$$\begin{aligned} r_{G^{\cdot w}} = {} & [G^w](\theta k_{fG1}^w[S_1^w] + \theta k_{fG2}^w[S_2^w]) \\ & - \{[G^{\cdot w}](k_{pG1}^w[M_1^w] + k_{pG2}^w[M_2^w] + k_{t12}^w[S_1^w] + k_{t22}^w[S_2^w])\} \end{aligned} \tag{C.8a}$$

$$\begin{aligned} r_{D_n^w} = {} & [M_1^w](k_{f11}^w[S_1^w] + k_{f21}^w[S_2^w]) + [M_2^w](k_{f12}^w[S_1^w] + k_{f22}^w[S_2^w]) + 2k_{t11}^w[S_1^w]^2 \\ & + 2k_{t12}^w[S_2^w][S_1^w] + 2k_{t22}^w[S_2^w]^2 + [G^w](k_{fG1}^w[S_1^w] + k_{fG2}^w[S_2^w]) \end{aligned} \tag{C.9a}$$

$$r_{(\mathrm{PR}^{\cdot p})} = -2k_{\mathrm{fast}}[(\mathrm{PR}^{\cdot p})] \tag{C.1b}$$

$$r_{\mathrm{PR}^{\cdot p}} = 2fk_{\mathrm{fast}}[(\mathrm{PR}^{\cdot p})] - [\mathrm{PR}^{\cdot p}]\left(k_{ini1}\left[M_1^p\right] + k_{ini2}\left[M_2^p\right]\right) \tag{C.2b}$$

$$\begin{aligned} r_{L_1^p} = {} & \left\{[M_1^P]\left(k_{p21}^P\left[L_2^p\right] + k_{p21}^P\left[L_3^p\right] + k_{pG1}^P[G^{\cdot p}]\right) + k_c^P\left[L_2^p\right]\right\} \\ & - \left\{k_{p12}^P[M_2^P]\left[L_1^p\right] + k_{x1}^P\left[\mathrm{PDB}_e^P\right]\left[L_1^p\right] + \left(k_{f11}^P\left[M_1^p\right] + k_{f12}^P\left[M_2^p\right]\right)\left[L_1^p\right]\right. \\ & \left. + 2k_{t11}^P\left[L_1^p\right]^2 + k_{t12}^P\left[L_1^p\right]\left[L_2^p\right] + k_{t12}^P\left[L_1^p\right][G^{\cdot p}] + k_{fG1}^P\left[L_1^p\right][G^P]\right\} \end{aligned} \tag{C.3b}$$

$$\begin{aligned} r_{L_2^p} = {} & [M_2^P]\left(k_{p12}^P\left[L_1^p\right] + k_{p22}^P\left[L_3^p\right] + k_{pG2}^P[G^{\cdot p}]\right) \\ & - \left\{k_c^P\left[L_2^p\right] + k_{p21}^P[M_1^P]\left[L_2^p\right] + k_{x2}^P\left[\mathrm{PDB}_e^P\right]\left[L_2^p\right]\right. \\ & + \left(k_{f21}^P\left[M_1^p\right] + k_{f22}^P\left[M_2^p\right]\right)\left[L_2^p\right] + 2k_{t22}^P\left[L_2^p\right]^2 + k_{t12}^P\left[L_1^p\right]\left[L_2^p\right] \\ & \left. + k_{t22}^P\left[L_2^p\right][G^{\cdot p}] + k_{fG2}^P\left[L_2^p\right][G^P]\right\} \end{aligned} \tag{C.4b}$$

$$r_{M_1^P} = -[M_1^P]\left(\left(k_{p11}^P + k_{f11}^P\right)\left[L_1^p\right] + \left(k_{p21}^P + k_{f21}^P\right)\left[L_2^p\right] + k_{p21}^P\left[L_3^p\right] + k_{pG1}^P[G^{\cdot p}]\right) \tag{C.5b}$$

$$r_{M_2^P} = -[M_2^P]\left(\left(k_{p22}^P + k_{f22}^P\right)\left[L_2^p\right] + \left(k_{p12}^P + k_{f12}^P\right)\left[L_1^p\right] + k_{p22}^P\left[L_3^p\right] + k_{pG2}^P[G^{\cdot p}]\right) \tag{C.6b}$$

$$\begin{aligned} r_{\mathrm{PDB}_e^P} = {} & \left\{\left(k_{p21}^P + 2k_{f21}^P\right)[M_1^P]\left[L_2^p\right] + \left(k_{p22}^P + 2k_{f22}^P\right)[M_2^P]\left[L_2^p\right] + k_{t11}^P\left[L_1^p\right]^2\right. \\ & \left. + k_{t22}^P[G^{\cdot p}]\left[L_2^p\right] + 2k_{t12}^P\left[L_2^p\right]\left[L_1^p\right] + 3k_{t22}^P\left[L_2^p\right]^2 + k_{fG2}^P[G^P]\left[L_2^p\right]\right\} \\ & + \left(k_{f11}^P\left[M_1^p\right] + k_{f12}^P\left[M_2^p\right]\right)\left[L_1^p\right] - \left(k_{x1}^P\left[L_1^p\right] + k_{x1'}^P\left[S_1^p\right]\right)\left[\mathrm{PDB}_e^p\right] \end{aligned} \tag{C.7b}$$

$$\begin{aligned} r_{G^{\cdot p}} = {} & \left\{[G^P]\left(\theta k_{fG1}^P\left[L_1^p\right] + \theta k_{fG2}^P\left[L_2^p\right]\right)\right\} \\ & - \left\{[G^{\cdot p}]\left(k_{pG1}^P[M_1^P] + k_{pG2}^P[M_2^P] + k_{t12}^P\left[L_1^p\right] + k_{t22}^P\left[L_2^p\right]\right)\right\} \end{aligned} \tag{C.8b}$$

$$r_{S_1^p} = k_{ini1}[\mathrm{PR}^{\cdot p}]\left[M_1^p\right] + \left(k_{f11}^P\left[L_1^p\right] + k_{f21}^P\left[L_2^p\right]\right)[M_1^P] - k_{x1'}^P\left[S_1^p\right]\left[\mathrm{PDB}_e^p\right] \tag{C.9b}$$

$$r_{S_2^p} = k_{ini2}[\mathrm{PR}^{\cdot p}]\left[M_2^p\right] + \left(k_{f12}^P\left[L_1^p\right] + k_{f22}^P\left[L_2^p\right]\right)[M_2^P] - k_{x2'}^P\left[S_2^p\right]\left[\mathrm{PDB}_e^p\right] \tag{C.10b}$$

$$\begin{aligned} r_{L_3^p} = {} & \left(k_{x1}^P\left[L_1^p\right] + k_{x1'}^P\left[S_1^p\right] + k_{x2}^P\left[L_2^p\right] + k_{x2'}^P\left[S_2^p\right]\right)\left[\mathrm{PDB}_e^P\right] \\ & - \left[L_3^p\right]\left(k_{p21}^P[M_1^P] + k_{p22}^P[M_2^P]\right) \end{aligned} \tag{C.11b}$$

$$
\begin{aligned}
r_{\lambda_{1,1}} = {} & \left\{k_{ini1}[\mathrm{PR}^{\cdot}][M_1^w] + k_{p11}^w\lambda_{0,1}[M_1^w] + k_{p21}^w\left(\lambda_{0,2}+\lambda_{1,2}\right)[M_1^w] + k_c^w\lambda_{1,2}\right. \\
& + k_{pG1}^w[G^{\cdot w}][M_1^w] + \left(k_{f11}^w\lambda_{0,1} + k_{f21}^w\lambda_{0,2}\right)[M_1^w]\Big\} \\
& - \Big\{\lambda_{1,1}\left(k_{p12}^w[M_2^w] + k_{x1}^w[PDB_e^w] + 2k_{t11}^w\lambda_{0,1} + k_{t12}^w\lambda_{0,2} + k_{fG1}^w[G^w]\right. \\
& \left.\left. + k_{f11}^w[M_1^w] + k_{f12}^w[M_2^w]\right)\right\}
\end{aligned}
\tag{C.1c}
$$

$$
\begin{aligned}
r_{\lambda_{1,2}} = {} & \left\{k_{ini2}[\mathrm{PR}^{\cdot}][M_2^w] + k_{p22}^w\lambda_{0,2}[M_2^w] + k_{p12}^w\left(\lambda_{0,1}+\lambda_{1,1}\right)[M_2^w] + k_{pG2}^w[G^{\cdot w}][M_2^w]\right. \\
& \left. + \left(k_{f22}^w\lambda_{0,2} + k_{f12}^w\lambda_{0,1}\right)[M_2^w]\right\} \\
& - \Big\{k_c^w\lambda_{1,2} \\
& + \lambda_{1,2}\left(k_{p21}^w[M_1^w] + k_{x2}^w[PDB_e^w] + 2k_{t22}^w\lambda_{0,2} + k_{t12}^w\lambda_{0,1} + k_{fG2}^w[G^w]\right. \\
& \left.\left. + k_{f22}^w[M_2^w] + k_{f21}^w[M_1^w]\right)\right\}
\end{aligned}
\tag{C.2c}
$$

$$
\begin{aligned}
r_{\lambda_{2,1}} = {} & \left\{k_{ini1}[\mathrm{PR}^{\cdot}][M_1^w] + k_{p11}^w\left(2\lambda_{1,1}+\lambda_{0,1}\right)[M_1^w] + k_{p21}^w\left(\lambda_{0,2}+2\lambda_{1,2}+\lambda_{2,2}\right)[M_1^w]\right. \\
& + k_c^w\lambda_{1,2} + k_{pG1}^w[G^{\cdot w}][M_1^w] + \left(k_{f11}^w\lambda_{0,1} + k_{f21}^w\lambda_{0,2}\right)[M_1^w]\Big\} \\
& - \Big\{\lambda_{2,1}\left(k_{p12}^w[M_2^w] + k_{x1}^w[PDB_e^w] + 2k_{t11}^w\lambda_{0,1} + k_{t12}^w\lambda_{0,2} + k_{fG1}^w[G^w]\right. \\
& \left.\left. + k_{f11}^w[M_1^w] + k_{f12}^w[M_2^w]\right)\right\}
\end{aligned}
\tag{C.3c}
$$

$$
\begin{aligned}
r_{\lambda_{2,2}} = {} & \left\{k_{ini2}[\mathrm{PR}^{\cdot}][M_2^w] + k_{p22}^w\left(2\lambda_{1,2}+\lambda_{0,2}\right)[M_2^w] + k_{p12}^w\left(\lambda_{0,1}+2\lambda_{1,1}+\lambda_{2,1}\right)[M_2^w]\right. \\
& + k_{pG2}^w[G^{\cdot w}][M_2^w] + \left(k_{f22}^w\lambda_{0,2} + k_{f12}^w\lambda_{0,1}\right)[M_2^w]\Big\} \\
& - \Big\{k_c^w\lambda_{2,2} \\
& + \lambda_{2,2}\left(k_{p21}^w[M_1^w] + k_{x2}^w[PDB_e^w] + 2k_{t22}^w\lambda_{0,2} + k_{t12}^w\lambda_{0,1} + k_{fG2}^w[G^w]\right. \\
& \left.\left. + k_{f22}^w[M_2^w] + k_{f21}^w[M_1^w]\right)\right\}
\end{aligned}
\tag{C.4c}
$$

$$
\begin{aligned}
r_T = {} & \Big\{[M_1^{\mathrm{w}}]\left(k_{ini1}[\mathrm{PR}^{\cdot w}] + k_{p11}^w[S_1^w] + k_{p21}^w[S_2^w] + k_{pG1}^w[G^{\cdot w}]\right) \\
& + [M_2^{\mathrm{w}}]\left(k_{ini2}[\mathrm{PR}^{\cdot w}] + k_{p12}^w[S_1^w] + k_{p22}^w[S_2^w] + k_{pG2}^w[G^{\cdot w}]\right) \\
& + \left(k_{x1}^w[S_1^w] + k_{x2}^w[S_2^w]\right)[\mathrm{PDB}_e^w] + k_c^w[S_2^w]\Big\}\phi \\
& + \Big\{[M_1^p]\left(k_{p11}^p\left[L_1^p\right] + k_{p21}^p\left[L_2^p\right] + k_{p21}^p\left[L_3^p\right] + k_{pG1}^p[G^{\cdot p}]\right) + k_c^p\left[L_2^p\right] \\
& + \left[M_2^{\mathrm{p}}\right]\left(k_{p12}^p\left[L_1^p\right] + k_{p22}^p\left[L_2^p\right] + k_{p22}^p\left[L_3^p\right] + k_{pG2}^p[G^{\cdot p}]\right) \\
& + \left(k_{x1}^p\left[L_1^p\right] + k_{x1'}^p\left[S_1^p\right] + k_{x2}^p\left[L_2^p\right] + k_{x2'}^p\left[S_2^p\right]\right)\left[\mathrm{PDB}_e^p\right]\Big\}(1-\phi)
\end{aligned}
\tag{C.5c}
$$

Appendix D

Parameter estimates

Table D.1 lists parameters required for polymer gel dosimeter simulations.

Table D.1: List of parameters used in the extended model.

Parameter	Value	Description	Units	Source
k_{ini_1}	$\approx 1 \times 10^{10}$	Initiation rate constant for reaction between primary radical and monomer.	L mol^{-1} s^{-1}	[1]
$k_{p_{11}}^0$	$1.65 \times 10^6 \, exp$ (-2743/RT)	Propagation rate coefficient in the absence of diffusion control.	L mol^{-1} s^{-1}	[2]
k_{pg}	3.676×10^{-3}	Propagation of gelatin-centred radicals	Lmol^{-1} s^{-1}	[10]
$k_{f_{11}}^0$	$9.55 \times 10^6 \, exp$ (-10438/RT)	Rate coefficient for transfer reaction between a macroradical and monomer.	L mol^{-1} s^{-1}	[2]
k_{fg}	0.02825	Chain transfer to gelatin	L mol^{-1} s^{-1}	[10]
$k_{t_{11}}^0$	$(1532 \, exp$ (-741/RT))^2	Bimolecular termination rate coefficient in the absence of diffusion control.	L mol^{-1} s^{-1}	[2]
k_c	1.1495×10^4	Primary cyclization	s^{-1}	[10]
$k_{p_{11}}^0/k_{p_{12}}^o$	0.5		-	[3]
$k_{p_{22}}^0/k_{p_{21}}^0$	2		-	[3]
θ	0.929993	Fraction of gelatin-centred radicals that can propagate		[10]
σ_{M_1}	5.02×10^{-8}	Lennard-Jones diameter of acrylamide monomer.	cm	[4,5]

Parameter	Value	Description	Units	Source
σ_{M_2}	6.42×10^{-8}	Lennard-Jones diameter of bisacrylamide monomer.	cm	[4,5]
a_1	1.54×10^{-8}	Mean distance travelled by a radical when an acrylamide monomer unit is added.	cm	[6]
$D_{M_1^w}$	4×10^{-6}	Diffusivity in the water phase of acrylamide monomer.	$cm^2\ s^{-1}$	[7]
$D_{H_2O^w}$	1.5×10^{-5}	Diffusivity in the water phase of water.	$cm^2\ s^{-1}$	[7]
C_p	4184	Heat capacity of the PAG gel system.	$J\ kg^{-1}\ K^{-1}$	[8]
$-\Delta H_R$	81500	Enthalpy of the reaction.	$J\ mol^{-1}$	[2]
$k_{cond}^{20°C}$	5.98×10^{-3}	Thermal conductivity in the PAG gel dosimeter at 20°C.	$J\ cm^{-1}\ K^{-1}\ s^{-1}$	[7]
h	5×10^{-3}	Heat transfer coefficient for heat transfer from the PAG to the surrounding environment.	$J\ cm^{-2}\ K^{-1}\ s^{-1}$	[9]
$G_{(e_{aq}+H^{\cdot}+OH^{\cdot})^{\cdot}}$	6.27×10^{-7}	Chemical yield of $H^{\bullet}$, e^-_{aq} or $OH^{\bullet}$	$mol\ J^{-1}$	[8]
Φ_{PDB}	0.1	Fraction of pendant vinyl groups in polymer phase that can crosslink with aqueous-phase radicals.	-	[7]
$\Phi_{\mathrm{H_2O}}$	0.6817	Partition coefficient for water between polymer and aqueous phases	$\frac{mol/L_{pol}}{mol/L_{aq}}$	[10]
Φ_{M}	0.0881	Partition coefficient for monomers between polymer and aqueous phases	$\frac{mol/L_{pol}}{mol/L_{aq}}$	[10]

Parameter	Value	Description	Units	Source
f	0.5	Radical efficiency in aqueous phase.	-	[7]
$D_{M_1^w}$	1.0×10^{-11}	Diffusivity of acrylamide in polymer phase.	$cm^2\ s^{-1}$	[7]
$D_{M_2^w}$	3/4 $D_{M_1^w}$	Diffusivity of bisacrylamide in polymer phase.	$cm^2\ s^{-1}$	[7]
$k_{x_1}^0$	k_{p11}^0	Rate constant for reaction between a macroradical bearing the active radical on a acrylamide unit and un-reacted double bond.	$L\ mol^{-1}s^{-1}$	[7]
D_{PR^w}	10 $D_{M_1^w}$	Dead primary radicals in the aqueous phase.	$cm^2\ s^{-1}$	[7]
$D_{S_1^w}$	Varied from $D_{M_1^w}$ to 0	Dead polymer chain bearing the active radical on an acrylamide unit.	$cm^2\ s^{-1}$	[7]
$D_{S_2^w}$	$D_{S_1^w}$	Dead polymer chain bearing the active radical on a bisacrylamide unit.	$cm^2\ s^{-1}$	[7]
a_2	2 a_1	Mean distance travelled by a radical when a bisacrylamide monomer unit is added.	cm	[7]
Φ_{G}	1	Ratio of the concentration of gelatin in the polymer phase over its concentration in aqueous phase.	-	[7]
ν	2	Ratio of reactivity of radicals with terminal acrylamide to radicals with bisacrylamide	-	[7]

D.1 References for Appendix D

[1] Spinks J W T and Woods R J 1976 *An introduction to radiation chemistry, 2nd ed*. (New York: John Wiley & Sons)

[2] Hernandez-Barajas J and Hunkeler D J 1997 Inverse-emulsion polymerization of acrylamide using block copolymeric surfactants: mechanism, kinetics and modelling *Polymer* **38** 437-47

[3] Tobita H and Hamielec A E 1990 Cross-linking kinetics in polyacrylamide networks *Polymer* **31** 1546-52

[4] Russell G T, Napper D H and Gilbert R G 1988 Termination in free-radical polymerizing systems at high conversion *Macromolecules* **21** 2133-49

[5] Reis R C, Prausnitz J M and Poling B E 1987 *The properties of gases and liquids* (New York: McGraw-Hill)

[6] Orwoll R A and Chong Y S 1999 *Polymer data handbook, J E Mark Ed*. (Oxford: Oxford University Press)

[7] Fuxman A M, McAuley K B, and Schreiner L J 2003 Modeling of free-radical crosslinking copolymerization of acrylamide and N,N'-methylenebis(acrylamide) for radiation dosimetry *Macromol. Theory Simul.* **12** 647-62

[8] Salomons G J, Park Y S, McAuley K B and Schreiner L J 2002 Temperature increases associated with polymerization of irradiated PAG dosimeters *Phys. Med. Biol.* **47** 1435-48

[9] Baldock C, Burford R P, Billingham N, Wagner G S, Patval S, Badawi R D and Keevil S F 1998 Experimental procedure for the manufacture and calibration of polyacrylamide gel (PAG) for magnetic resonance imaging (MRI) radiation dosimetry *Phys. Med. Biol.* **43** 695-702

[10] Koeva V I, Daneshvar S, Senden R J, Imam A H M, Schreiner L J and McAuley K B 2009 Mathematical modeling of PAG- and NIPAM-based polymer gel dosimeters contaminated by oxygen and inhibitor *Macromol. Theory Simul*. **18** 495-510

Appendix E

Summary of model extensions

Table E.1 summarizes all of the additions and modifications made to the reaction scheme and equations of the Fuxman *et al.* (2005) model, prior to the coordinate transformation, during the development of the extended model.

Table E. 1: List of extensions and modifications to the previous Fuxman *et al.* (2005) model.

Boundary Conditions	
$k_{\text{cond}} \left.\frac{\partial T}{\partial x}\right\|_{x=0} = h(T - T_s)$	(E.31)
PDEs	
$\frac{\partial[(\text{PR}^{\cdot})]}{\partial t} = \Gamma(x) R_{(\text{PR}^{\cdot})}[\text{H}_2\text{O}] M_{w,\text{H}_2\text{O}} - r_{(\text{PR}^{\cdot})} - \frac{[(\text{PR}^{\cdot})]}{\phi}\frac{\partial \phi}{\partial t}$	(E.32)
$\frac{\partial[\text{PDB}_e^p]}{\partial t} = r_{\text{PDB}_e^p} + n_{\text{PDB}}\{(k_{x1}^w[S_{1,n}^w] + k_{x2}^w[S_{2,n}^w])([\text{PDB}_e^w])\}\frac{\phi}{(1-\phi)} + \frac{[\text{PDB}_e^p]}{(1-\phi)}\frac{\partial \phi}{\partial t}$	(E.33)
Reaction Mechanisms	
$S_{1,n}^w + G^{\cdot w} \xrightarrow{k_{t12}^w} D_n^w$	(E.34)
$S_{2,n}^w + G^{\cdot w} \xrightarrow{k_{t22}^w} D_n^w + \text{PDB}_e^w$	(E.35)
$L_1^p + G^{\cdot p} \xrightarrow{k_{t12}^P} D^P$	(E.36)
$L_2^p + G^{\cdot p} \xrightarrow{k_{t22}^P} D^P + \text{PDB}_e^P$	(E.37)

Reaction Rates

$$r_{S_1^w} = \{k_{i1}[\mathrm{PR}^{\cdot w}][M_1^w] + (k_{p21}^w + k_{f21}^w)[S_2^w][M_1^w] + k_c^w[S_2^w] + k_{pG1}^w[G^{\cdot w}][M_1^w]\} - \{k_{t12}^w[G^{\cdot w}][S_1^w] + (k_{p12}^w + k_{f12}^w)[S_1^w][M_2^w] + k_{x1}^w[S_1^w][\mathrm{PDB}_e^w] + 2k_{t11}^w[S_1^w]^2 + k_{t12}^w[S_2^w][S_1^w] + k_{fG1}^w[G^w][S_1^w]\} \quad \text{(E.38)}$$

$$r_{S_2^w} = \{k_{i2}[\mathrm{PR}^{\cdot w}][M_2^w] + (k_{p12}^w + k_{f12}^w)[S_1^w][M_2^w] + k_{pG2}^w[G^{\cdot w}][M_2^w]\} - \{k_{t22}^w[G^{\cdot w}][S_2^w] + k_c^w[S_2^w] + (k_{p21}^w + k_{f21}^w)[S_2^w][M_1^w] + k_{x2}^w[S_2^w][\mathrm{PDB}_e^w] + 2k_{t22}^w[S_2^w]^2 + k_{t12}^w[S_2^w][S_1^w] + k_{fG2}^w[G^w][S_2^w]\} \quad \text{(E.39)}$$

$$r_{\mathrm{PDB}_e^w} = \{(k_{p21}^w + 2k_{f21}^w)[S_2^w][M_1^w] + (k_{p22}^w + 2k_{f22}^w)[S_2^w][M_2^w] + k_{t11}^w[S_1^w]^2 + k_{t22}^w[G^{\cdot w}][S_2^w] + 2k_{t12}^w[S_2^w][S_1^w] + 3k_{t22}^w[S_2^w]^2 + k_{fG2}^w[G^w][S_2^w] + (k_{f11}^w[M_1^w] + k_{f12}^w[M_2^w])[S_1^w]\} - (k_{x1}^w[S_1^w] + k_{x2}^w[S_2^w])[\mathrm{PDB}_e^w](1 + n_{\mathrm{PDB}}) \quad \text{(E.40)}$$

$$r_{G^{\cdot w}} = \{[G^w](\theta k_{fG1}^w[S_1^w] + \theta k_{fG2}^w[S_2^w])\} - \{[G^{\cdot w}](k_{pG1}^w[M_1^w] + k_{pG2}^w[M_2^w] + k_{t12}^w[S_1^w] + k_{t22}^w[S_2^w])\} \quad \text{(E.41)}$$

$$r_{L_1^p} = \{[M_1^P](k_{p21}^P[L_2^p] + k_{p21}^P[L_3^p] + k_{pG1}^P[G^{\cdot p}]) + k_c^P[L_2^p]\} - \{k_{p12}^P[M_2^P][L_1^p] + k_{x1}^P[\mathrm{PDB}_e^p][L_1^p] + (k_{f11}^P[M_1^p] + k_{f12}^P[M_2^p])[L_1^p] + 2k_{t11}^P[L_1^p]^2 + k_{t12}^P[L_1^p][L_2^p] + k_{t12}^P[L_1^p][G^{\cdot p}] + k_{fG1}^P[L_1^p][G^P]\} \quad \text{(E.42)}$$

$$r_{L_2^p} = \{[M_2^P](k_{p12}^P[L_1^p] + k_{p22}^P[L_3^p] + k_{pG2}^P[G^{\cdot p}])\} - \{k_c^P[L_2^p] + k_{p21}^P[M_1^P][L_2^p] + k_{x2}^P[\mathrm{PDB}_e^P][L_2^p] + (k_{f21}^P[M_1^p] + k_{f22}^P[M_2^p])[L_2^p] + 2k_{t22}^P[L_2^p]^2 + k_{t12}^P[L_1^p][L_2^p] + k_{t22}^P[L_2^p][G^{\cdot p}] + k_{fG2}^P[L_2^p][G^P]\} \quad \text{(E.43)}$$

$$r_{\mathrm{PDB}_e^P} = \{(k_{p21}^P + 2k_{f21}^P)[M_1^P][L_2^p] + (k_{p22}^P + 2k_{f22}^P)[M_2^P][L_2^p] + k_{t11}^P[L_1^p]^2 + k_{t22}^P[G^{\cdot p}][L_2^p] + 2k_{t12}^P[L_2^p][L_1^p] + 3k_{t22}^P[L_2^p]^2 + k_{fG2}^P[G^P][L_2^p]\} + (k_{f11}^P[M_1^p] + k_{f12}^P[M_2^p])[L_1^p] - \{(k_{x1}^P[L_1^p] + k_{x1,}^P[S_1^p])[\mathrm{PDB}_e^p]\} \quad \text{(E.44)}$$

$$r_{G^{\cdot p}} = \{[G^P](\theta k_{fG1}^P[L_1^p] + \theta k_{fG2}^P[L_2^p])\} - \{[G^{\cdot p}](k_{pG1}^P[M_1^P] + k_{pG2}^P[M_2^P] + k_{t12}^P[L_1^p] + k_{t22}^P[L_2^p])\} \quad \text{(E.45)}$$

Appendix F
Cubic spline fits

Figures F.1 to F.5 shows the accuracy of the cubic spline fits to their respective radiation depth-dose data. Each cublic spline is nearly a perfect match to its experimental depth-dose data.

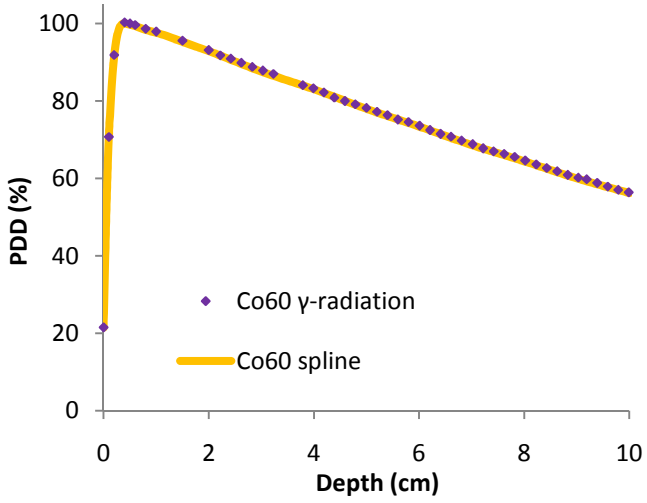

Figure F.1: Plot comparing PDD data and spline fit for Co^{60} γ-radiation.

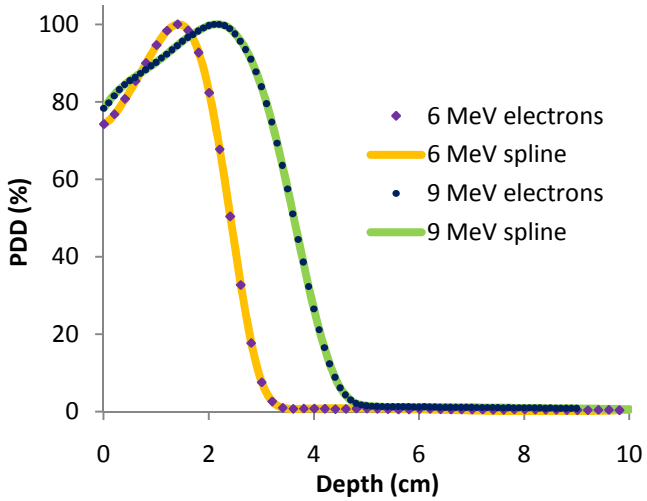

Figure F.2: Plot comparing PDD data and spline fit for 6 MeV and 9 MeV electron radiations.

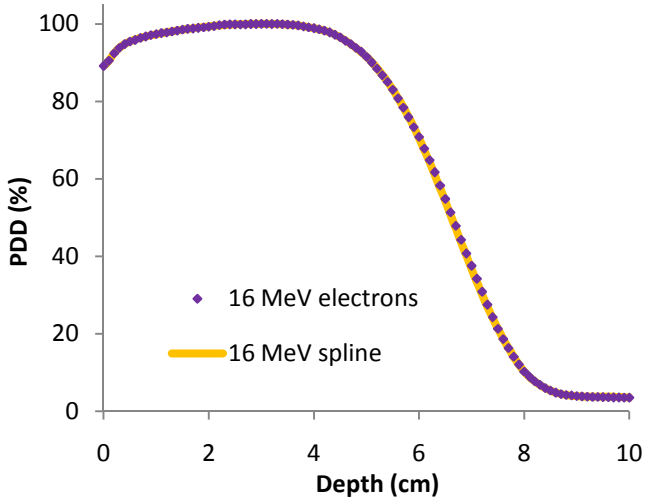

Figure F.3: Plot comparing PDD data and spline fit for 16 MeV electron radiation.

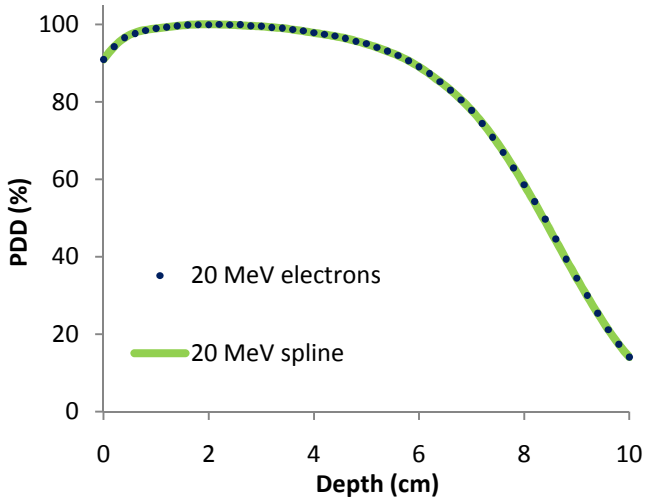

Figure F.4: Plot comparing PDD data and spline fit for 20 MeV electron radiation.

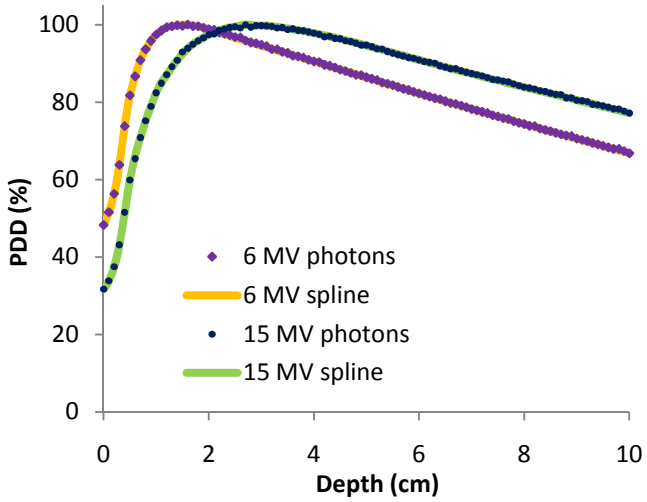

Figure F.5: Plot comparing PDD data and spline fit for 6 MV and 15 MV photon radiations.

Appendix G

Transformed balance equations

To properly investigate depth-dose behaviour, a large depth ($x = d_b$) is considered for the horizontal axis. However, the VLUGR2 algorithm solves partial differential equations (PDEs) on a spatial domain where the horizontal axis (w) extends from 0 to 1. Therefore, a coordinate transformation is used to solve the system of PDEs presented in Chapter 2. All terms within the PDEs which contained the original x coordinate were replaced by the transformed variable w. The following equations describe the relationship between the original (x) and transformed (w) coordinates.

$$w = \frac{x}{d_b}$$

$$\frac{\partial w}{\partial x} = \frac{1}{d_b}$$

The PDEs in the extended model contain first and second derivatives with respect to x, which need to be transformed. The following is an example of a first derivative transformation of a random variable Ψ.

$$\frac{\partial \Psi}{\partial x} = \frac{\partial \Psi}{\partial w} \cdot \frac{\partial w}{\partial x} = \frac{\partial \Psi}{\partial w} \cdot \frac{1}{d_b}$$

A second derivative transformation on the same variable Ψ is shown below.

$$\frac{\partial^2 \Psi}{\partial x^2} = \frac{\partial \left(\frac{\partial \Psi}{\partial x}\right)}{\partial x} = \frac{\partial \left(\frac{\partial \Psi}{\partial w} \cdot \frac{\partial w}{\partial x}\right)}{\partial w} \frac{\partial w}{\partial x} = \frac{\partial \left(\frac{\partial \Psi}{\partial w} \cdot \frac{1}{d_b}\right)}{\partial w} \frac{1}{d_b}$$

$$\therefore \frac{\partial^2 \Psi}{\partial x^2} = \left(\frac{1}{d_b}\right)^2 \frac{\partial^2 \Psi}{\partial w^2}$$

Transformations on first and second derivatives of all PDEs are implemented. Below shows the original and transformed PDEs on acrylamide concentration.

$$\frac{\partial[M_1^w]}{\partial t} = D_{M_1^w}\left(\frac{1}{\phi}\frac{\partial\phi}{\partial x}\frac{\partial[M_1^w]}{\partial x} + \frac{\partial^2[M_1^w]}{\partial x^2}\right) + r_{M_1^w} - k_m\left([M_1^w] - \frac{[M_1^p]}{\Phi_{M_1}}\right) - \frac{[M_1^w]}{\phi}\frac{\partial\phi}{\partial t}$$

$$\frac{\partial[M_1^w]}{\partial t} = D_{M_1^w}\left(\frac{1}{d_b}\right)^2\left(\frac{1}{\phi}\frac{\partial\phi}{\partial w}\frac{\partial[M_1^w]}{\partial w} + \frac{\partial^2[M_1^w]}{\partial w^2}\right) + r_{M_1^w} - k_m\left([M_1^w] - \frac{[M_1^p]}{\Phi_{M_1}}\right) - \frac{[M_1^w]}{\phi}\frac{\partial\phi}{\partial t}$$

Table G.1 and Table G.2 list all transformed species balance equations, in the aqueous and polymer phases, used in the extended model. Table G.3 lists overall balance equations and Table G.4 lists transformed boundary conditions for the extended model.

Table G.1: Species balance equations for the aqueous phase of the transformed extended model.

$$\frac{\partial[(\mathrm{PR}^{\cdot w})]}{\partial t} = \Gamma(w) R_{(\mathrm{PR}^{\cdot w})}[\mathrm{H_2O}^w] M_{w,\mathrm{H_2O}} - r_{(\mathrm{PR}^{\cdot w})} - \frac{[(\mathrm{PR}^{\cdot w})]}{\phi}\frac{\partial \phi}{\partial t} \tag{G.1a}$$

$$\frac{\partial[\mathrm{PR}^{\cdot w}]}{\partial t} = D_{\mathrm{PR}^{\cdot}} \left(\frac{1}{d_b}\right)^2 \left(\frac{1}{\phi}\frac{\partial \phi}{\partial w}\frac{\partial[\mathrm{PR}^{\cdot w}]}{\partial w} + \frac{\partial^2[\mathrm{PR}^{\cdot w}]}{\partial w^2}\right) + r_{\mathrm{PR}^{\cdot w}} - \frac{[\mathrm{PR}^{\cdot w}]}{\phi}\frac{\partial \phi}{\partial t} \tag{G.2a}$$

$$\frac{\partial[S_1^w]}{\partial t} = D_{S_1^w} \left(\frac{1}{d_b}\right)^2 \left(\frac{1}{\phi}\frac{\partial \phi}{\partial w}\frac{\partial[S_1^w]}{\partial w} + \frac{\partial^2[S_1^w]}{\partial w^2}\right) + r_{S_1^w} - \frac{[S_1^w]}{\phi}\frac{\partial \phi}{\partial t} \tag{G.3a}$$

$$\frac{\partial[S_2^w]}{\partial t} = D_{S_2^w} \left(\frac{1}{d_b}\right)^2 \left(\frac{1}{\phi}\frac{\partial \phi}{\partial w}\frac{\partial[S_2^w]}{\partial w} + \frac{\partial^2[S_2^w]}{\partial w^2}\right) + r_{S_2^w} - \frac{[S_2^w]}{\phi}\frac{\partial \phi}{\partial t} \tag{G.4a}$$

$$\frac{\partial[M_1^w]}{\partial t} = D_{M_1^w} \left(\frac{1}{d_b}\right)^2 \left(\frac{1}{\phi}\frac{\partial \phi}{\partial w}\frac{\partial[M_1^w]}{\partial w} + \frac{\partial^2[M_1^w]}{\partial w^2}\right) + r_{M_1^w} - k_m \left([M_1^w] - \frac{[M_1^p]}{\Phi_{\mathrm{M_1}}}\right) - \frac{[M_1^w]}{\phi}\frac{\partial \phi}{\partial t} \tag{G.5a}$$

$$\frac{\partial[M_2^w]}{\partial t} = D_{M_2^w} \left(\frac{1}{d_b}\right)^2 \left(\frac{1}{\phi}\frac{\partial \phi}{\partial w}\frac{\partial[M_2^w]}{\partial w} + \frac{\partial^2[M_2^w]}{\partial w^2}\right) + r_{M_2^w} - k_m \left([M_2^w] - \frac{[M_2^p]}{\Phi_{\mathrm{M_2}}}\right) - \frac{[M_2^w]}{\phi}\frac{\partial \phi}{\partial t} \tag{G.6a}$$

$$\frac{\partial[\mathrm{PDB}_e^w]}{\partial t} = D_{\mathrm{PDB}^{\mathrm{w}}} \left(\frac{1}{d_b}\right)^2 \left(\frac{1}{\phi}\frac{\partial \phi}{\partial w}\frac{\partial[\mathrm{PDB}_e^w]}{\partial w} + \frac{\partial^2[\mathrm{PDB}_e^w]}{\partial w^2}\right) + r_{\mathrm{PDB}_e^w} - \frac{[\mathrm{PDB}_e^w]}{\phi}\frac{\partial \phi}{\partial t} \tag{G.7a}$$

$$\frac{\partial[G^{\cdot w}]}{\partial t} = r_{G^{\cdot w}} - \frac{[G^{\cdot w}]}{\phi}\frac{\partial \phi}{\partial t} \tag{G.8a}$$

$$\frac{\partial[\mathrm{H_2O}^w]}{\partial t} = D_{\mathrm{H_2O}^w} \left(\frac{1}{d_b}\right)^2 \left(\frac{1}{\phi}\frac{\partial \phi}{\partial w}\frac{\partial[\mathrm{H_2O}^w]}{\partial w} + \frac{\partial^2[\mathrm{H_2O}^w]}{\partial w^2}\right) - k_m \left([\mathrm{H_2O}^w] - \frac{[\mathrm{H_2O}^p]}{\Phi_{\mathrm{H_2O}}}\right) - \frac{[\mathrm{H_2O}^w]}{\phi}\frac{\partial \phi}{\partial t} \tag{G.9a}$$

$$\frac{\partial[D^w]}{\partial t} = D_{D^w} \left(\frac{1}{d_b}\right)^2 \left(\frac{1}{\phi}\frac{\partial \phi}{\partial w}\frac{\partial[D^w]}{\partial w} + \frac{\partial^2[D^w]}{\partial w^2}\right) + r_{D^w} - \frac{[D^w]}{\phi}\frac{\partial \phi}{\partial t} \tag{G.10a}$$

Table G.2: Species balance equations for the polymer phase of the transformed extended model.

$$\frac{\partial[(\mathrm{PR}^{\cdot p})]}{\partial t} = \Gamma(w) R_{(\mathrm{PR}^{\cdot p})}[\mathrm{H_2O}^p] M_{w,\mathrm{H_2O}} + r_{(\mathrm{PR}^{\cdot p})} + \frac{[(\mathrm{PR}^{\cdot p})]}{(1-\phi)}\frac{\partial \phi}{\partial t} \tag{G.1b}$$

$$\frac{\partial[\mathrm{PR}^{\cdot p}]}{\partial t} = r_{\mathrm{PR}^{\cdot p}} + \frac{[\mathrm{PR}^{\cdot p}]}{(1-\phi)}\frac{\partial \phi}{\partial t} \tag{G.2b}$$

$$\frac{\partial[L_1^p]}{\partial t} = r_{L_1^p} + \frac{[L_1^p]}{(1-\phi)}\frac{\partial \phi}{\partial t} \tag{G.3b}$$

$$\frac{\partial[L_2^p]}{\partial t} = r_{L_2^p} + \frac{[L_2^p]}{(1-\phi)}\frac{\partial \phi}{\partial t} \tag{G.4b}$$

$$\frac{\partial[M_1^p]}{\partial t} = r_{M_1^p} + k_m \frac{\phi}{(1-\phi)}\left([M_1^w] - \frac{[M_1^p]}{\Phi_{\mathrm{M_1}}}\right) + \frac{[M_1^p]}{(1-\phi)}\frac{\partial \phi}{\partial t} \tag{G.5b}$$

$$\frac{\partial[M_2^p]}{\partial t} = r_{M_2^p} + k_m \frac{\phi}{(1-\phi)}\left([M_2^w] - \frac{[M_2^p]}{\Phi_{\mathrm{M_2}}}\right) + \frac{[M_2^p]}{(1-\phi)}\frac{\partial \phi}{\partial t} \tag{G.6b}$$

$$\frac{\partial[\mathrm{PDB}_e^p]}{\partial t} = r_{PDB_e^p} + n_{\mathrm{PDB}}(k_{x1}^w[S_1^w] + k_{x2}^w[S_2^w])[\mathrm{PDB}_e^w]\frac{\phi}{(1-\phi)} + \frac{[\mathrm{PDB}_e^p]}{(1-\phi)}\frac{\partial \phi}{\partial t} \tag{G.7b}$$

$$\frac{\partial[G^{\cdot p}]}{\partial t} = r_{G^{\cdot p}} + \frac{[G^{\cdot p}]}{(1-\phi)}\frac{\partial \phi}{\partial t} \tag{G.8b}$$

$$\frac{\partial[\mathrm{H_2O}^p]}{\partial t} = k_m \frac{\phi}{(1-\phi)}\left([\mathrm{H_2O}^w] - \frac{[\mathrm{H_2O}^p]}{\Phi_{\mathrm{H_2O}}}\right) + \frac{[\mathrm{H_2O}^p]}{(1-\phi)}\frac{\partial \phi}{\partial t} \tag{G.9b}$$

$$\frac{\partial[S_1^p]}{\partial t} = r_{S_1^p} + \frac{[S_1^p]}{(1-\phi)}\frac{\partial \phi}{\partial t} \tag{G.10b}$$

$$\frac{\partial[S_2^p]}{\partial t} = r_{S_2^p} + \frac{[S_2^p]}{(1-\phi)}\frac{\partial \phi}{\partial t} \tag{G.11b}$$

$$\frac{\partial[L_3^p]}{\partial t} = r_{L_3^p} + (k_{x1}^w[S_1^w] + k_{x2}^w[S_2^w])[\mathrm{PDB}_e^w]\frac{\phi}{(1-\phi)} + \frac{[L_3^p]}{(1-\phi)}\frac{\partial \phi}{\partial t} \tag{G.12b}$$

Table G.3: Overall balance equations for the transformed extended model.

$$\frac{\partial[C]}{\partial t} = k_c^w[S_2^w]\phi + k_c^p[L_2^w](1-\phi) \tag{G.1c}$$

$$\frac{\partial[X]}{\partial t} = (k_{x1}^w[S_1^w] + k_{x2}^w[S_2^w])[\mathrm{PDB}_e^w]\phi + \left(k_{x1}^p[L_1^p] + k_{x1}^p,[S_1^p] + k_{x2}^p[L_2^p] + k_{x2}^p,[S_2^p]\right)[\mathrm{PDB}_e^p](1-\phi) \tag{G.2c}$$

$$\begin{aligned}\frac{\partial[\phi]}{\partial t} = &-\left(k_{x1}^w[S_1^w]\bar{S}_{w,1} + k_{x2}^w[S_2^w]\bar{S}_{w,2}\right)[\mathrm{PDB}_e^w]V_{av}\phi - k_m\left([M_1^w] - \frac{[M_1^p]}{\Phi_{\mathrm{M}_1}}\right)\phi\frac{M_{w,M_1}}{\rho_{M_1}} \\ &- k_m\left([M_2^w] - \frac{[M_2^p]}{\Phi_{\mathrm{M}_2}}\right)\phi\frac{M_{w,M_2}}{\rho_{M_2}} - k_m\left([\mathrm{H_2O}^w] - \frac{[\mathrm{H_2O}^p]}{\Phi_{\mathrm{H_2O}}}\right)\phi\frac{M_{w,\mathrm{H_2O}}}{\rho_{\mathrm{H_2O}}} \\ &+ [G^p]\frac{M_{w,G}}{\rho_G}\frac{\partial\phi}{\partial t}\end{aligned} \tag{G.3c}$$

where $$\bar{S}_{w,1} = \frac{\lambda_{2,1}}{\lambda_{1,1}}, \qquad \bar{S}_{w,2} = \frac{\lambda_{2,2}}{\lambda_{1,2}}$$

and $$V_{av} = \left(\frac{M_{w,M_1}\left(\rho_{M_1}\right)^{-1}[C_1] + M_{w,M_2}\left(\rho_{M_2}\right)^{-1}[C_2]}{([C_1] + [C_2])}\right)$$

$$\frac{\partial\lambda_{0,1}}{\partial t} = \frac{\partial[S_1^w]}{\partial t} \tag{G.4c}$$

$$\frac{\partial\lambda_{0,2}}{\partial t} = \frac{\partial[S_1^w]}{\partial t} \tag{G.5c}$$

$$\frac{\partial\lambda_{i,j}}{\partial t} = D_{S_j^w}\left(\frac{1}{d_b}\right)^2\left(\frac{1}{\phi}\frac{\partial\phi}{\partial w}\frac{\partial\lambda_{i,j}}{\partial w} + \frac{\partial^2\lambda_{i,j}}{\partial w^2}\right) + r_{\lambda_{i,j}} - \frac{\lambda_{i,j}}{\phi}\frac{\partial\phi}{\partial t} \quad \text{for } i = 1,2;\ j = 1,2 \tag{G.6c}$$

$$\frac{\partial[C_1]}{\partial t} = -r_{M_1^w} - \frac{[C_1]}{\phi}\frac{\partial\phi}{\partial t} \tag{G.7c}$$

$$\frac{\partial[C_2]}{\partial t} = -r_{M_2^w} - \frac{[C_2]}{\phi}\frac{\partial\phi}{\partial t} \tag{G.8c}$$

$$\frac{\partial T}{\partial t} = \left(\frac{k_{\mathrm{cond}}}{\rho C_p}\right)\left(\frac{1}{d_b}\right)^2\frac{\partial^2 T}{\partial w^2} + r_T\frac{(-\Delta H_r)}{\rho C_p} \tag{G.9c}$$

Table G.4: Boundary conditions for the transformed extended model.

$\left.\frac{\partial[\mathrm{PR}^{\cdot w}]}{\partial w}\right\|_{w=0} = \left.\frac{\partial[\mathrm{PR}^{\cdot w}]}{\partial w}\right\|_{w=1} = 0$	(G.1d)
$\left.\frac{\partial[S_1^w]}{\partial w}\right\|_{w=0} = \left.\frac{\partial[S_1^w]}{\partial w}\right\|_{w=1} = 0$	(G.2d)
$\left.\frac{\partial[S_2^w]}{\partial w}\right\|_{w=0} = \left.\frac{\partial[S_2^w]}{\partial w}\right\|_{w=1} = 0$	(G.3d)
$\left.\frac{\partial[M_1^w]}{\partial w}\right\|_{w=0} = \left.\frac{\partial[M_1^w]}{\partial w}\right\|_{w=1} = 0$	(G.4d)
$\left.\frac{\partial[M_2^w]}{\partial w}\right\|_{w=0} = \left.\frac{\partial[M_2^w]}{\partial w}\right\|_{w=1} = 0$	(G.5d)
$\left.\frac{\partial[\mathrm{PDB}_e^w]}{\partial w}\right\|_{w=0} = \left.\frac{\partial[\mathrm{PDB}_e^w]}{\partial w}\right\|_{w=1} = 0$	甄G.6d)
$\left.\frac{\partial[\mathrm{H_2O}^w]}{\partial w}\right\|_{w=0} = \left.\frac{\partial[\mathrm{H_2O}^w]}{\partial w}\right\|_{w=1} = 0$	(G.7d)
$\left.\frac{\partial\lambda_{1,1}}{\partial w}\right\|_{w=0} = \left.\frac{\partial\lambda_{1,1}}{\partial w}\right\|_{w=1} = 0$	(G.8d)
$\left.\frac{\partial\lambda_{1,2}}{\partial w}\right\|_{w=0} = \left.\frac{\partial\lambda_{1,2}}{\partial w}\right\|_{w=1} = 0$	(G.9d)
$\left.\frac{\partial\lambda_{2,1}}{\partial w}\right\|_{w=0} = \left.\frac{\partial\lambda_{2,1}}{\partial w}\right\|_{w=1} = 0$	(G.10d)
$\left.\frac{\partial\lambda_{2,2}}{\partial w}\right\|_{w=0} = \left.\frac{\partial\lambda_{2,2}}{\partial w}\right\|_{w=1} = 0$	(G.11d)
$k_{\mathrm{cond}}\frac{\partial T}{\partial w}\left(\frac{1}{d_b}\right)\Big\|_{w=0} = -k_{\mathrm{cond}}\frac{\partial T}{\partial w}\left(\frac{1}{d_b}\right)\Big\|_{w=1} = h(T - T_s)$	(G.12d)

Appendix H
Experimental procedure

This appendix includes a more practical step-by-step approach of the experimental procedures, in addition to the information provided throughout this thesis. The following procedure (Table H.2) was used in the general preparation of the improved polymer gel dosimeter recipe for optical imaging of this thesis. Table H.1 lists materials used in the preparation of the polymer gels.

Table H.1: List of materials used in the preparation of the gels.

List of Materials
Erlenmeyer flasks
Graduated cylinders
Magnetic stir bars
PARAFILM®
Aluminum foil
Pasteur pipettes
Eppendorf pipette
Weighing dishes
Scoopulas and spatulas
Plastic powder funnel
Heating/Stirring Plate

Table H.2: Gel preparation.

1)	Always prepare the polymer gel in the fume hood and wear personal safety equipment (i.e. wear goggles, gloves, lab coat)
2)	Add the porcine gelatin to a clean Erlenmeyer flask and let it swell over 10-15 minutes with the total amount of water at room temperature without stirring.
3)	Heat and stir the swollen gelatin solution in a water bath held at 40 °C until the gelatin is fully dissolved (using a magnetic heater/stirrer plate).
4)	Cool the gelatin solution to 34 °C before adding NIPAM. Continue to stir until the NIPAM has fully dissolved.
5)	Once the NIPAM has fully dissolved, add Bis and stir until the Bis fully dissolves.
6)	Once the Bis has fully dissolved, cool the resulting solution to 30 °C before adding THPC (using an Eppendorf pipette) and stirring for another couple of minutes.
7)	Transfer the final solution from the Erlenmeyer flask to a set of plastic cuvettes using a Pasteur pipette, and cap the cuvettes.
8)	Tightly seal the cuvettes with *PARAFILM*® around the lid to prevent oxygen diffusion and then wrap the cuvettes in aluminum foil to prevent photo-initiated polymerization.
9)	Place all the filled cuvettes in a plastic zip-lock bag, purge with nitrogen gas and store in a covered environment to allow the gel to set (a refrigerator may be required).

Appendix I

Nomenclature for appendices

Symbols	
C^i	Cyclized unit in the *i*th phase
C_p	Heat capacity of the PAG gel system [J kg^{-1} K^{-1}]
d_b	Depth of the back wall
d_{max}	Depth of maximum delivered dose on depth-dose curves
D^i	Dead polymer chain in the *i*th phase. In the aqueous phase, subscript *n* indicates the length of the chain
D^i_i	Diffusivity in the *i*th phase of the j^{th} species [cm^2 min^{-1}]
e_{aq}^-	Hydrated electron
f	Radical efficiency
G	Gelatin
h	Heat transfer coefficient for heat transfer from the PAG to the surrounding environment [J cm^{-2} K^{-1} s^{-1}]
H_2O	Water
ΔH_R	Energy released per mole of double bonds consumed
k_{cond}	Thermal conductivity in the PAG dosimeter [J cm^{-1} K^{-1} s^{-1}]
k_c	Rate constant for intermolecular cyclization reactions [$M^{-1}s^{-1}$]
$k_{f,jk}$	Rate constant for chain transfer reaction of a polymer radical bearing the active radical on an acrylamide unit (j = 1), bisacrylamide unit (j = 2), or peroxy unit (j = 3) to acrylamide monomer (k = 1) or bisacrylamide monomer (k = 2) [$M^{-1}s^{-1}$]
$k_{f,jG}$	Rate constant for chain transfer reaction of a polymer radical bearing the active radical on an acrylamide unit (j = 1), bisacrylamide unit (j = 2), or peroxy unit (j = 3) to gelatin [$M^{-1}s^{-1}$]

$k_{ini,k}$	Rate constant for initiation reaction between primary radicals and acrylamide monomer (k = 1) or bisacrylamide monomer (k = 2) [$M^{-1}s^{-1}$]
k_m	Mass transfer coefficient [s^{-1}]
$k_{p,jk}$	Rate constant for propagation of a polymer radical bearing the active radical on an acrylamide unit (j = 1) or bisacrylamide unit (j = 2) with acrylamide monomer (k = 1) or bisacrylamide monomer (k = 2) [$M^{-1}s^{-1}$]
$k_{p,Gk}$	Rate constant for re-initiation of a gelatin radical with acrylamide monomer (k = 1) or bisacrylamide monomer (k = 2) [$M^{-1}s^{-1}$]
$k_{t,jk}$	Rate constant for termination reaction between a polymer radical bearing the active radical on an acrylamide unit (j = 1), bisacrylamide unit (j = 2), or peroxy unit (j = 3) and a polymer radical bearing the active radical on an acrylamide unit (k = 1), bisacrylamide unit (k = 2), or peroxy unit (k = 3) [$M^{-1}s^{-1}$]
$k_{x,j}$	Rate constant for crosslinking reaction between an unreacted pendant double bond and a polymer radical bearing the active radical on an acrylamide unit (j = 1) or bisacrylamide unit (j = 2) [$M^{-1}s^{-1}$]
k^0_{fij}, k^0_{pij} k^0_{tij}	Rate constants for trasnfter to monomer, propagation and termination in the absence of diffusion control
L_i	Growing radical in polymer phase, bearing the active radicals on an acrylamide unit (*i* = 1), bisacrylamide unit (*i* = 2), or peroxy (*i* = 3) unit.
M_1	Acrylamide monomer
M_2	Bisacrylamide monomer
$M_{w,H2O}$	Molecular weight of water [g mol^{-1}]
n_{PDE}	Number of pendent double bonds on a water soluble polymer chain
$(PR^{\bullet})$	Primary radical in water cage
$PR^{\bullet}$	Primary radical outside of water cage
r_i	Rate of reaction of species *i* [mol L^{-1} s^{-1}]
R	Gas constant (1.9872 cal mol^{-1} K^{-1})
R_2	Transverse relaxation rate [s^{-1}]
$R_{(PR)}$	Rate of generation of primary radicals [mol s^{-1}]

$S_{j,n}$	(short) Propagating radical of length n, bearing the active radicals on an acrylamide unit (i = 1), bisacrylamide unit (i = 2), or peroxy (i = 3) unit.
$\bar{S}_{w,i}$	Weight average chain length of water soluble radicals with terminal monomer i
T	Temperature inside the PAG system [°C]
T_S	Temperature of the surrounding environment [°C]
V_{avg}	Average volume of a monomer unit attached to a soluble polymer chain
X	Crosslinked unit
x	Horizontal coordinate [cm]
w	Transformed horizontal coordinate

Subscripts	
n	Number that indicated chain length
1	Acrylamide
2	Bisacrylamide
3	Newly crosslinked unit without a neighbouring PDB (only L_3^p)

Superscripts	
•	Radical species
w	Aqueous phase
p	Polymer phase

Greek	
Γ	Fraction of total delivered dose
γ	Gamma radiation
$\lambda_{i,j}$	Moments of the water soluble growing radical distribution (i=0,1,2) with the active radical on an acrylamide (j=1) or bisacrylamide (j=2) unit
ϕ	Volume fraction of the reaction volume occupied by the aqueous phase
θ	Fraction of gelatin radicals that can re-initiate polymerization
Φ_i	Ratio of the concentration of species i in the polymer-phase over the concentration of the same species in the aqueous phase
Acronyms	
AAm	Acrylamide monomer
Bis	N,N'-methylene-bisacrylamide crosslinker
CT	Computed Tomography
Gy	Gray, unit for radiation dose (= J/kg)
MeV	Mega-electronvolt
MRI	Magnetic Resonance Imaging
MV	Megavolt
NIPAM	N-isopropylacrylamide monomer
PAG	Polyacrylamide gel
PDB	Pendant double bond
PDB_e	Pendant double bond available for crosslinking
PDE	Partial differential equation
THPC	Tetrakis (hydroxymethyl) phosphonium chloride